UNIVERSITÀ DEGLI STUDI DI MILANO

SCUOLA DI DOTTORATO
FISICA, ASTROFISICA E FISICA APPLICATA

DIPARTIMENTO
DI FISICA

CORSO DI DOTTORATO DI RICERCA IN
FISICA, ASTROFISICA E FISICA APPLICATA
CICLO XXIII

Study of Positronium Converters in the AEGIS Antimatter Experiment

Settore Scientifico disciplinare FIS/04

Tesi di Dottorato di:
Davide Trezzi

Supervisore: Dott. Marco Giulio Giammarchi
Coordinatore: Prof. Marco Bersanelli

A.A. 2009-2010

Contents

Chapter 1

AE$\bar{g}$IS antimatter experiment, an overview

1.1 The theoretical framework

The theory that describes the gravitational interaction is General Relativity, formulated by A. Einstein in 1915. This theory is based on the *equivalence principle* that, in its original formulation, assumes the physical equivalence between gravitational field and an uniform accelerating reference frame. Today we have three formulations for the equivalence principle, namely: the weak equivalence principle, Einstein's equivalence principle and the strong equivalence principle. The last two require the veridicity of the first one, that is: "all bodies in the same time-space point, in a given gravitational field, are subject to the same acceleration". In the particle physics framework this means that matter and antimatter in the same gravitational field, like the Earth's one, should be subject to the same acceleration or the gravitational interaction is unchanged under charge conjugation symmetry. Modern theories [1] (e.g theories of supergravity), formulated in order to unify in one theory the gravitational interaction with the electroweak and strong interactions, allow for the possibility that matter and antimatter can interact in a different way in some gravitational field, and in particular in the terrestial one. In other words, this would result in the violation of the weak equivalence principle. An experimental evidence is thus fundamental in order to test such candidate theory of everything.

In the formalism of modern quantum mechanics, every local Lorentz-invariant quantum field theory, like the Particle Standard Model, should be invariant under CPT transformation that is the composition of three discrete symmetries: charge conjugation C, parity P and time reversal T. This property was independently found by G. Lüders, W. Pauli and J. Schwinger and is nowadays known as the *CPT theorem* [2]. From CPT theorem one can derive some interesting conclusions:

1. particles can follow Bose-Einstein or Fermi-Dirac statistics. If they have integer spin they follow the Bose-Einstein statistics otherwise in the case of semi-integer spin, they follow the Fermi-Dirac statistics. In quantum mechanics this imply that the integer spin operators should be quantized using the commutation rules whereas the semi-integer ones should be quantized using the anti-commutation rules;

2. particles and anti-particles must have identical rest masses and life-times;

3. all internal quantum numbers of the anti-particles must be opposite than those of the corresponding particle;

4. the transition frequencies for the matter and anti-matter bound states must be the same.

While experimental P,C,CP and T symmetries (in the Particle Standard Model) are violated [3], CPT violations have never been found. The importance of this symmetry requires accurate experimental tests with every kind of particles: barions, mesons and leptons. AE$\bar{g}$IS - namely *Antimatter Experiment: Gravity, Interferometry, Spectroscopy*[4] - is an experiment designed to test the weak equivalence principle by measuring the $\bar{g}$ constant with an accuracy of about 1% for anti-hydrogen atoms. Moreover, gravity measurements should be indipendent from the theoretical framework used to describe the interaction with the Earth's gravitational field. In a second phase of the experiment, a comparison between the hydrogen and anti-hydrogen electromagnetic spectrum will give a high sensitivity test for the CPT theorem.

1.2 Antihydrogen Physics

Antihydrogen is the simplest antimatter atoms. It is composed of an antiproton and positron (anti-electron). The first evidence of antihydrogen was obtained at CERN in 1995. The experiment, named PS210 [5], took place in the LEAR antiproton ring facility [6] where antiprotons, produced in the PS ring [7], hit Xenon atoms in order to produce electron-positron pairs. Thus antiprotons and positrons could form antihydrogen atoms but with high mean kinetic energy (billions of Kelvin ($\sim GeV$, indicated like "hot antihydrogen"). Hot antihydrogen production was confirmed later, in 1997, at Fermilab accelerator [8]. Antihydrogen of such high energy could not be used for tests of fundamental symmetries. In 2000, the AD *Antiproton Decelerator* ring [9] substitute the older LEAR, in order to decelerate antiproton to $5MeV$. The new energy of the antiproton beam can be further decelerate to a few eV after moderation. Two AD experiments, ATRAP [10] and ATHENA [11], brought together antiprotons and positrons (produced

by a Sodium 22 radioactive source) in Penning traps. Such antihydrogen atoms, produced for the first time by ATHENA [12] and subsequently by ATRAP [13] in 2002, had a mean kinetic energy of a hundred Kelvin. These atoms are still too hot to be used for experiments like atomic spectroscopy. However ATHENA and ATRAP gave the first evidence that cold antihydrogen could be made. A new experiment, ALPHA[14], as well as ATRAP, is pursuing the production of antihydrogen at much lower kinetic energy so that it could be confined magnetically. In 2008 the AE$\bar{g}$IS experiment [15] proposed another process - namely the charge exchange reaction between antiproton and positronium - in order to produce "cold antihydrogen" with a mean kinetic energy of the order of $100mK$. Such low energy beam will be used for gravity fall measurements (see the next sections). Other experiments at CERN are using antihydrogen for antimatter physics, like ASACUSA [16] (Atomic spectroscopy and collisions using slow antiprotons) and ACE [17] (Relative biological effectiveness and peripheral damage of antiproton annihilation).

1.3 The AE$\bar{g}$IS experiment

The AE$\bar{g}$IS experiment, under construction at the CERN Antiproton Decelerator[1], aims at directly measuring the gravitational acceleration $\bar{g}$ by detecting the vertical deflection of an anti-hydrogen beam, after a flight path of about 1 meter, with a 1% relative precision. In AE$\bar{g}$IS , the essential steps leading to the production of anti-hydrogen ($\bar{H}$) and the measurement of gravitational interaction it undergoes are:

1. the production of cold ($100mK$) anti-hydrogen beam based on the charge exchange reaction between cold ($100mK$) anti-protons and Rydberg positronium,

2. the formation and acceleration of a Rydberg anti-hydrogen beam using inhomogeneous electric fields and

3. the determination of $\bar{g}$ through the measurement of the vertical deflection of the antihydrogen beam in a two-grating Moiré deflectometer coupled with a position-sensitive detector.

1.3.1 Production of cold anti-hydrogen

Cold anti-hydrogen ($\bar{H}$) in AE$\bar{g}$IS will be produced by the charge exchange reaction between cold anti-protons ($\bar{p}$) and Rydberg positronium (Ps^*):

$$\bar{p} + Ps^* \rightarrow \bar{H}^* + e^-$$

[1]The experiment has been approved at CERN in 2008 and the installation in the experimental hall has begun in 2010.

Antiprotons delivered by the CERN Antiproton Decelerator, will be trapped in a Malmberg-Penning trap (catching trap) mounted in a horizontal cryostat inside the bore of a 3 Tesla magnetic field and cooled by electron cooling down to subeV energies in a cryogenic environment at $4K$ in temperature. The antiproton cloud will be radially compressed and then transferred into a second trap mounted in a colder region (100 mK) and with a magnetic field of 1 Tesla (antihydrogen formation trap). Here antiprotons will be cooled down to 100 mK.

Instead, the Positronium will be formed by bombarding a porous material - converter - with bunches of 10^8 positrons, with a time length of 10-20 ns. A fraction of the positrons are re-emitted as positronium atoms with a velocity of about $10^4 m/s$. In this thesis we will investigate the proprierties of the AE$\bar{g}$IS candidate converters. Positronium atoms are subsequentially excited, by two laser pulses, to Rydberg states with principal quantum number $n = 20 - 30$, thus optimizing the cross section of the charge exchange reaction which depends on the fourth power of n [15].

The production of cold ($100mK$) anti-hydrogen takes place when the Rydberg positronium traverses the cold anti-proton cloud. Taking into account the velocity of the Rydberg positronium and the anti-proton cloud dimensions (of the order of few mm) the production time of anti-hydrogen is defined within about $1\mu s$. This pulsed anti-hydrogen production allows for the possibility of measuring both the anti-hydrogen temperature and the $\bar{g}$ constant, by a time of flight method. Figure 1.1 shows the region where anti-hydrogen will be formed, accelerated and sent to the grating system.

1.3.2 Formation and acceleration of anti-hydrogen beam

The formation and acceleration of anti-hydrogen beam in AE$\bar{g}$IS will be obtained by switching the voltage applied to the anti-proton trap electrodes from the usual Penning trap configuration to a new configuration that we call "Rydberg accelerator" [18]. This new configuration consists in applying appropriate voltages to generate an electric field, having an amplitude decreasing along the z axis, designed to accelerate, by Stark effect, the anti-hydrogen atoms. The accelerating electric field will stay on for a selected time interval (about $70 - 80\mu s$), then the field will be switched off as the anti-hydrogen atoms continue to fly toward the grating system, decaying to the fundamental state. The time when the field is switched off will provide a $t = 0s$ time for the gravity measurement. The Rydberg anti-hydrogen atoms will be produced with a distribution of quantum states, with principal quantum number $n = 25 - 35$; the simulation of the expected horizontal velocity shows a broad distribution peaked around about $500 - 600 m/s$ [15].

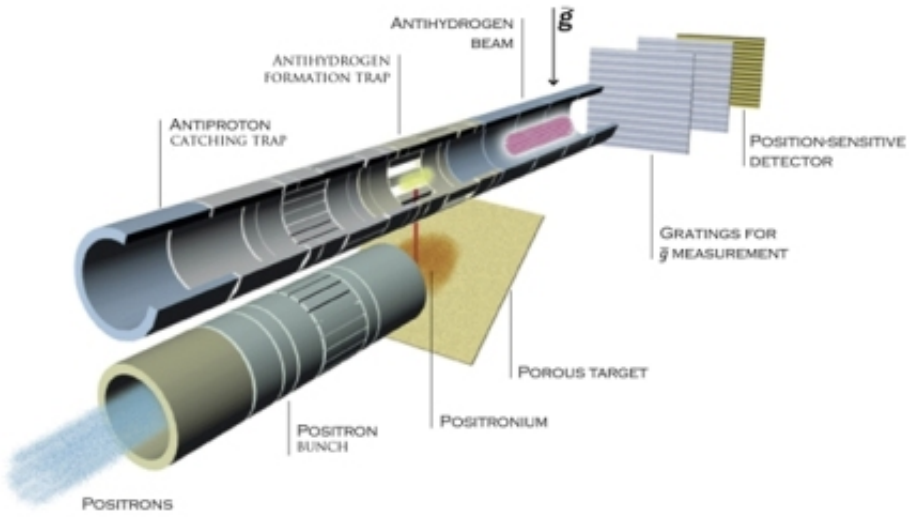

Figure 1.1: Sketch (not to scale) of the AE$\bar{g}$IS setup where anti-protons and positrons are manipulated to form anti-hydrogen beam. Antihydrogen beam is accelerated towards the grating system in order to measure the gravity acceleration constant $\bar{g}$.

1.3.3 Measurement of the gravitational acceleration

The measurement of the gravitational acceleration $\bar{g}$ will be achieved by detecting the vertical deflection, due to the Earth's gravitational field, of the anti-hydrogen beam. This vertical displacement, given AE$\bar{g}$IS realistic numbers (1 m flight path, anti-hydrogen horizontal velocity about $500m/s$) would be very small (about $20\mu m$) and will be measured using a classical Moiré deflectometer. It consists of two material gratings, selecting specific trajectories of the atoms, coupled with a position-sensitive detector. The distribution of the number of atoms arriving on the detector as a function of the vertical coordinate shows a periodical pattern due to the gratings. The gravity force causes a vertical shift of this pattern which depends on the time of flight between the two gratings. From the measurement of the vertical position and of the horizontal velocity of the particles, it is possible to reconstruct the value of the gravitational acceleration $\bar{g}$. The image of the anti-hydrogen beam will be obtained by reconstructing the annihilation point of each atoms on the position-sensitive detector. To ensure an accurancy of 1% for the $\bar{g}$ measurement, this detector must have specific requirements: spatial resolution of about $10\mu m$, active area of $20 \times 20cm^2$ and capability to operate at cryogenic temperatures. Simulations have shown that these requirements can be satisfied by a silicon microstrip detector $300\mu m$ thick, with 8000 strips and a $25\mu m$ pitch [15].

Chapter 2

The AE$\bar{g}$IS positron source

As previously seen, in order to produce Positronium, AE$\bar{g}$IS requires an intense monoenergetic positron beam. Thus positrons, emitted from an intense radioactive ^{22}Na source, will be moderated and magnetically guided to the positron trap and accumulator. Through these last two stages, the beta plus positron - monoenergetic after the moderation process - are cooled, accumulated and bunched. The operation of the positron trap is based on the buffer gas slowing down and cooling of positrons in a Penning-Malmberg trap. A device of this type has been used with success in the ATHENA antimatter experiment [11] and the technology is now so well established that a commercial version of the system is available [1]. In this chapter we report on the first studies about the AE$\bar{g}$IS positron source and moderator system that were made during the PhD activity. We will not talk in detail about the accumulator system (the reader can find more informations in [15]). A scheme of the AE$\bar{g}$IS apparatus is shown in figure 2.1.

2.1 The positron source

Of all the radionuclides used in experiments as positron sources, the most convenient is the ^{22}Na isotope [20]. Its half-life period is $2.6yr$, which is sufficient for carrying out long-term experiments. The high intensity source (75 mCi) will be supplied by the iThemba Labs and will be located at CERN. This is the most active ^{22}Na radioactive source useful for positron experiments. For greater activity value the positron emission is reduced by self-absorption. The source was provided with its holder used for insert it safely into the source plus moderator system as shown in figure 2.2.

In the holder, the ^{22}Na is sealed behind a $13\mu m$ tantalum window.

[1] At the moment, AE$\bar{g}$IS has committed a custom-modified positron accumulator to the First Point Scientific Inc., whose delivery is scheduled for 2011 [19]. Also the source and moderator (the commercial name is RGM-2) was ordered in 2010 to the First Point Scientific Inc.

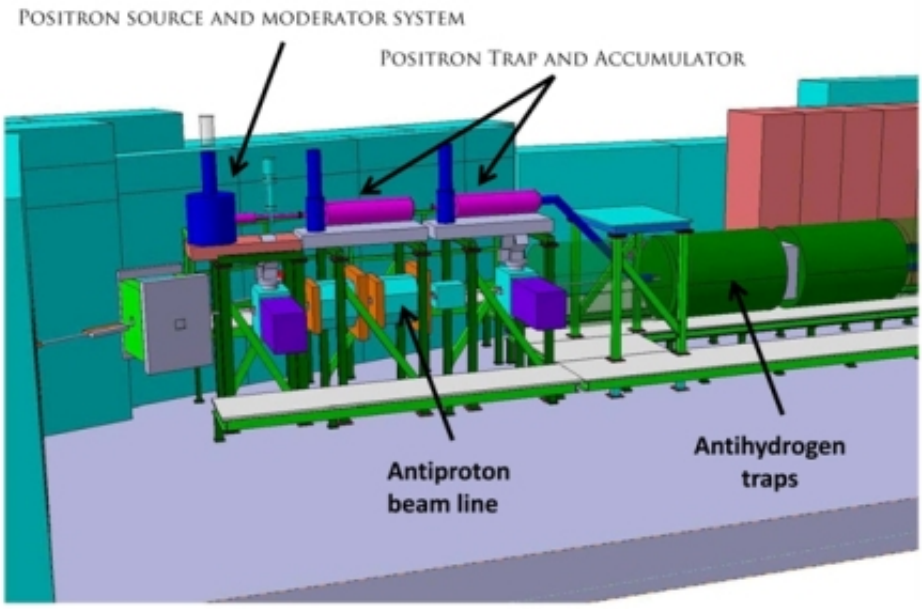

Figure 2.1: A raw scheme of the positron source and accumulator in the AE$\bar{g}$IS experiment.

Figure 2.2: The source holder. The cylinder in the background is part of the moderator system.

Positrons emitted by such a radioactive source have a wide energy spectrum with a maximum at about $514keV$ (figure 2.3).

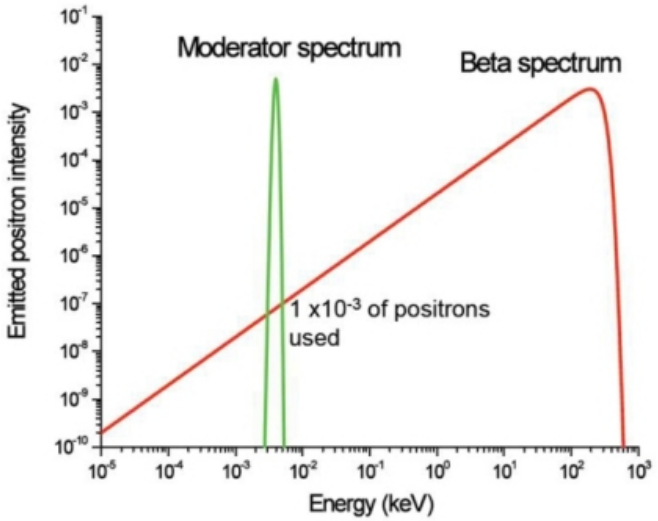

Figure 2.3: The positron energy spectrum shape after and before the moderation process.

Because of this high energy, positron accumulation is impossible. It is therefore necessary to convert the positron energy distribution from a beta plus spectrum to a monoenergetic one (Gaussian with a much lower average energy). This process, named "moderation", will be discussed in the next section.

2.2 The moderator system

Positrons slow down in a solid body initially through ionization losses and, below the ionization threshold, through the generation of an electron - hole pair and excitation of excitons and phonons. When thermalized, a positron can either diffuse to the surface and escape from the substance or be trapped in the substance and annihilate with an electron directly or via formation of Positronium. A solid is characterized by work function for positron ϕ_+, which is equal to the difference of the particle's potential energy inside the solid and outside it. For $\phi_+ > 0$, a potential barrier is formed at the surface-vacuum border, which forbids the escape of thermal positrons. Solid Neon, a dielectric with a wide energy gap, is the most effective moderator for positrons [20] (see table 2.1).

Neon has $\phi_+ > 0$, which prevents the escape of thermal positrons. Since the energy gap is wide, a large part of positrons had no time to be completely thermalized in a thin Neon layer. As a result, they have enough energy to

Material	Efficiency
MgO (polycrystalline powder)	$3 \cdot 10^{-5}$
Cu(111) (a single crystal)	$1 \cdot 10^{-3}$
B (a polycrystal coated with carbon)	$\cong 10^{-7}$
W(110) (a single crystal)	$3 \cdot 10^{-3}$
Ne (solid Ne at 5 K)	$7 \cdot 10^{-3}$

Table 2.1: The positron energy spectrum shape after and before the moderator process.

overcome the potential barrier at the surface. To maximize the yield of slow positrons, the thickness of a solid Neon layer must be selected close to the ionization length of a positron emitted by the ^{22}Na isotope with maximum energy. The spread of the final positron energy depend on the layer the Neon layer's thickness d. The minimum spread value, of about $0.5eV$, is obtained for $d = 130\mu m$ and the final energy spectrum of the emitted positrons is a gaussian-like with a mean value that varies between $0.5eV$ to $2.0eV$, as reported in [20]. The main disadvantages of the Neon moderator (and in general of the Rare Solid Gas Moderators - RGS) is that the energy spread of the moderated positrons is substantially larger than that of positrons from metal film moderators (e.g. Tungsten foil).

The best efficiency is achieved with a conical moderator as reported in [21]. The moderator support is in copper and cooled to a temperature of about $5-7K$. At this temperature the moderator gas, like Neon, can solidify on the support. The connection between the source and the closed-cycle refrigerator[2] is provides by an Elkonite rod. This is electrically isolated from ground by a sapphire washer, to allow electrical biasing of the source.The vacuum chamber is filled with gaseous Neon which will condensate onto the moderator support surface, forming a solid moderator layer. In order to increase the positron yield and collimate the beam, a metallic grid and collimator can be mounted in front of the source plus moderator system. A good approximation estimates a positron yield of about $10^6 - 10^7 e^+/sec.$ In figure 2.4 we shown a schematic diagram of the source and cold - head assembly.

2.3 The positron magnetic guide

In order to guide the positrons emitted by the source plus moderator system, an axial static magnetic field is applied. The field intensity, produced by a set of coils or solenoids, varies from $100G$ to $300G$ and can be computed by the MI-AEGIS.Mag software as shown in figure 2.5. The field strength

[2]For example the ARS DE-210SB closed cycle cryostat.

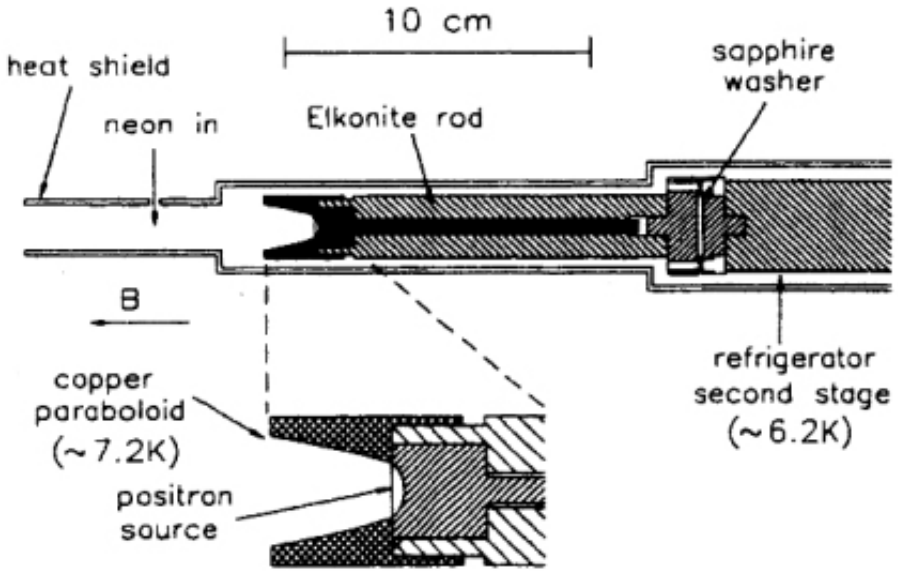

Figure 2.4: Schematic diagram of the source and cold-head assembly.

was chosen in order to match the positron trap and accumulator's input magnetic field.

This field's gradient thus reduce the dimension of the spot by a factor $\sqrt{3}$ [22]. The positron source produce a forward gamma radiation that can be shielded by inserting an $\vec{E} \times \vec{B}$ system in the $300G$ region. It is possible to substitute the $\vec{E} \times \vec{B}$ system with a set of curved solenoids or by a magnetic slalom system as reported in [20]. However, the $\vec{E} \times \vec{B}$ system reduces also the energy spread of the positrons. We compute the positron spot radius at the starting point of the $300G$ region by developing a SIMION 7.0 simulation. The dimensions of the apparatus and the simulations are shown in figure 2.6.

At the end of the positron magnetic guide we expect a radius of about $0.66cm$ comparable with that obtained in a typical positron source apparatus (i.e. the Surko machine [23]). From the simulations we obtain that the spot dimension does not depend on the positron source potential and neither by the positron energy at the moderator surface (in the range between $0.2eV - 2.0eV$, in the isotropic emission approximation). The possibility to build up a positron source system for AE$\bar{g}$IS , supported by references and simulations, was presented at CERN during the AE$\bar{g}$IS meeting, 30th-31st March 2009. Respect to a commercial positron source plus moderator system, the one presented here is more customizable. The main disadvantage is instead the long time need for the R & D of the apparatus.

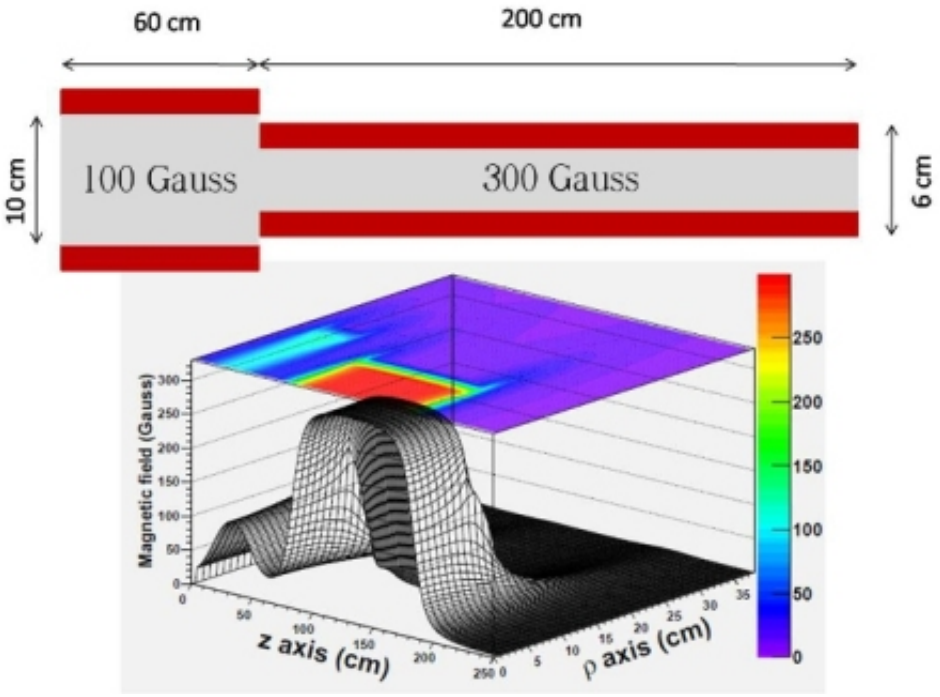

Figure 2.5: The AE$\bar{g}$IS source's magnetic field computed by MI-AEGIS.Mag software (100G and 300G regions). The z axis is the axis of the AE$\bar{g}$IS apparatus. ρ is the radial coordinate in cylindrical coordinates.

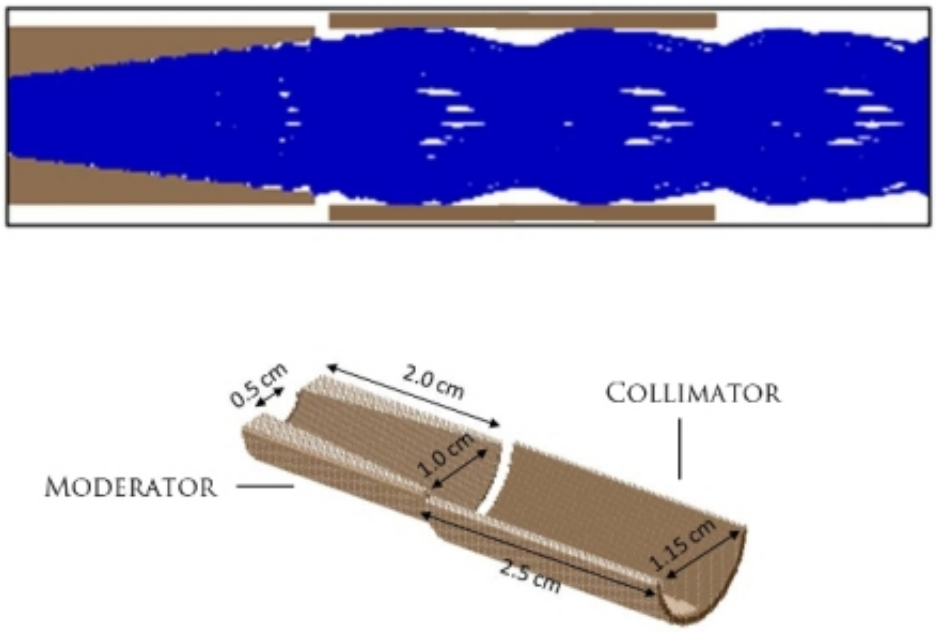

Figure 2.6: SIMION 7 simulation for the AE$\bar{g}$IS positron source, in blue the positron tracks for positrons isotropically emitted up to $6eV$ from the cone surface (at $40V$). The dimensions of the cone and the cylindrical collimator in front of it (at ground) are shown below.

2.4 The RGM system

The RGM-1, *Rare Gas Moderator* - 1, is the commercial name of the positron source and moderator system developed by the First Point Scientific Inc. This represents a positron beam with an output of up to $10^7 e^+/sec$. It includes the equipment for producing the solid Neon moderator, the radiation shielding for ^{22}Na sources up to $150mCu$, magnetic beam transport and source manipulating for loading and unloading source capsules with minimum radiation exposure. The usual RGM-1 system scheme is shown in figure 2.7.

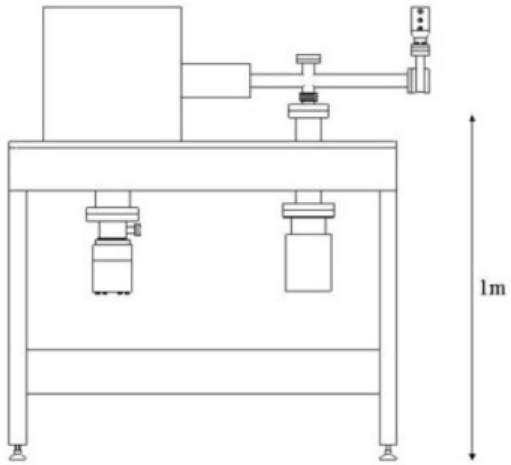

Figure 2.7: The RGM-1 apparatus.

As shown in figure 2.1, this configuration does not fit with the AEḡIS apparatus. In order to solve the problem the First Point Scientific developed a new RGM-1 design named RGM-2. Thus the RGM-2 practically is the RGM-1 system upside down. The design of this new apparatus is shown in figure 2.8.

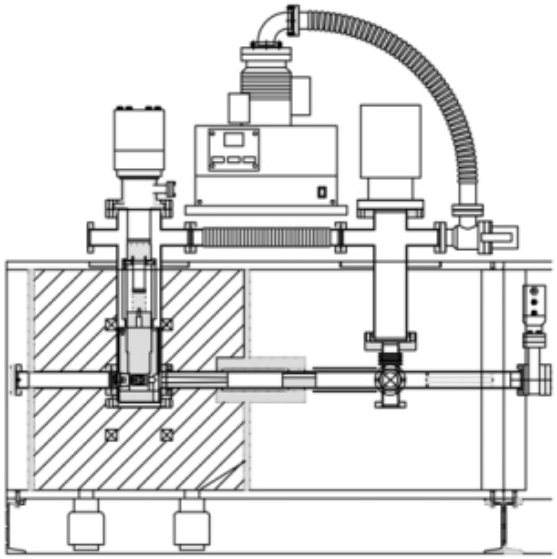

Figure 2.8: The RGM-2 apparatus.

Chapter 3

Positronium Physics

3.1 Introduction

The charge exchange reaction between cold antiprotons and Rydberg positronium is used in the AE$\bar{g}$IS experiment in order to produce cold antihydrogen, as described in section 1.3.1. Positronium is the simplest quantum electrodinamical bound system in nature, composed by one electron and one positron [24]. The ground state of positronium, like that of hydrogen, has two possible configurations depending of the relative orientations of the spins of the electron and the positron. The singlet state with antiparallel spins is known as *para-positronium* (pPs) whereas the triplet state with parallel spins is known as *ortho-positronium* (oPs). In order to conserve C-parity para-positronium and ortho-positronium states should annihilate in different ways with different lifetimes, as expected by quantum electrondynamics. Para-positronium decay via $pPs \rightarrow \gamma + \gamma$ and ortho-positronium $oPs \rightarrow \gamma + \gamma + \gamma$. The lifetime of para-positronium in vacuum was first calculated to lowest order of perturbation theory by Wheeler [25]. The more complicated calculation of ortho-positronium lifetime in vacuum was done to lowest order of perturbation theory by Ore and Powell [26]. The difference between the two lifetimes is due to an additional power of the fine structure constant α which follows directly from the Feynman rules given by the additional photon in the ortho-positronium annihilation process. Vacuum lifetimes have been calculated to order α^7 for para-positronium and order α^8 for otho-positronium [27] with results $\tau_{pPs} = 125ps$ and $\tau_{oPs} = 142ns$. As in the hydrogen atom-case, para-positronium and ortho-positronium atoms can be formed in excited states Ps^* other than the ground state. Excited positronium with high n levels is called Rydberg positronium.

Positronium can not be found in nature. As it is highly unstable the simplest way to produce positronium in laboratory is to implant positrons with low enough kinetic energy into a solid target which is then called converter[1].

[1]It is possible to produce positronium also in liquid and gases as reported in section

Positron slowing down to thermal energies occurs rapidly in comparison with annihilation [28]. Thermal and epithermal positrons can be re-emitted into the vacuum as positronium atoms after capture of an electron. Almost all positronium produced are in the ground state[2]. The positronium formation yield and its energy distribution depend on the nature of the converter material and, for a specific material, on the implantation depth and on the temperature of the target. In the AE$\bar{g}$IS experiment, the ground state positronium must be excited to $n = 20 - 30$ level by a two step laser pulse [30]. Given that the para-positronium lifetime is too short to allow its laser excitation before it decays ($125ps$), in the AE$\bar{g}$IS experiment is interested only in the fraction of positronium emitted as ortho-positronium ($142ns$).

3.2 Positronium formation in solids

In this section we will discuss the formation and properties of positronium in solids. Positronium production occurs in metals and semiconductors as well as in insulator materials but the production mechanisms are somewhat different.

3.2.1 Positronium formation in metal and semiconductors

In metal and semiconductors, positronium formation is only a surface process originating from positron back-diffusion or transmission across the surface followed by electron capture. Thermalized positrons can produce positronium by an adiabatic charge transfer reaction at any converter temperature, provided that the positronium formation potential W is negative:

$$W = \Phi_- + \Phi_+ - 6.8eV < 0 \tag{3.1}$$

where $6.8eV$ is the positronium ground state binding energy and Φ_- and Φ_+ are, respectively, the work functions of the electron and of the positron for the converter material. In this case, positronium leaves the surface with an energy distribution extending from zero up to the work function energy, resulting in a mean energy of the order of a few eV. If $W > 0$ the positronium adiabatic emission is scarce and mostly due to ephitermal positrons. When also $\Phi_+ < 0$ the process of direct positron emission is in competition with the adiabatic positronium emission. In addition to the adiabatic emission, thermally activated formation has been observed [31]. This additional process is dominant when the target temperature is of the order of several hundred kelvin and it is interpreted in terms of surface traps in which the positrons reside but from which it may be desorbed as positronium. In this case positronium has an energy distribution corrisponding to the target temperature.

3.3.2.

[2]For $n = 2$ "natural" positronium production see [29].

3.2.2 Positronium formation in insulators

In insulators, surface formation of positronium by thermal positrons is unlikely since the binding energy of positronium atom is normally insufficient to compensate for the exctraction of the positron and of the electron ($W > 0$). However the themalization of positrons in an insulator is less efficient than in a metal, thus a large flux of positrons returning to the surface of the insulator with a sufficient kinetic energy to form positronium can be expected. The energy spectrum in this case reflects the energy distribution of the ephitermal positrons and may extended up to several eV.

In addition positronium can be formed in the bulk as quasi-positronium[3], reach the surface and then be emitted in vacuum. In this case positronium is formed during the slowing down of positron, mostly when the positron energy is in the range between $E_{gap} - E_{solid}$ and E_{gap} (the so called "Ore gap" [33]). E_{gap} is the energy necessary to excite an electron from the valence to the conduction band and E_{solid} is the binding energy of the positronium atom in the solid. In general $E_{solid} < 6.8eV$. Bulk positronium formation is also possible when a positron encounters a spur electron, i.e. an electron raised in the conduction band by the positron itself during its slowing down [34]. The positronium atom in solid is a mobile system, as long as it is not trapped by a defect or self-trapped in a phonon-cloud; it will eventually reach the surface with a residual kinetic energy E_{CM} (of the order of few eV) that depends on the depth of formation. The two options described above (surface or bulk formation) depend on the temperature of the converter only indirectly, through temperature effects on migration and trapping.

3.2.3 Monte Carlo simulation of Ps formation in solids

Monte Carlo simulation of Ps formation Al_2O_3

Lacking experimental data, the Monte Carlo simulation of positronium formation in solids is the only method that gives informations about the energy spectrum and the angular distribution of the emitted positronium. In order to achieve this goal, my Master thesis [35] consisted in develop a simulation of positronium formation in insulator materials and in particular in Alumina (Al_2O_3). The idea is that, when we know precisely the energy and velocity distribution of the emitted positronium atoms, we will implement the positronium thermalization in nanochannels and/or pores in order to predict the characteristics of the final positronium cloud that will be excited by

[3]The electron - positron pairs interacting with a solid medium (the so called quasi-positronium) have close analogies with the positronium atom discussed in the introduction, in particular for the spin-dependent part of the wave function, but also it's possible to expect important difference in the spatial part of the wave function and in the absolute values of the annihilation rates as reported in [32]. However since the second half of '90 the positronist community decided to use the word positronium also for indicate quasi-positronium atoms. In this PhD thesis we will use this new terminology.

laser. The simulation starts with an ingoing positron with a kinetic energy between zero and $5keV$. Such positron enters in the Alumina solid and it is followed, scattering by scattering, till its energy is grater than the cut-off energy, fixed in our simulation at $1eV$. Two different approach are used for compute the positron tracks in the range $5keV - 20eV$ and $20eV - 1eV$. If the positron goes back at the solid surface it have a probability P_{Ps} to form positronium. This is the first step of an overall simulation of the AE$\bar{g}$IS target in which the outgoing positronium hits the inner nanochannel surface and lost energy by inelastic scatterings (figure 3.1). Low energy positronium (meV) is fundamental in order to maximize the antihydrogen production cross section for the process $Ps^* + \bar{p} \rightarrow \bar{H} + e^-$.

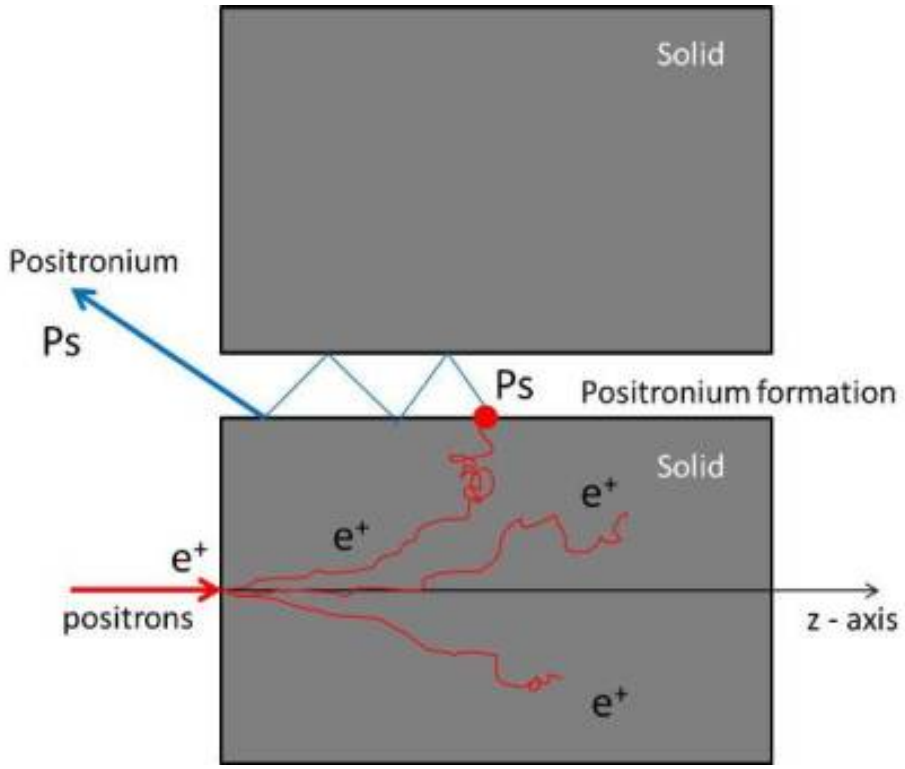

Figure 3.1: The Monte Carlo scheme: in red the positrons slowing down and positronium formation. In blue the positronium thermalization in ordered nanochannels (not considered, at the moment, in our simulations).

The scheme used for the simulation, in the energy range between $5keV$ and $20eV$, is based on the energy loss approximation model [36]. During the slowing down process in matter, the positron undergoes many elastic scattering with the atoms of the media that produce angular deviations of the positron path given by the elastic differential cross section. This quantity can be computed by solving the Dirac equation for a given electrostatic

potential in the non-relativistic limit. During the positron slowing down, in addition to elastic scattering we also have inelastic processes, i.e. atomic excitation, ionization or radiative effects. These processes can be included using a "mean" approach studying the positron Energy Stopping Power. This quantity allows us to get the mean energy loss for unity of length. Averaging over all inelastic processes involved, it reduces the sensibility of the Monte Carlo to statistical effects that were not considered in our simulation [37]. While the Energy Stopping Power for positrons with energy greater than $10keV$ is theoretically known [38], at energy below $10keV$ only a few models have been developed. In our simulation, one of these, the H. Gümüş model [39] was used. However it fails at energy lower than a few tens of eV. At such low energies the inelastic positron interaction depend both on the class of solids and the solids structure (amorphous or crystalline) or the presence of cavities (without cavities, regular or irregular porous or channeled media). In our simulation we considered only amourphous media without cavities. This is the case of the Aluminum Oxide Al_2O_3 (Alumina). This is the costituent of Whatman® membrane, that is one of the possible candidates for the AE$\bar{g}$IS converter. Whatman® membrane will be discussed in section 3.4.2.

The scheme used in order to simulate the positron tracks in the $20eV - 1eV$ energy range is based on the Ritley scheme [40], originally developed for solid metals. Each positron with energy less than $20eV$ is followed till the cut-off energy value fixed in our simulation at $1eV$. The positron moves on straight lines which length is an appropriate part of the total mean free path. At the end of every straight line the positron, with a given probability defined by the elastic and inelastic cross sections ratio, makes an elastic or inelastic scattering with a molecule of the medium. In each case the scattered positron moves in a new direction and, in the case of inelastic scattering, it loses a quantity ΔE of its kinetic energy.

If the positron backscatters till the surface with kinetic energy in the Ore gap, this positron may form positronium with probability P_{Ps} that is, in general, a function of the kinetic energy of the inner positron. Given that ground state positronium is formed with equal likelihood in the singlet state or in one of the three triplet states, only the 75% of the total amount of positronium formed is ortho-positronium. In our simulation we do not consider the possibility of positronium formation in the bulk of Alumina as experimentally found by S. Van Petegem [41]. Neither implement the thermalization of positronium in the Whatman® membrane nanochannels or the positronium formation in the space between alumina grains. The simulated positronium energy spectrum and angular distribution for Alumina are shown in figure 3.2.

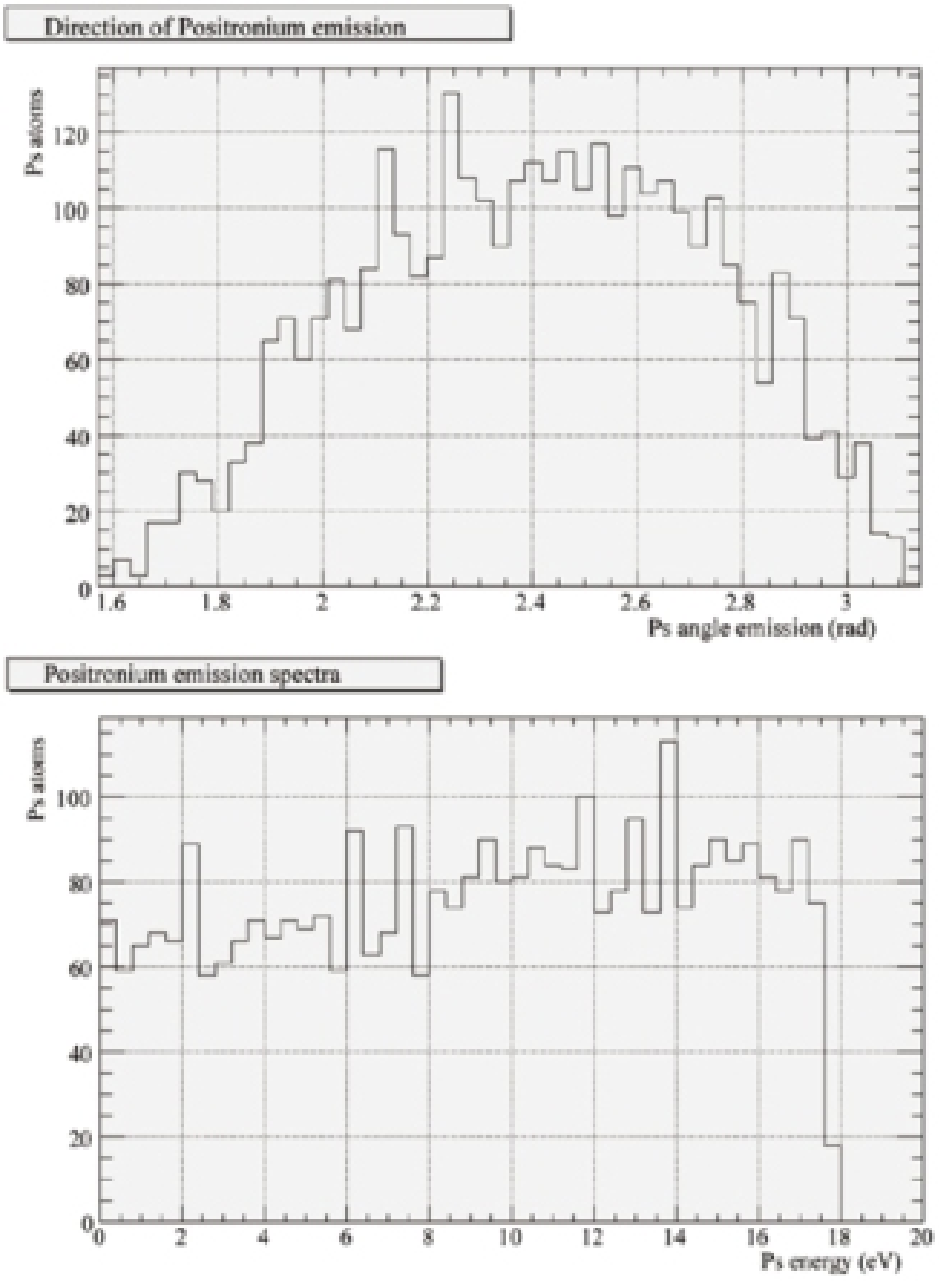

Figure 3.2: Positronium energy spectrum and angular distribution for positrons implanted in Alumina (Al_2O_3). Angles are referred to the positron ingoing direction. The $18eV$ cut-off in energy is due to the the maximum positronium energy permetted by the Ore gap model.

Extension to amorphous SiO_2 and limits of Monte Carlo simulations

After the production of the more promising oriented Si/SiO_2 nanochannels target by the Trento group (see section 3.4.7), we decided to extend the Monte Carlo simulation described in my Master thesis to amorphous silicon dioxide SiO_2 (Silica). Unfortunately the Monte Carlo simulation of Positronium formation in Alumina shows many inaccuracies especially in the Stopping Profile determination. We think that the main problem is due to the simulation method used in the $> 20eV$ energy range (continous slowing down approximation). In fact it may lead to erroneous results, since straggling is neglected, i.e. the fact that energy is actually lost in discrete collisions [37]. The number of such collisions fluctuates statistically on a given path length and the energy loss ΔE in each collision varies in accordance with a probability distribution corresponding to the inelastic differential cross section. A detailed simulation of the energy loss process is therefore necessary in order to obtain accurate results and realistic energy loss distributions at low and intermediate energies. In order to achieve these conditions we studied the possibility to extend the detailed description previously used for positron energy lower then $20eV$ to the overall positron energy range, using the "straggling energy" simulation method [36]: at each interaction vertex the positron can interact elastically or inelastically according to its differential cross sections. This method was already developed for Silica by M. Dapor in the energy range between few keV and few tens eV [42]. In figure 3.3 the stopping profile[4] for positrons in amorphous Silica is shown.

Below $10eV$: "hic sunt leones". In fact we don't have any semi-classical realistic models[5] that are able to theoretically describe what happens below that energy. The open problems are many. In a quantum mechanical view of the problem, the positron wavefunction increases its dimension when the velocity of the positron decreases. This spatial delocalization of the positron, useful in order to describe the increase of annihilation probability at rest, force it to interact at the same time with many molecules or atoms. The two body interaction (free wave-packets approximation) fails and we must use a multibody approach. In our simulation with Alumina, in order to overcome this problem, an "effective theory" in which the multibody interaction theory is approximated by an effective single interaction model was used. The delocalization of the wavefunction moreover induces us to consider the interaction of the positron not only with free molecules and atoms but with the whole solid. In this condition also the Born approximation for the computation of the differential elastic cross section fails. We don't actually know neither theoretically nor experimentally of any important quantity

[4] That is the probability to find a positron at $< 10eV$ in energy in function of penetration depth.

[5] We don't consider quantum Monte Carlo simulations

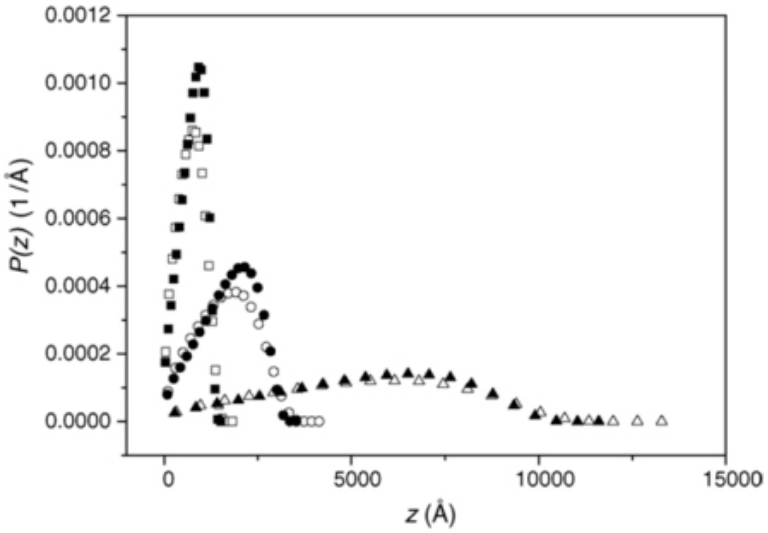

Figure 3.3: M. Dapor Monte Carlo calculation of the stopping profiles P(z) of electrons (empty symbols) and positrons (filled symbols) in SiO2 as a function of z, the depth inside the solid measured from the surface. The primary energies of the particles are: 3 keV (squares), 5 keV (circles) and 10 keV (triangles).

about positronium formation and diffusion in solids. In particular, in Silica rather than Alumina we have positronium formation not only on the target surface but also in the bulk of the solid [43]. This positronium atom can therefore diffuse like a neutral gas till the surface. As such it interacts with the solid bulk. The processes available at the surface are not so clear. In this condition it is impossible, at the moment, to develop a semi-classical Monte Carlo simulation of positronium formation in SiO_2 and more generally in solids in order to predict the energy spectrum and directionality of the emitted positronium. In future probably it will be possible to study quantum Monte Carlo or multibody models in order to parametrize the interactions of positron at very low energy (few eV). In addition, experimental measurements like Time of Flight (TOF) of positronium emitted from solids or measurements of directionality, are also necessary in order to have more experimental constraints.

3.2.4 Positronium thermalization in porous media

Positronium formation in porous media is especially interesting. A material can have pores not connected to the surface or a network of pores (ordered or not ordered) connected to the surface. Positronium formed in the bulk can diffuse into a pore or we can have positronium formation at the pore surface. If the pores are connected to the surface of the material then the

positronium can escape toward the vacuum following the pore channels and colliding with the pore walls. The energy spectrum of the emitted positronium depends on the energy of the positronium entering the pore, on the number of collisions with a pore surface and on the mean energy loss for each collision. Trough this processes it is possible to reduce the positronium energy from a few eV to a few meV [44]. This is one of the two requirements of the AE$\bar{g}$IS laser excitation system: few meV positronium atoms in a small dimension cloud (of the order of few millimeters). As seen previously, we are interested only in the fraction of positronium emitted as ortho-positronium. Annihilation of the ortho-positronium by pick-off [45] with the pore walls can not be avoided but the total pick-off loss is expected to remain at the tolerable level of 60%-70%. Moreover has given that the depth in the bulk where positronium is formed depends on the positron energy, with an appropriate design of the pore geometry and by controlling the implantation depth through the positron implantation energy, we will be able to tailor the energy spectrum of the emitted positronium to match the required values and possibly give directionality at the positronium cloud in order to increase the solid angle efficiency for the laser excitation. Some of this aspects, supported by experimental results obtained by the collaboration, will be treated in the next sections.

3.3 Positronium detection

The understanding of the directionality of the emitted ortho-positronium, its energy spectrum and its yield are the main goals of the AE$\bar{g}$IS converter R&D. The first two requests need Time Of Flight measurements (TOF) that, up to now, are only partially available[6]. The measurements of positronium formation yield were performed by means of a monoenergetic positron beam[7] using the well-known "3γ method" described in subsection 3.3.3.The amount of positronium emitted in vacuum depends on the pick-off annihilation reduction that is the size of pores or channels. This quantity can be experimentally obtained by Positron Annihilation Lifetime Spectroscopy measurements as described in subsection 3.3.1.

3.3.1 Positron Annihilation Lifetime Spectroscopy

PALS (Positron Annihilation Lifetime Spectroscopy) is a technique that allows to analyse the microscopic structure of a given material by ortho-positronium lifetime measurements. When a positron interacts with matter it can undergo a free annihilation $e^+ + e^- \rightarrow \gamma + \gamma$ or form positronium in voids or in the bulk of the solid [31] $e^+ + e^- \rightarrow Ps$. If the ortho-positronium

[6]Some TOF measurements are achieved at Trento laboratory by R. Brusa et al.
[7]L-NESS laboratory in Como. For more information http://lness.como.polimi.it

can not escape from the solid, it is subject to pick-off effects. This effect is the detection of premature annihilations when positrons are "picked off" by free electrons from an enclosing surface. Suppose that two positronium atoms are trapped in an arbitrary material, one in a large hole (or pore) and one in in a small pore. As the positronium atoms move in their pores, the positron within the atom has a chance to pick off electrons from the material, causing a premature annihilation. The likelihood of the pick-off effect is determined by the characteristics of the pore, so the atom in the small pore should have, on average, a shorter lifetime than the one in the large pore. From the lifetime data, you can infer information about the surroundings of the atom. Most part of the positron annihilation take place in two gamma with energy $511keV$ by free annihilation $e^+ + e^- \rightarrow \gamma + \gamma$, by para-positronium decay $pPs \rightarrow \gamma + \gamma$ and by pickoff ortho-positronium $oPs + e^- \rightarrow \gamma + \gamma + e^-$. This two annihilation gamma are emitted in opposite directions in order to conserve energy and momentum. In addition, if the positron is produced by a Sodium-22 radioactive decay there is a $1280keV$ gamma associated to the positron emission. Therefore, we can compute the positron or positronium lifetime in the solid as the delay time between the $1280keV$ (start) and a $511keV$ (stop) gamma detection. In this procedure we neglect the time between the emission of a positron and the $1280keV$ gamma (about $2-3ps$) and the time between the emission of a positron and its implantation in the solid (about $20-30ps$). If the solids have sets of pores with about the same dimensions the overall positron annihilation lifetime is a weighted sum of lifetimes given by free, para-positronium and pick-off ortho-positronium annihilations. If we don't have losses of positronium atoms in void the weight of lifetime components is the amount of positronium formation in the sample. Vice versa if we measure the positron lifetime components we obtain information about the pore dimensions using for example the Tao-Eldrup model [46]. PALS is therefore an important tool in order to measure the dimensions of converter voids like nano-channels or pores. Given that the AE$\bar{g}$IS converters emit a lot of positronium in vacuum we can't use PALS for positronium yield measurements. During my PhD activity I studied also the positronium formation in Pseudocumene with PALS technique, as reported in the following.

PALS apparatus in the Milano Politecnico Positron Laboratory

Positrons are generally obtained from ^{22}Na, a radioisotope which also emits a prompt γ-ray with an energy of $1280keV$. This start signal marks the birth of the positron. The stop signal is given by one of the annihilation photons (0.511 MeV): most of the annihilations occur into two gamma rays. The source strength is typically 0.04 to 0.8 MBq, and the source is prepared by depositing a droplet of an aqueous solution containing ^{22}Na on a thin metallic foil or plastic sheet; after drying the residue is subsequently covered by an

identical support and sealed, to obtain a reusable source. A typical support is the polymide Kapton; its use is advantageous since Ps does not form in it and subtraction of positrons contribution to the total time annihilation spectrum is therefore rather simple [47]. The source is inserted between two layers of the sample to be investigated ("sandwich" configuration) whose thickness must be sufficient to stop 99.9 % of the injected positrons (the range of positrons in matter from a ^{22}Na source is about $170 mg/cm^2$ [48]). A schematic diagram of a PALS time spectrometer is shown in Figure 3.4.

The time spectrometer is formed by two detector channels: each channel consisting of a scintillator coupled to a photomultiplier tube (PMT); the scintillator converts the start or stop γ-ray into UV photons which are absorbed by the window of the PMT producing the emission of photoelectrons. Most commonly used scintillators are organic (plastic) or inorganic (BaF_2). The resulting photoelectrons are multiplied by a series of intermediate dynodes, in order to obtain a sufficient voltage pulse at the output of the PMT anode; the resulting voltage is proportional to the energy of the γ-ray emitted by the scintillator. Discrimination between start and stop events occurs on the basis of the different energies of the detected γ-ray: a constant fraction discriminator (CFD) on each channel of the spectrometer generates a fast timing signal whenever a γ-ray with the correct energy is detected. A time-to-amplitude converter (TAC) enabled by the start signal from the CFD produces a voltage linearly increasing with time, which stops at the arrival of the stop signal from the other CFD: the available signal at the output of the TAC is therefore proportional to the time interval elapsed between generation and annihilation of the positron. This signal is digitized by a analog-to-digital converter (ADC) and transferred to the memory of a personal computer (PC). Each memory channel corresponds to a voltage ΔV and contains the annihilation events occurring within a specified time interval Δt. Linearity of the apparatus guarantees constancy of the ratio $\Delta t/\Delta V$, which can be easily confirmed through a calibration procedure. Recently certain of the electronic units (CFD and TAC) have been replaced by digital counterparts [49][50]: signals from the PMT are digitized by means of ultra-fast modules. Digitized pulses are stored in a personal computer and analysed off-line by software; digital filters select pulses with suitable shape and amplitude. Improvement in timing resolution is obtained with respect to the standard configuration of the positron lifetime set-up, without decreasing the counting rate [51]. Furthermore, it is possible to accumulate two independent lifetime spectra at a time, by exploiting each detector as source of start and stop signals. Introduction of ultra-fast digitizers represents a real milestone in the PALS technique. The annihilation lifetime spectrum assumes the form of an histogram (generally containing from one million to several millions of counts) which can be analyzed by means of a computer program. The experimental spectrum is the convolution of the intrinsic spectrum with a resolution function, that is, a function describing

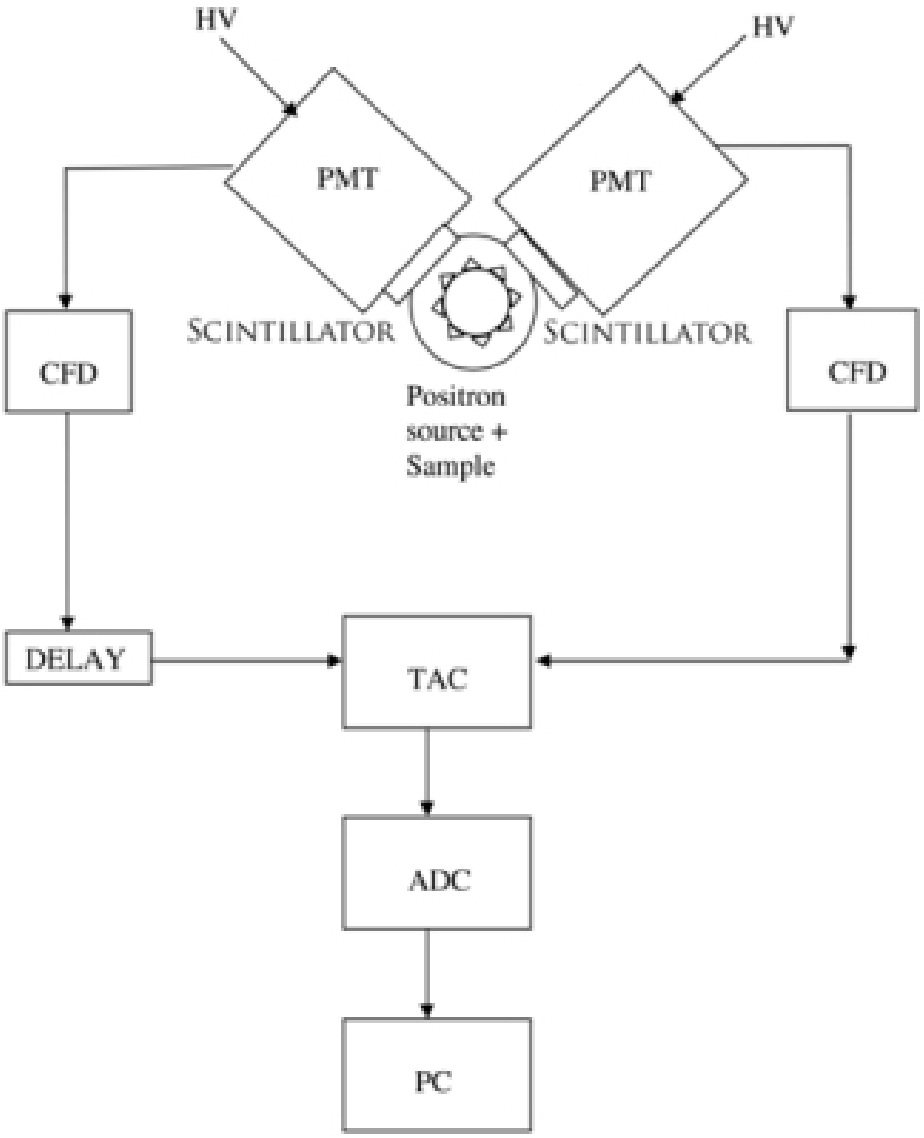

Figure 3.4: Milano Politecnico Positron Laboratory PALS apparatus' scheme.

the response of the apparatus to two simultaneous events. This can be obtained [48] from the time spectrum of ^{60}Co, which decays by emitting two gamma rays with similar energies (1.33 and 1.17 MeV) within a time interval of about 0.7 ps. The two events can be considered simultaneous on the typical time scale of PALS and the corresponding time spectrum is often assumed to represent the resolution function of the positron annihilation lifetime spectrum, although the energy of the annihilation photon is rather different with respect to the ^{60}Co gamma rays. In fact, the full width at half maximum (FWHM) for a time spectrum with 1.274 and 0.511 MeV gammas is larger (by a factor of about 1.1) than that for 1.17 and 1.33 MeV gammas. A better approach is to use the time spectrum of ^{207}Bi, which decays to an excited state of ^{207}Pb with half life of 30 years. In the de-excitation process of ^{207}Pb to the ground state two gammas, with respective energies of 1.06 and 0.57 MeV, are emitted, with a lifetime of 182 ps. The energies of the two photons are very near to those corresponding to the start and stop photons in PALS. Deconvolution of the ^{207}Bi time spectrum with a single fixed lifetime provides a realistic resolution function, which may be represented by a single gaussian or a sum of gaussians with different centroids and weights; values between 150 and 300 ps are quite common for the FWHM of the resolution function. Various computer codes are available [52][53][54] [55] to analyse the annihilation lifetime spectrum in terms of different components, each corresponding to a particular positron state. A PALS spectrum consists thus of the sum of a number of components, which can be treated as *discrete* or and *continuous*. In the first case, each annihilation component is an exponential function of the form $\frac{I}{\tau}e^{-\frac{t}{\tau}}$, each characterized by a lifetime τ and an intensity I. The intrinsic spectrum $S(t)$ can be written:

$$S(t) = R(t) \otimes \left[\sum_{i=1}^{N} \frac{I_i}{\tau_i} e^{-\frac{t}{\tau_i}} + B \right] \tag{3.2}$$

where $R(t)$ is the resolution function and B is the constant background, representing the spurious coincidence events, to be subtracted during the fitting procedure. The symbol $\otimes$ stands for the convolution operation. PALS analyses in terms of three components (that is, $N = 3$) are quite common. Typical lifetimes of free positrons (i.e., those that do not form Ps) in polymers are around 0.4 ns. p-Ps lifetimes in condensed matter are usually below 0.15 ns; o-Ps shows the longest lifetimes, generally in the range 1-10 ns. A continuous PALS spectral component is constructed as a continuous sum of discrete components and is characterized by three parameters: the intensity and the first two moments of the distribution of lifetimes, that is, the centroid (mean lifetime) and second moment (standard deviation from the mean lifetime). A distribution of o-Ps lifetimes is expected in a polymeric material, and will depend on the hole volume distribution present in the amorphous zones. Both the computer programs MELT [54] and CONTIN

[53] analyse the time annihilation spectrum only in terms of continuous components, without any guess as to the shape of the distributions. Conversely, the code POSITRONFIT [52] provides analyses only in term of discrete components. The program LT [55] is also able to provide for eventual distributions of lifetimes (assuming a log-normal distribution) and can be used for a mixed analysis, in the sense that each component can be chosen to be discrete or continuous. Of course, the statistics of a spectrum must be substantially higher than as in the case of discrete component, if continuous components are to be accurately resolved.

As an application of these techniques we present a study of the effects of the otrhopositronium formation in organic liquid scintillators on electron anti-neutrino detection. This study was made as a part of my PhD program.

3.3.2 Technical application: effects of the oPs formation in organic liquid scintillators on electron anti-neutrino detection

Electron anti-neutrinos are produced in β decays of naturally occurring radioactive isotopes in the Earth, representing a unique direct probe of our planet's interior. Also nuclear reactors provide intense sources of antineutrinos, which come from the decay of neutron-rich fragments produced by heavy element fissions. Electron anti-neutrinos are often detected with the reaction:

$$\nu_e + p \rightarrow n + e^+ \tag{3.3}$$

by looking at the neutron-positron coincidence.

Organic liquid scintillators:

- Neutrons are captured mainly on protons, and identified looking at the characteristic $2.23MeV$ gamma ray emitted in the reaction:

  $$n + p \rightarrow d + \gamma \tag{3.4}$$

  The neutron mean capture time varies from few up to hundreds microseconds.

- Positrons interacting in liquid scintillator may either annihilate with electrons or form positronium (Ps). In condensed matter, however, interactions of otho-positronium with the surrounding medium strongly reduce its lifetime: processes like chemical reactions, spin-flip (ortho-para conversion at paramagnetic centers), or pick-off annihilation on collision with an anti-parallel spin electron, lead to the two body decay with lifetimes of a few nanoseconds. The surviving three body decay channel $oPs \rightarrow \gamma + \gamma + \gamma$ is typically reduced to a negligible fraction (ortho-positronium can not excape in vacuum). If the delay introduced by the positron annihilation lifetime is of the order of a

few nanoseconds, calorimetric scintillation detectors, like Borexino [56] and KamLAND [57], are unable to disentangle the energy deposited by positron interactions from that released by annihilation gamma rays. In these cases, a delayed gamma ray emission induces a distortion in the time distribution of emitted scintillation photons (*pulse shape*), with respect to a pure annihilation event. Such distortion can affect algorithms based on the pulse shape, like the position reconstruction and the particle discrimination. As second order effect, positron energy reconstruction can be distorted if a correction based on the energy dependency on position is applied.

Thus we have characterized the o-Ps formation probability (o-PsFP) and lifetime for the most popular choices of scintillator solvents among the present experiments, as shown in Table 3.1.

Experiment	**Scintillator**	**Fluor**	**Dope**
KamLAND	20% PC 80% OIL	$1.5 g/l$ PPO	
Borexino	PC	$1.5 g/l$ PPO	
LVD	Paraffin	$1.0 g/l$ PPO	
SNO+	LAB	PPO	0.1% ^{150}Nd
Double Chooz	20% PXE 80% OIL	$3-6 g/l$ PPO $20 mg/l$ Bis-MSB	0.1% Gd
Daya Bay	LAB	$3 g/l$ PPO $15 mg/l$ Bis-MSB	0.1% Gd
RENO	LAB	$1-5 g/l$ PPO $1-2 mg/l$ Bis-MSB	0.1% Gd

Table 3.1: Scintillator composition used in present and future underground neutrino experiment.

In particular, we studied the following solvents: 1,2,3 trimetilbenzene or pseudocumene (PC, C_9H_{12}), linear alkyl benzene (LAB, $C_{18}H_{30}$), phenylxylylethane (PXE, $C_{16}H_{18}$) and dodecane (OIL, $C_{12}H_{26}$). Wavelength shifters are present in scintillators with very low concentrations. However, adding a fluor to scintillators can change the o-Ps properties. For this reason we studied a typical scintillator mixture, $PC+1.5 g/l$ of PPO (2,5-diphenyloxazole), to observe the effect of the fluor on the o-Ps. The apparatus used for the measurements is the one described in section 3.3.1. The source was prepared by drying a droplet of ^{22}Na from a carrier free neutral solution between two Kapton foils ($7.5 \mu m$ thick, $1 cm$ radius each single layer) which were afterwards glued together. In order to avoid damage of the radiative source by the liquid sample under investigation, we covered the Kapton backing by another pair of Kapton foils. We chose Kapton since it is a polymide com-

patible with scintillator materials and where positrons do not form Ps. The source has an activity of 0.8 MBq. The Kapton-source sandwich is poured in a glass vial, containing the scintillator sample. The vial is positioned between the two plastic scintillator detectors.

Data analysis and results The 5 samples of scintillator solvents (PC, PXE, LAB, OIL, PC+PPO) have been degassed with nitrogen. For each sample, we repeated the measurement from 3 to 5 times, to observe possible systematic effects, collecting a total statistics for each sample larger than $4 \cdot 10^6$ events. Examples of collected spectra are shown in Figure 3.5.

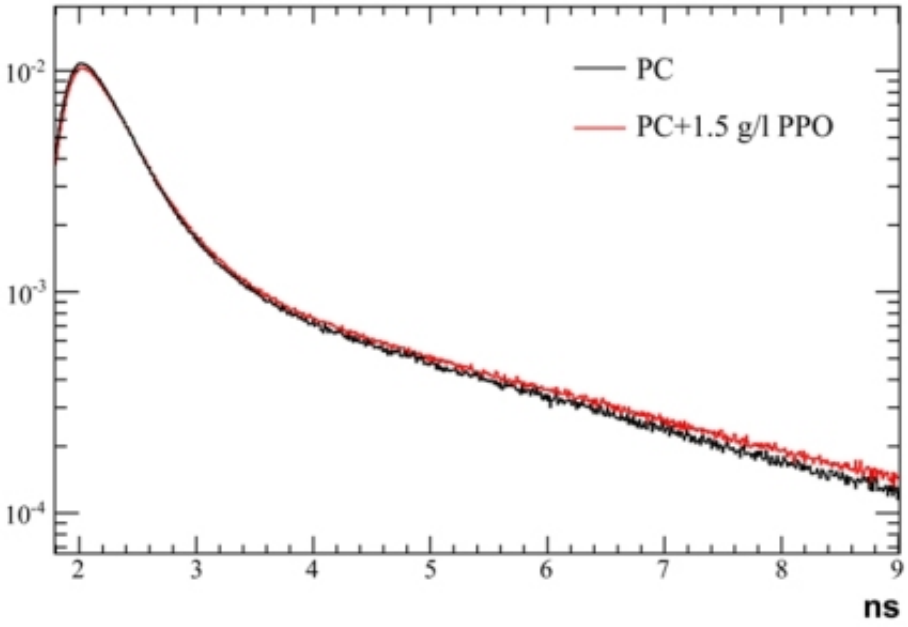

Figure 3.5: Examples of PAL spectra for the PC and PC + $1.5g/l$ PPO samples. The difference in shape is due to the different positronium lifetime in the two samples.

Data are fitted with a two component model (see section 3.3.1):

$$F(t) = \Theta(t_0) \cdot \left[\sum_{k=1,2} \frac{A_k}{\tau_k} \cdot e^{-\frac{t}{\tau_k}} + C \right] \tag{3.5}$$

where A_1 and τ_1 correspond to the amplitude and mean life of the free annihilation $e^+ + e^- \rightarrow \gamma + \gamma$ and p-Ps component $pPs \rightarrow \gamma + \gamma$, A_2 and τ_2 refer to the o-Ps one $oPs + e^- \rightarrow \gamma\gamma + e^-$, and C is the noise and background constant component. t_0 is the detector offset. $\Theta(t_0)$ is the Heaviside step

function in t_0. The fit function $F(t)$ is convoluted with the resolution of the apparatus, modelled with the sum of two gaussians:

$$G(t) = \sum_{i=1,2} \frac{g_i}{\sqrt{2\pi\sigma_i^2}} \cdot e^{-\frac{t^2}{2\sigma_i^2}} \tag{3.6}$$

centred in the same value but with different resolutions (σ_1 and σ_2), and where $g_1 + g_2 = 1$. The detector resolution is dominated by the first component with $\sigma_1 \cong 110ps$ ($g_1 \cong 0.8$), while $\sigma_2 \cong 160ps$. The data modeling package used in this analysis is the RooFit toolkit, embedded in the ROOT package, based on MINUIT [58]. All the parameters in the model are free in the fit, and all the fits to the data samples produced a normalized χ^2 in the $0.85 - 0.98$ range. The parameter τ_1 is almost constant in all the measurements: the mean value is centered around $365ps$, with a root mean square of $8ps$. An example of fit for the PXE sample is shown in Figure 3.6.

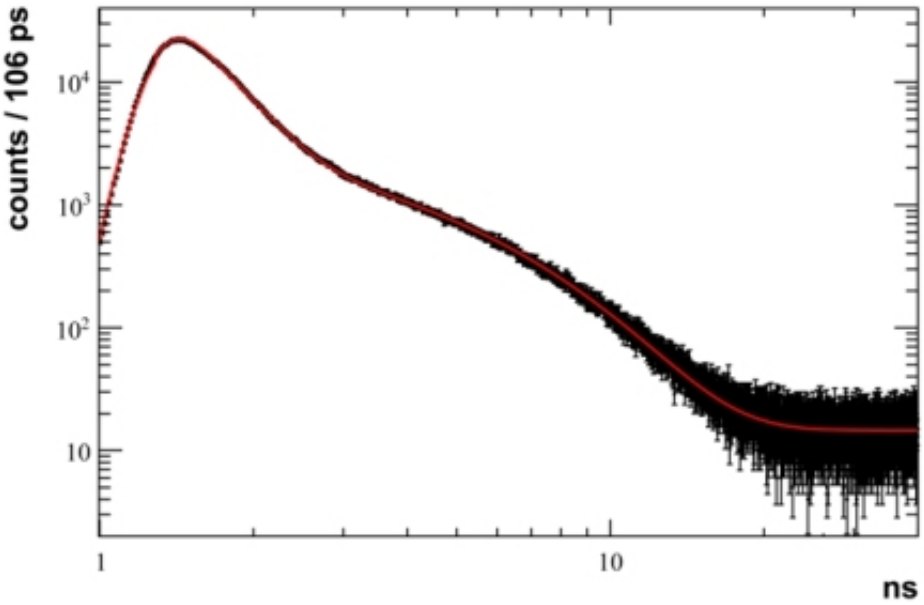

Figure 3.6: Fit (red line) of the positron annihilation life time spectrum (black dots) for the PXE sample.

We made an attempt to add an exponential component to the model, to disentangle free annihilation from p-Ps, but the fit was not able to determine the minimum. To estimate the fraction of positrons annihilating in Kapton, we covered the ^{22}Na source with 1 to 3 Kapton layers. The Kapton-source sandwiches were inserted in a Plexiglas medium, characterized by an o-Ps mean life of $\cong 2ns$ and the atomic number Z compatible to the scintillators'

ones. The surviving o-Ps fractions in Plexiglas, after crossing the Kapton layers, are shown in Figure 3.7.

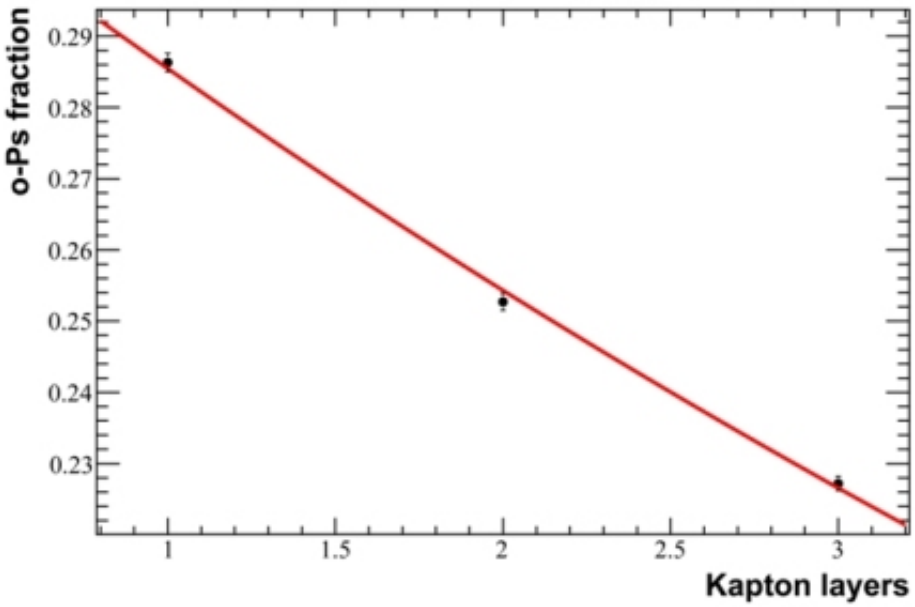

Figure 3.7: Dots represent the o-Ps fraction, survived to 1 to 3 Kapton layers, inserted in a Plexiglas medium. Each layer is $7.5\mu m$ thick and $1cm$ radius. The line is the result of an exponential fit.

By fitting the obtained fractions with an exponential law, we estimated that $20.6 \pm 0.2\%$ of positrons annihilate in the double Kapton layer ($15\mu m$ thick), used to characterize the scintillator samples. The normalized o-Ps fraction is then:

$$f_2 = \frac{A_2}{A_1 + A_2 - A_K} \tag{3.7}$$

where A_K is the Kapton component. For each sample, we evaluated the weighted average, with the correspondent statical error, for both the o-Ps fraction and mean life. To estimate the systematic errors, we fitted with a gaussian, in a likelihood approach, the deviations of each measurement from the weighted average. The systematic errors for the o-Ps fraction and mean life are 0.5% and $0.03ns$, respectively. Final results are shown in table 3.2.

Pulse shape distortion All the samples analysed are characterized by an o-Ps mean life around $3ns$ and a formation probability (FP) around 50%. The o-Ps τ and FP for PXE and LAB represent the extremes in the value ranges: PXE (LAB) is the solvent where o-Ps has the lowest (largest) probability to be formed and the shortest (longest) life time. However, the impact

Material	f_2 [%]	τ_2 [**ns**]
PXE	0.466 ± 0.005	2.74 ± 0.03
LAB	0.542 ± 0.005	3.08 ± 0.03
PC	0.485 ± 0.005	2.96 ± 0.03
OIL	0.506 ± 0.005	3.04 ± 0.03
PC + $1.5g/l$ PPO	0.512 ± 0.005	3.12 ± 0.03

Table 3.2: Final results for the formation probability of ortho-positronium and corresponding mean life for the analysed samples of scintillators.

of the o-Ps formation in scintillator on the positron event reconstruction, and hence on the anti-neutrino detection, depends also on the positron energy and on the scintillator decay time. Positrons and annihilation gammas can not be disentangled in organic scintillator detector since the fastest component of the fluorescence decay-time constants (table 3.3) is of the order of few nanoseconds.

Scintillator	Δt_1 [**ns**]	Δt_2 [**ns**]	Δt_3 [**ns**]	N_1 [%]	N_2 [%]	N_3 [%]
PC $1.5g/l$ PPO	3.57	17.61	59.9	89.5	6.3	4.2
PXE $1.0g/l$ PPO	3.16	7.7	34	84.0	12.0	2.9
LAB $1.0g/l$ PPO	7.46	22.3	115	75.9	21.0	3.1

Table 3.3: Scintillator decay constants Δt_i for β particles for PC + $1.5g/l$ PPO [59], PXE + $1.0g/l$ PPO [60], LAB + $1.0g/l$ PPO [60]. N_i are the scintillator amplitude for the given component.

In the positron detection, scintillator molecules are first excited by positron interactions, and then by annihilation gamma rays. If annihilation passes through the intermediate o-Ps state, the annihilation component is delayed, and the overall photon emission time distribution (PETD) results as the sum of the two components.

An example of PETD is shown in figure 3.8, for 0.5 MeV positrons in PC + 1.5 g/l PPO, annihilating after o-Ps formation. The correspondent deformation, with respect to the pure annihilation case, is dominant in the first $30ns$, as shown in figure 3.9.

The relative weights of the two components depend on the positron energy, which is related to the anti-neutrino energy. In order to estimate the deformation, we simulated positrons with energies from 0.1 to $5.0MeV$. The mean value of the so-obtained time distribution is a good estimator of the

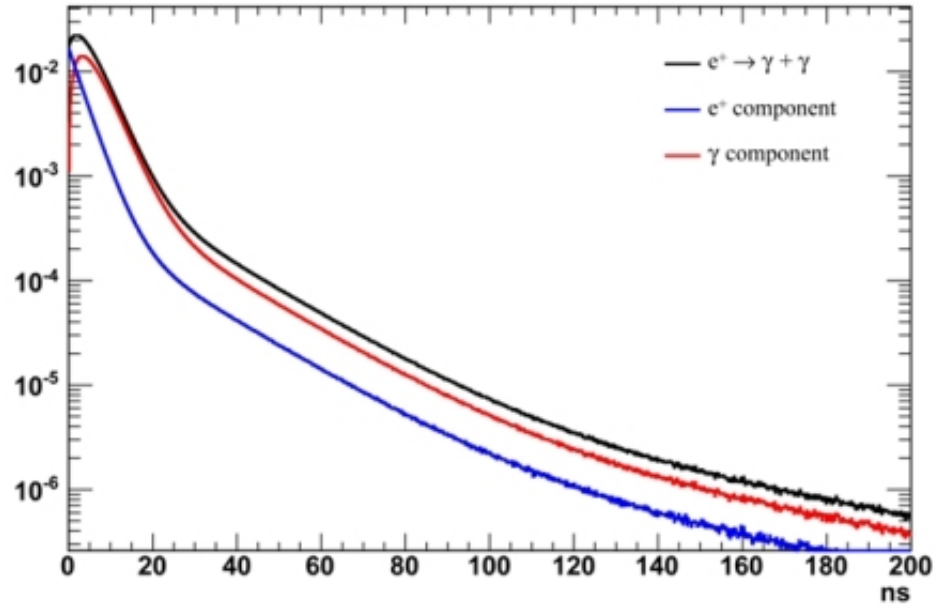

Figure 3.8: Simulation of the pulse shape induced by $0.5MeV$ positrons, all forming o-Ps, in PC. The positron and gamma components are also shown.

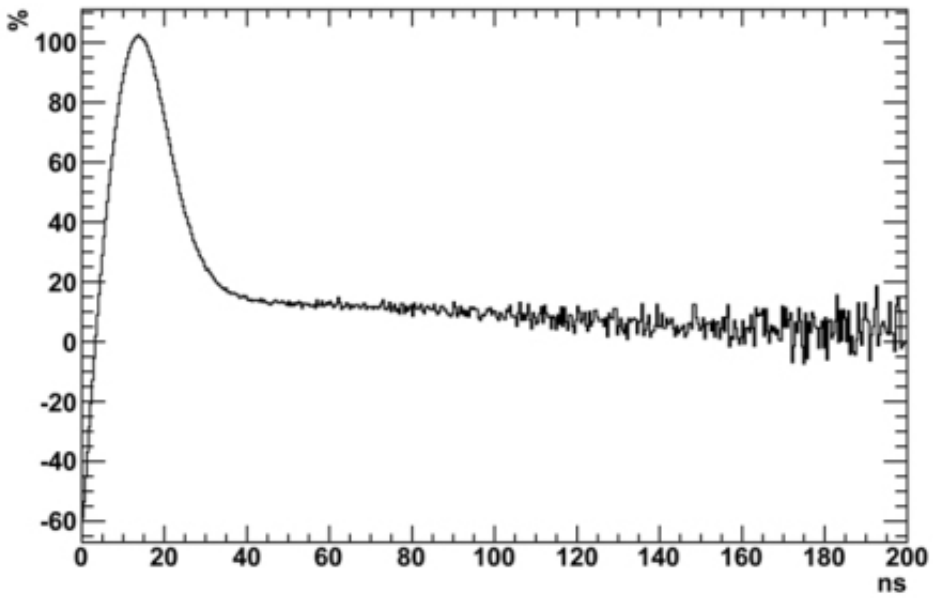

Figure 3.9: Distortion of the pulse shape in the o-Ps case with respect to the pure annihilation in PC for $0.5MeV$ electrons.

distortion. In figure 3.10, we show the ratio R between the mean values in the o-Ps case with respect to the pure annihilation one. It is noticeable that the deformation is stronger for lower energy positrons, and the mean value can be increased up to 50%. At larger positron energies, the distortion reaches a saturation, extending the mean value up to $10 - 20\%$.

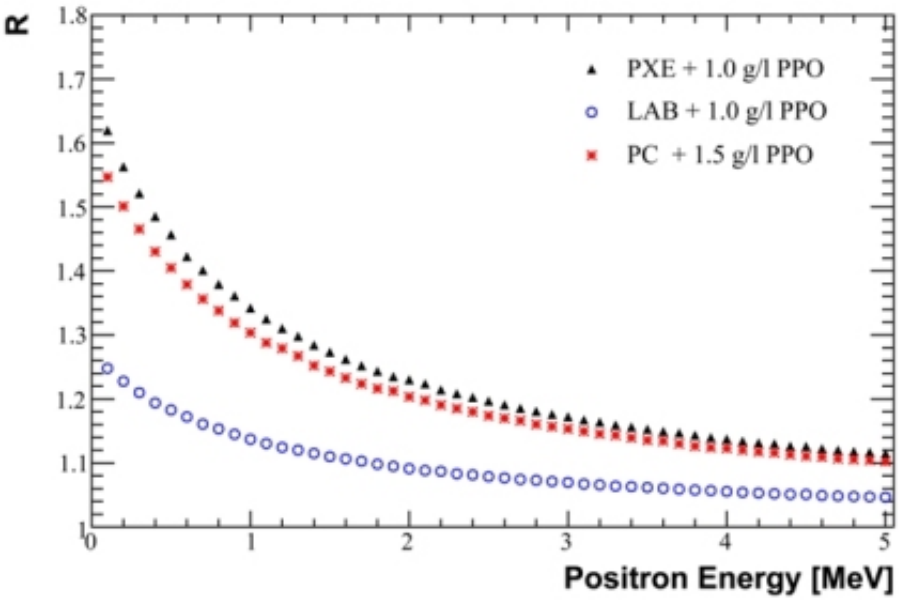

Figure 3.10: Ratio between the mean values of the o-Ps and annihilation pulse shapes as function of the positron energy for PXE + $1.0 g/l$ PPO, LAB + $1.0 g/l$ PPO, and PC + $1.5 g/l$ PPO.

3.3.3 Determination of ortho-positronium yield formation

In order to obtain the ortho-positronium yield we must have an accurate determination of the fraction of those positrons which form positronium. We assume that, when positronium is initially formed, the statistical weight will produce three times as much ortho-positronium than para-positronium. The para-positronium state decays into two photons in $125 ps$ with the energy of each photon being $511 keV$. If we assume no pick-off or spin exchange processes, the ortho-positronium exhibits primarily a three-body decay spectrum (i.e. three photons) decaying in $142 ns$ and producing a continuous

energy distribution given by (see Fig. 3.11):

$$P(E) = \frac{2}{N}\cdot\left[\frac{E\,(m_{e+}-E)}{(2\cdot m_{e+}-E)^2} - \frac{2\cdot m_{e+}\cdot(m_{e+}-E)^2}{(2\cdot m_{e+}-E)^3}\cdot\ln\left(\frac{m_{e+}-E}{m_{e+}}\right) + \right.$$
$$\left. + \frac{2\cdot m_{e+}-E}{E} + \frac{2\cdot m_{e+}\cdot(m_{e+}-E)}{E^2}\cdot\ln\left(\frac{m_{e+}-E}{m_{e+}}\right)\right] \qquad (3.8)$$

where m_{e+} is the positron rest mass, E is the gamma energy and N is the normalization given by:

$$N = \int_0^{m_{e+}} \frac{2}{N}\cdot\left[\frac{E\,(m_{e+}-E)}{(2\cdot m_{e+}-E)^2} - \frac{2\cdot m_{e+}\cdot(m_{e+}-E)^2}{(2\cdot m_{e+}-E)^3}\cdot\ln\left(\frac{m_{e+}-E}{m_{e+}}\right) + \right.$$
$$\left. + \frac{2\cdot m_{e+}-E}{E} + \frac{2\cdot m_{e+}\cdot(m_{e+}-E)}{E^2}\cdot\ln\left(\frac{m_{e+}-E}{m_{e+}}\right)\right] dE \qquad (3.9)$$

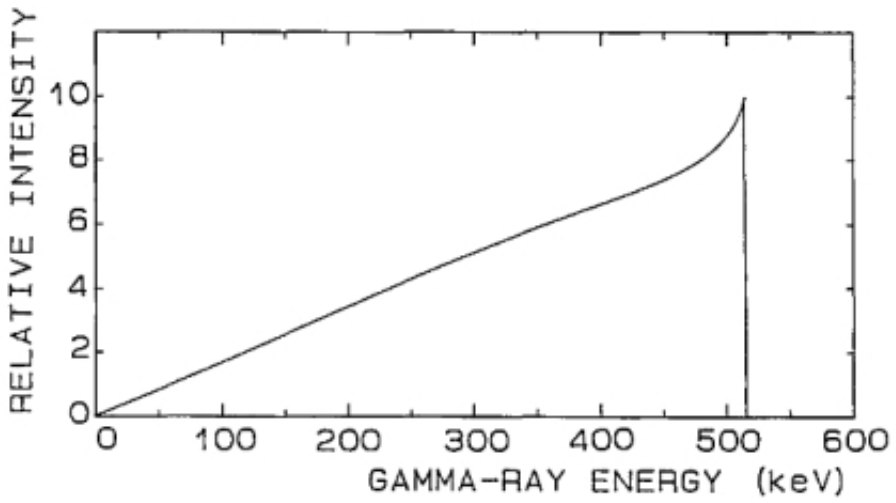

Figure 3.11: Theoretical energy distribution of annihilation radiation of the ortho-positronium three gamma decay in the region of $0 - 511keV$.

The sum of the energy of these three photons equals two times the mass of the positron at rest. The measured photon energy spectrum of these positrons, annihilating from the orto-positronium state, is markedly different from the two-photon process obtained when positrons decay by pickoff or from para-positronium state. The dissimilarities ascribed to positronium formation in the measured gamma ray energy spectrum from a single detector can easy be observed in figure 3.12. The single-detector method provides ease and a high-counting rate method for measuring the fraction of positronium formed in the target region f. However, it does require calibration points in the same geometry for both $f = 0$ and $f = 1.0$, i.e. for absence of

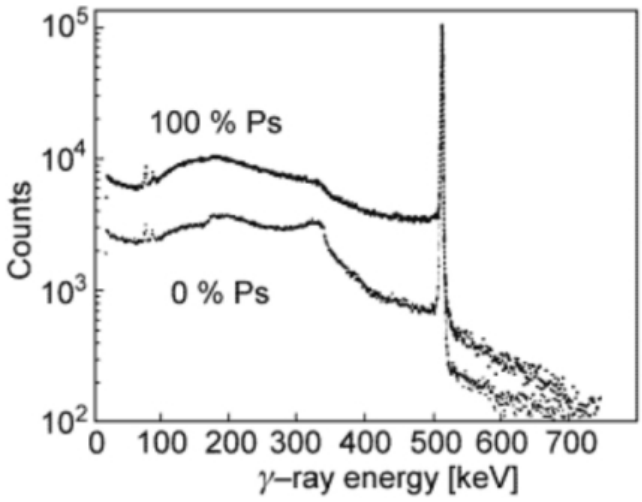

Figure 3.12: Experimental positron annihilation gamma spectrum in the case of 0% and 100% positronium formation yield. The spectra are normalized to the $511keV$ peak.

positronium formation or a fully positron to positronium conversion. The single-detector method, knows as "3γ method", was initially derived in the work of Marder et al. [61] We now indicate the total number of counts per unit time of the measured energy spectrum with T_F, and with P_F at the $511keV$ peak. This two quantities obey to the equations:

$$\begin{aligned} P_F &= N_a(1-f)g_p + fN_o g_o + fN_p g_p, \\ T_F &= N_a(1-f)h_p + fN_o h_o + fN_p h_p. \end{aligned} \tag{3.10}$$

The quantities N_a, N_p and N_o are the number of counts per unit time for the direct annihilation of positrons in the bulk or surface state, para-positronium annihilations and ortho-positronium annihilations, respectively. The quantity g_o and h_o represent, respectively, the average probability that a photon from the ortho-positronium decay will be counted in the peak or in the full energy spectrum. The average probability that an annihilation photon from a para-positronium decay will be counted in the peak region or in the total part of the energy spectrum are g_p and h_p, respectively. Direct positron - electron annihilations will be assigned the same average probability as that for the para-positronium. These probability factors depend upon the spatial distribution of annihilation events, resolution and absolute efficiency of the detector system, scattering events which cause degradation of annihilation photons (i.e. gamma ray absorbtion and scattering in the sample and sorrouding vacuum chamber) and the solid angle subtended by the gamma ray detector. One assumes that the same efficiency factors are used in all measurements. Now by forming the ratio $R_F = (T_F - P_F)/P_F$, one can use

equations 3.10 and solve for f obtaining:

$$f = \left[1 + \frac{P_1}{P_0}\frac{R_1 - R_F}{R_F - R_0}\right]^{-1}, \tag{3.11}$$

where the subscripts 0 and 1 correspond to P_F and R_F for 0% and 100% positronium formation, respectively. Experimentally R_1 and R_0 represent the parameter R_F measured on the surface of a Germanium single crystal at high temperature (where the implanted positrons back diffuse and form positronium) and in bulk of a Germanium single crystal (where no positronium is formed), respectively. When the Ps is formed inside the pores, the pick-off effect reduces the probability of three gamma annihilations by a factor

$$\epsilon = \frac{\lambda_{3\gamma}}{\lambda_{3\gamma} + \lambda_{p.o.}} \tag{3.12}$$

where $\lambda_{3\gamma}^{-1}$ is the three gamma annihilation rate in vacuum and $\lambda_{p.o.}^{-1}$ the pick-off annihilation rate. Thus the appropriate expression for the Ps fraction becomes:

$$F = \epsilon^{-1} f \tag{3.13}$$

where ϵ can be measured by PALS techniques (see subsection 3.3.1). We warn however that this formalism, which is adopted by other authors, is somewhat misleading, since the true fraction of positrons annihilated in three gamma is smaller by a factor 3/4. As previously said, the calibration of the parameters R_0 and R_1 depends on the experimental measurements of R_F made in a Germanium single crystal. The usual assumption is that we don't have ortho-positronium formation and we don't have at the detector (after background subtraction) gammas with energy between the $511keV$ peak and its relative Compton edge. Experimental measurements made at L-NESS laboratory, show instead that we can have events in this forbidden range. This is due to the Compton scattering of the annihilation gamma in the target. In particular it is possible to show that we have a dependence of R_0 and probably R_1 from the dimensions of the target and from its density. The results of our theoretical study and Montecarlo simulations are not presented in this thesis.

3.4 Positronium converter in AE$\bar{g}$IS

For the AE$\bar{g}$IS experiment, the overall yield of ortho-positronium and its precise degree of thermalization is critical. In particular, the anti-hydrogen charge-exchange cross section drops rapidly when the temperature of the ortho-positronium atom bocomes high. The energy of the positronium atoms must match the energy of the antiproton cloud, that is less than $100mK$. Besides, the number of anti-hydrogen produced in AE$\bar{g}$IS depends

from the number of ortho-positronium atoms emitted by the converter and laser excited. A schematic view of this part of the AE$\bar{g}$IS apparatus is shown in figure 3.13.

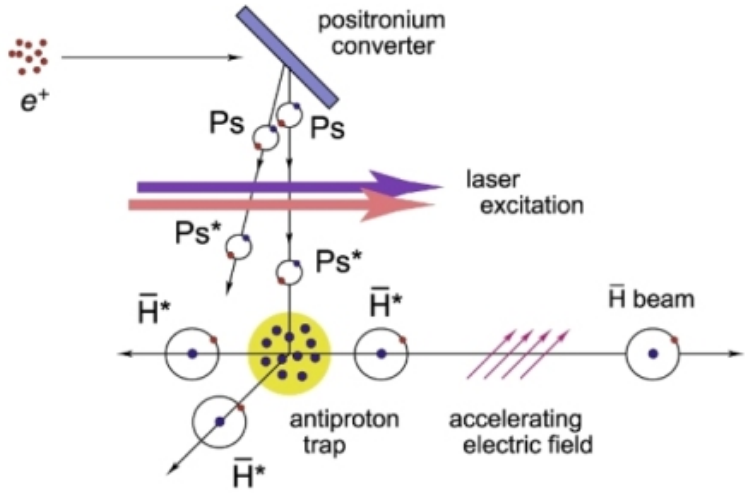

Figure 3.13: Scheme of the AE$\bar{g}$IS apparatus for antihydrogen production. The positrons are sent to the porous target and then converted to positronium atoms (Ps). Two laser pulses hit the positronium atoms in order to excite them. Rydberg positronium atoms (Ps^*) arrive to the antiproton traps where they can produce antihydrogen.

For the laser excitation process to be efficient the positronium cloud must be spatially localized and with appropriate velocity (corrisponding to few eV). The velocity depends upon the characteristics of the converter material, its pore structure, the implantation depth and the target temperature. The use of porous materials with pores connected to the target surface is fundamental in order to have positronium thermalization and emission. The use of metallic and semi-metallic converters would certainly be more efficient from the point of view of positronium cooling, since a single collision of a positronium atom with a free electron at the surface of the metal can produce a fractional energy loss of 50% thereby reducing the number of necessary collisions to less than about 100. On the other hand, pick-off annihilation losses in a metal are expected to strongly reduce the flux of ortho-positronium emerging from the pores. Nevertheless, the lack of experimental data on this subject suggests that one should not a priori abandon any attempt to use a metallic converter.

The AE$\bar{g}$IS collaboration is developping a new kind of porous metal targets made of compressed metal microspheres (see section 3.4.1). In these kind of converters the pores are connected each other and with the target surface, but are disordered. The ortho-positronium atoms are thus expected to be emitted isotropically in vacuum. The only way to compensate the ortho-

postronium loss by solid angle is by having a high positronium formation yield. Another problem is that disordered pores do not permit the tuning of the emitted ortho-positronium energy. In addition, this energy depends on the pore shape, its diameter and the positron penetration depth.

Insulators must also be considered. In this case the positronium formation yield is not too low and the pick-off annihilation losses do not reduce drastically the flux of the emitted ortho-positronium. Several groups have studied porous insulator materials with disordered and interconnected pores. In particular the AE$\bar{g}$IS collaboration is studying a wide set of converters with ordered and disordered porosity, i.e. Alumina with ordered nanochannels (Whatman® membrane), Vycor glasses, MOFs, aerogel/xerogel and MACS[62]. Insulators must however be considered with care because of space charge effect in the AEGIS experimental setup.

3.4.1 Metal/SiO_2 Microspheres

The Chemistry Department of the Università degli Studi di Milano is developing new kinds of porous metallic targets. The common idea, at the base of all these samples, is the compression of metallic micro-spheres in order to orbtain a compact solid with disordered voids in the bulk and (important for the experiment) on the surface. These targets should be able to form positronium that, after many collisions on the pores wall, can escape from the solid as cold ortho-positronium. The metallic nature of the sample prevents the possibility of electric breakdown triggered by the high positron density bunch in AE$\bar{g}$IS . Two TEM images of two microspheres targets (gold and silver) are shown in figure 3.14.

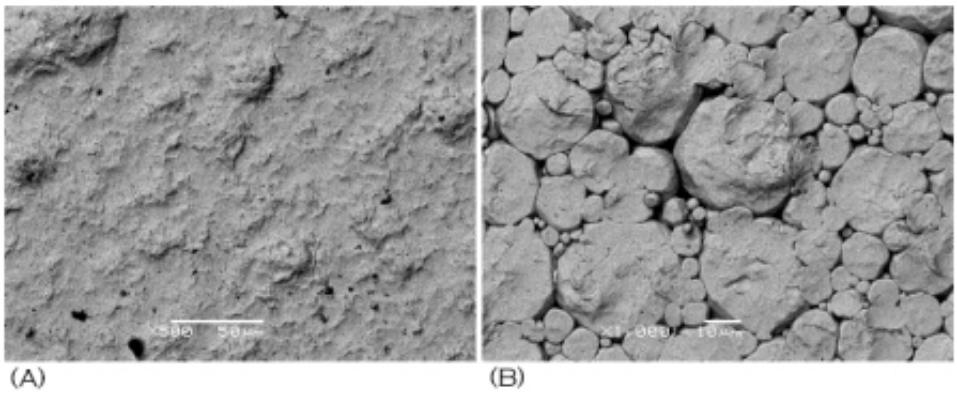

Figure 3.14: TEM picture of the gold (a) and silver (b) microspheres target surface.

Up to now, the AE$\bar{g}$IS chemistry group is studying the possibility to realize a solid target made of silicon oxyde microspheres compressed, with intrinsic nanoporosity [63]. Thus, this sample should present two set of

voids with two different diameter ranges: micro voids between the spheres and nano or subnano voids in the spheres as shown in figure 3.15.

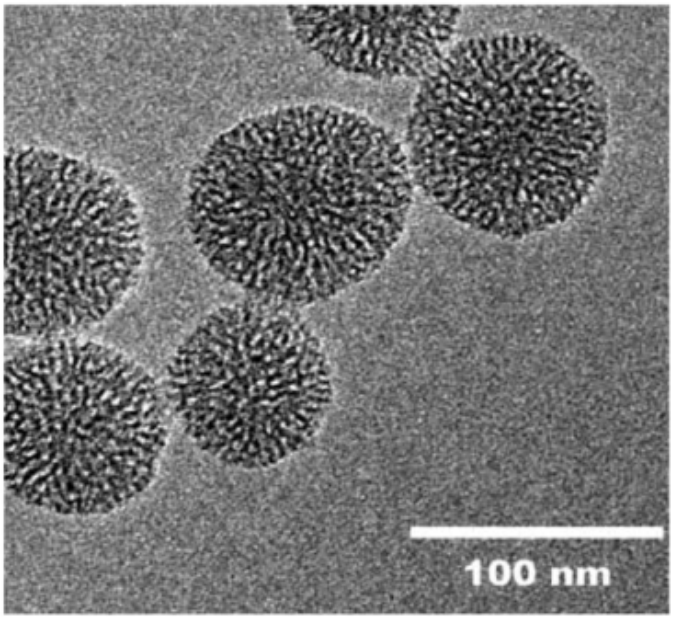

Figure 3.15: TEM picture of the porous silica microspheres condensate. The picture shows the two set of voids of this target: micro voids between the spheres and nano or subnano voids in the spheres.

3.4.2 Whatman® membrane

The Whatman® Anopore inorganic membrane is composed of high purity anodic alumina (Al_2O_3), electrochemically manufactured, with a precise, non-deformable honeycomb pore structure with no lateral crossovers between individual pores. This commercial membrane is supplied in the form of disks, bonded to an annular polypropylene ring. The minimum diameters of the pores is of about $20nm$. The target thickness is $60\mu m$. In figure 3.16, the pore structure of the Whatman® membrane is shown. Van Petegem et al. have demostrated experimentally that in single-crystalline Al_2O_3, bulk positronium is not formed but positronium emission from the surface has been observed [41]. This is in agreement with the observed positronium formation in polycristalline Alumina powders where the positronium formation is observed on the wall of the free volumes between the powder grains [64]. Thus in the Whatman® anopore membrane, the well-ordered channel porosity combined with positronium formation in the "bulk" of anodic Alumina samples would eventually lead to high positronium yield and positronium emission into vacuum. In a similar sample, N. Djourelov et al. [64], from

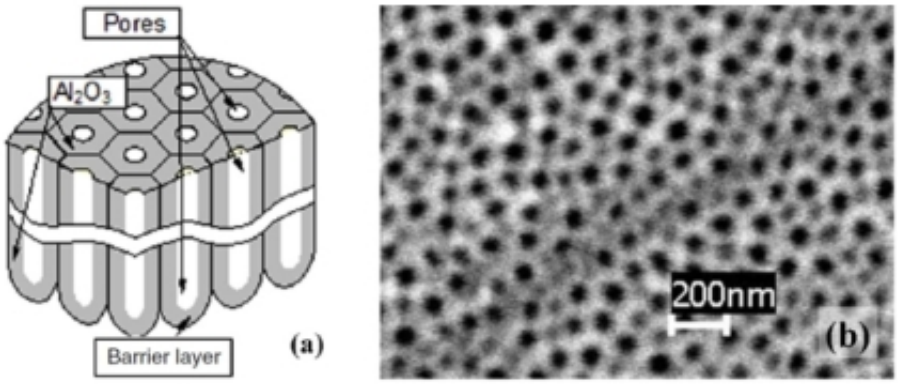

Figure 3.16: (a) Schematic representation of anodic alumina structure and (b) electron microscopy image of the surface of an anodic Al_2O_3 with pore's diameter of about $70nm$.

the 3γ method analysis, estimate that the 20% of all the injected positrons will form ortho-positronium.

3.4.3 Vycor glass

Vycor porous glass is an open cell, pourous glass formed by 96% of silicon dioxide. The homogeneous pore diameters can be controlled to average between 40 and 200 Angstroms. 3 γ measurements made in the Como L-NESS laboratory shows a positronium formation yield of about 10%-20%. Advantages of Vycor porous glass for positron to positronium converter include rigidity, chemical inertness, high temperature capability, superior thermal shock resistance, and controlled microporosity. In the other hand, electric breakdown is a disadvantage.

3.4.4 MOFs

Other materials considered as converters are the Metal-Organic frameworks (MOFs). These are crystalline compounds consisting of metal ions or clusters coordinated to rigid organic molecules to form one, two, or three-dimensional structures that can be porous (in our case we have a quasi-cubic grains with a side of about $50\mu m$). In particular we considered MOF-177. This kind of MOF consists of octahedral Zn4 carboxylate clusters linked to organic groups. Its surface area was determined to be an unprecedented $4500m^2/g$, which exceeds the surface areas of other MOFs, carbon materials, and zeolites. Its density is $4.27 \cdot 10^{-1} g/cm^3$. The open spaces are regular and have dimensions of a few nanometers. Figure 3.17 shows the structure of MOF-177. Potentially, the positronium formed in the open spaces can be drifted to the suface and thus emitted in vacuum. The regularity of the voids

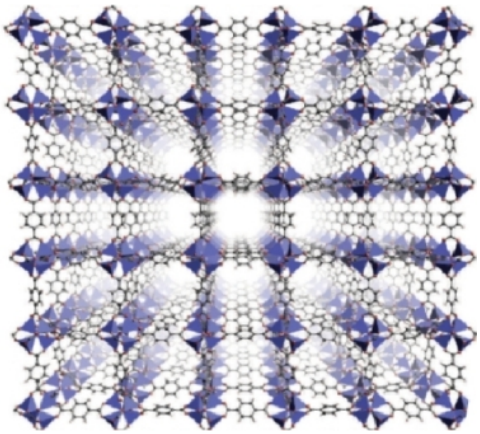

Figure 3.17: The Isoreticular Metal Organic Frameworks (IMOFS) MOF-177

may give directionality at the outgoing positronium. The 3γ measurements, made in Como L-NESS laboratories, show a formation positronium yield of about 5%-10%. We don't have, at the moment, measures in MOF-177 that indicate the directionality of the outgoing positronium atoms.

3.4.5 Aerogel/Xerogel

Aerogel is a manufactured material with the lowest bulk density of any known porous solid. It is derived from a gel in which the liquid component of the gel has been replaced with a gas. The result is an extremely low-density solid with several remarkable properties, most notably its effectiveness as a thermal insulator. Aerogel was first created by Samuel Stephens Kistler in 1931 [65], as a result of a bet with Charles Learned over who could replace the liquid in "jellies" with gas without causing shrinkage. The first aerogels were produced from silica gels. Kistler's later work involved aerogels based on alumina, chromia and tin oxide. Carbon aerogels were first developed in the late 1980s. The aerogel samples available to the AE$\bar{g}$IS collaboration are Aerogel-150 and AerogelC-20. The number indicates the aerogel density in mg/cm^3. The Aerogel samples of $20mg/cm^3$ were doped with C atoms (0.67% atoms of graphite). All aerogel used in AE$\bar{g}$IS are silica aerogel. Silica aerogel is the most common type of aerogel and the most extensively studied and used. It is a silica-based substance, derived from silica gel. The average pore diameter is $\simeq 1nm \leq d \leq 150nm$ and the porosity[8] lays between 93% and 99%. Another target tested by the AE$\bar{g}$IS collaboration is Xerogel. A Xerogel is a solid formed from a gel by drying it with unhindered shrinkage. Xerogels usually retain high porosity (25%) and

[8]Defined as the vacuum to matter volume ratio in a porous material.

enormous surface area, along with very small pore size ($1 - 10nm$). Nitrogen absorption measurements showed the presence of a bimodal distribution of pores, featuring nanopores (below $2nm$) and mesopores (between $20nm$ and $50nm$). The number density of the small pores was strongly dominant (150:1). Figure 3.18 shows the Xerogel-85 target during the 3γ mesurements made in the L-NESS laboratory. Also in Xerogel, the number 85 indicates the sample density of $85mg/cm^3$. Germanate Xerogel is a normal aerogel in which some silicon atoms are replaced by germanium. In these Aero-

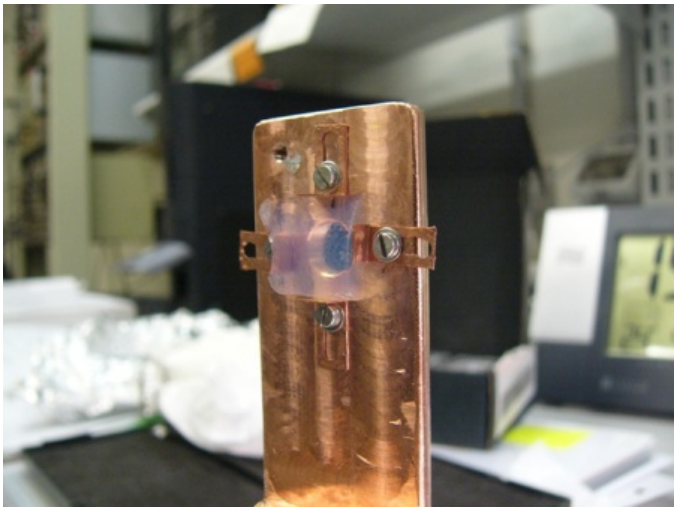

Figure 3.18: The Xerogel-85 target during the 3γ mesurements made in the L-NESS laboratory.

gel/Xerogel targets it is not possible to do PALS measurements due to their very low density (too many long lifetime components). However 3γ mesurements made in L-NESS laboraties shows that the positronium formation yield of Aerogel and Xerogel is very high, between 45% and 60%. The only one that produces "only" about 10%-20% is the Germanate Xerogel sample. Future TOF measurements are necessary in order to measure the velocity of the outgoing positronium atoms.

3.4.6 MACS

The Mesoporous Amorphous Calcium Silicate (MACS) are synthesized using mesoporous silica grains, structured by esadecilammonium hexadecyl ammonium - trimetilbenzene mixed micelles and calcined at $550C$ in air. The MACS shows a well-defined mesoporous structure with high specific surface area. The pores, with a cylindrical shape in the original material, are locally deformed by compression. Other than the structural mesoporosity, the targets show a variable macroporosity (diameter greater than $90nm$). In AE$\bar{g}$IS we test two different MACS with two different macoporosities,

named MACS-A and MACS-B. The first macroporosity has a density of $1.5cm^3/g$ and the second one has $0.5cm^3/g$. From PALS measurements made in the positron laboratory at Politecnico di Milano, we have estimated (using the Tao-Eldrup model [46]) two different mean pore size[9] in MACS-A and MACS-B, respectively $R = 6.9 \pm 1nm$ and $R = 5.5 \pm 0.7nm$. 3γ measurements made at L-NESS laboratory shows a positronium formation yield of about 35%-50% for both samples. MACS are the samples that produce more positronium after Aerogel/Xerogel. Moreover the advantage of MACS over Aerogel/Xerogel is due to the regularity of the pore and of the geometry, as they forms nanochannel, which is fundamental for the AE$\bar{g}$IS purpose.

3.4.7 Ordered nano-channels Si/SiO_2

The Trento group of the AE$\bar{g}$IS collaboration developped a novel structure with ordered nano-channels perpendicular to the surface [66]. Nano-channels have been produced by selective etching in silicon and oxidized in air at different temperatures and times. A scanning electron microscopy picture of the converter surface is shown in figure 3.19. In that sample, holes of 5-8 nm in diameter are present, and are spaced by about the same distance of 5-8 nm. The synthesis of the converter was optimized by maximizing

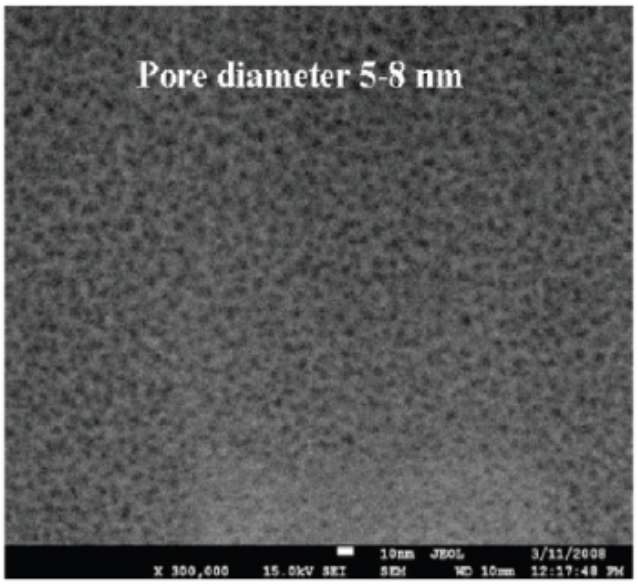

Figure 3.19: SEM picture of the Si/SiO_2 nano-channels converter surface with $5 - 8nm$ pores.

[9] With R we indicate the porous mean radius.

the positronium yield (maximum of about 50%). The high positronium yield of this system is due to the following processes. Implanted positrons thermalize in silicon and due to the high diffusion length ($200nm$ in Si), a big fraction of thermalized positrons reaches the Si/SiO_2 interface. Positrons are energetically favored to pass from silicon to the silicon oxide covering the walls of the channels. In the silicon oxide, positrons form positronium that is emitted after a very small path (few nm of silica) in the channels. This target has several advantages with respect to silica with disordered channels:

1. The diameter of the channels can be controlled. This is important if positronium at very low velocity is to be obtained. With small channel diameters (lower than 5 nm) positronium quantum confining does not allow positronium thermalization at cryogenic temperature.

2. The channels allow a very high fraction of positronium to escape into vacuum from the sample.

3. The silicon converter is expected to be less sensitive to space charge effects and damage effects under positron bombardment.

4. Positronium velocity in vacuum may be tuned by a suitable choice of the positron implantation energy and the sample temperature.

Recent time of flight measurements[10] made by Trento group show that the positronium, formed and emitted in the nano-channels, escapes from the target in vacuum [67]. The amount of emitted ortho-positronium with thermal energy is about 3% at $200K$ and 2.5% at $T = 150K$ for $7keV$ positron implantation energy (figure 3.20).

3.4.8 Conclusions

Figure 3.21 shows the positronium 3γ fraction F as a function of the positron implantation energy E for the different materials under test. At low implantation energy ($E \leq 200eV$) the 3γ fraction for all samples is high, between 20% and 60%. In MOF-177, germanate Xerogel, Vycor an increase of the 3γ fraction vs. the implantation energies was found, followed by an asymptotic decrease (figure 3.21-B). This trend, which is observed also in other materials, can be explained by a model [68] that takes into account the energy dependence of the ortho-positronium formation and escape. The model cannot be applied to silica Aerogel, where the low pick-off rate combined with a diffusion length of some microns cancels the characteristic decrease of the 3γ yield at high energy. The 3γ fraction in Aerogel samples is very high at all implantation energies, as expected for a material with very large free space between silica particles. In our quest for a promising positron-Ps converter

[10] These consist in measuring the elapsed time between the emission of positronium from the target surface and the arrival time at fixed distance of $8.9mm$.

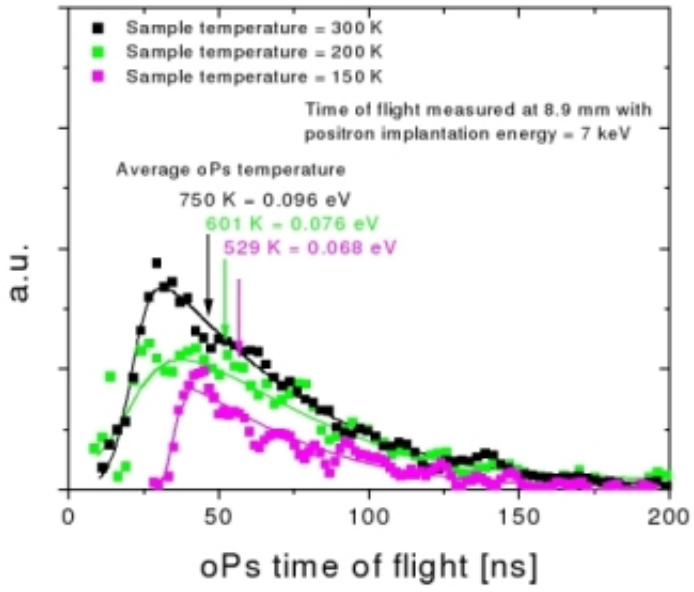

Figure 3.20: Ortho-positronium TOF measurements. The mean kinetic energy of ortho-positronium is expressed in terms of equivalent temperature $E = kT$. Present preliminary data are the only measurements with target temperature below 300 K.

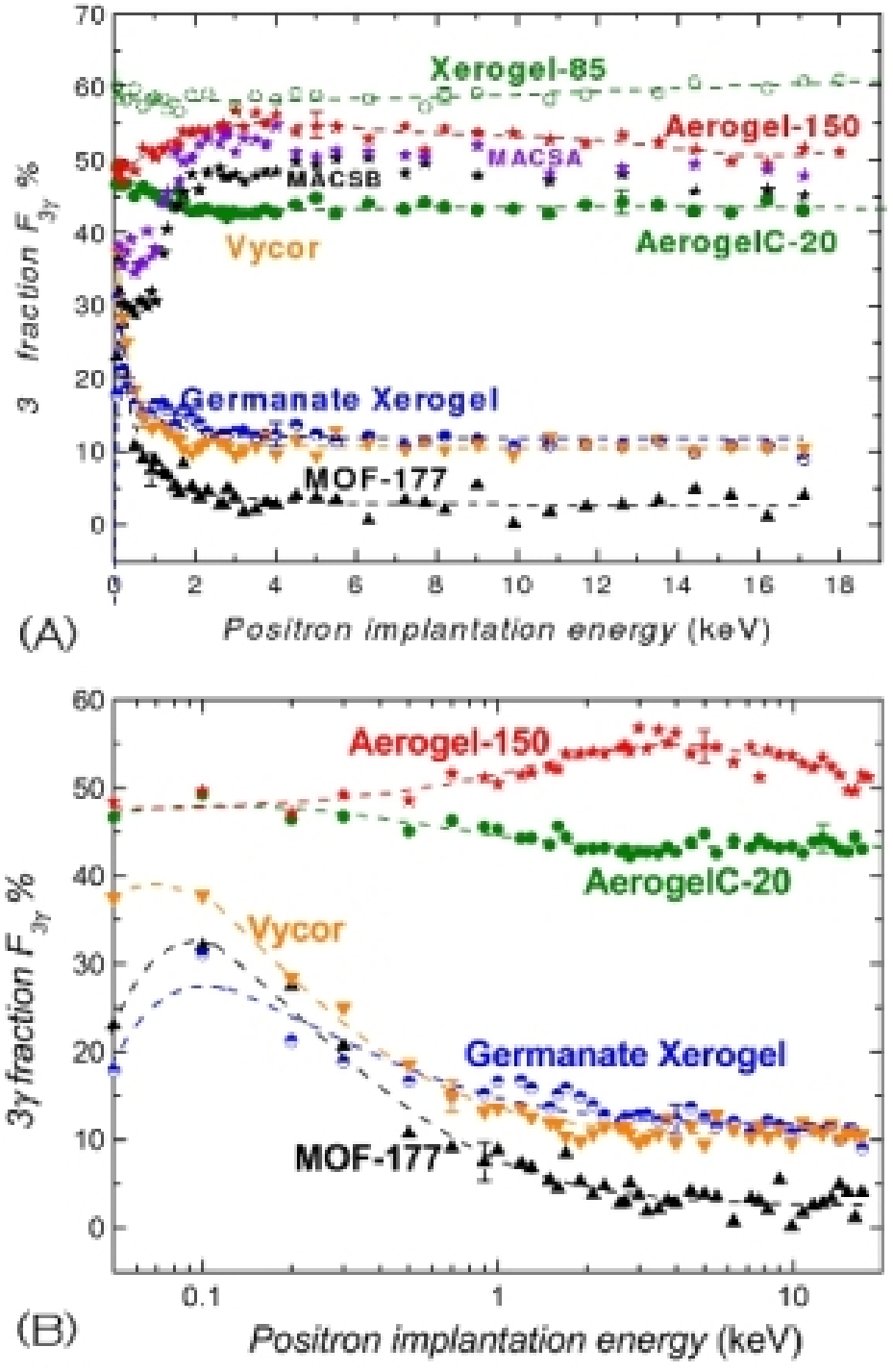

Figure 3.21: A) Positronium 3γ fraction $F_{3\gamma}$ as a function of the positron implantation energy in different porous samples: MOF-177, Vycor, germanate Xerogel, Aerogel-150, AerogelC-20, Xerogel-85, MACS. The dashed lines upper 0.1 keV in MOF-177, MACS, germanate Xerogel and Vycor are fits of the model proposed in [68]. The others dashed lines are only a visual guide. Error bars are shown for one point only in each evolution. B) The same plot in logarithmic scale for Aerogel-150, AerogelC-20, germanate Xerogel, Vycor and MOF-177.

to be chosen in the AE$\bar{g}$IS experiment, the collaboration has tested a series of materials with known open porosity. We have found that the highest formation of positronium occurs in Xerogel, Aerogel and MACS. However, high formation is not the only important factor. It must be reminded that positronium is emitted into the pores with an initial kinetic energy of the order of a few eV. Since our goal is to obtain ortho-positronium in the free space with energies of the order of $10^{-2}eV$, it is necessary that the positronium suffers a large number of collisions with the walls of the pores before emerging in the free space outside the target. This means that the useful ortho-positronium fraction must come from the deep regions of the target. This is certainly not the case of germanate Xerogel, where ortho-positronium appears to be strongly quenched in the pores. The reason is the presence in this material of a dense distribution of very small pores, probably with a low degree of interconnections, which act as dominant ortho-positronium cages. Most probably, this situation also occurs in Vycor. MOF-177 is a new material; there is no previous information of its ability in producing positronium. The experiments done in L-NESS laboratories show that, in spite of its very large free volume, this material is not really interesting as a converter. On the contrary, low-density Aerogel and Xerogel are a promising target candidate under two aspects: high formation and long survival time of ortho-positronium inside the pores. Finally MACS is the more interesting material because it has high positronium formation yield and a regular scructures of its nanopores. These nano-channels could give to positronium atoms the correct directionality request in the AE$\bar{g}$IS experiments. Another important target is the ordered nano-channeled Si/SiO_2 converter. In this case the yield is not very high but have many advantage like the possibility to make directional channels and its better electrical conduction proprieties. Additionally we have much informations about this target like TOF and "low" temperature measurements. Up to date, except for the ordered nano-channeled Si/SiO_2 converter, it was not possible to measure the kinetic energy of ortho-positronium outside the target. TOF measurements of the emitted ortho-positronium are highly desirable for finding the best compromise. At the moment all the presented targets are possible candidates.

3.5 Positronium formation in extreme conditions

In the previous sections we analysed the positronium formation and thermalization in solids without considering some important experimental condictions fixed by the AE$\bar{g}$IS apparatus:

- The first one is that the converter is located in a $1T$ magnetic field. In a magnetic field the ortho-positronium state with spin component $S_z = 0$ is mixed with the para-positronium singlet state, resulting in a reduction of the self annihilation lifetime. On the contrary the lifetime

of the orthopositronium states with $S_z = \pm 1$ are not affected by the magnetic field, therefore the maximum expected yield reduction in a magnetic field of $1T$ is one third of the ortho-positronium fraction.

- Another experimental condition is that the converter is at cryogenic temperature of about $100mK$. Theoretically, as described previously, the converter temperature should not influence the positronium production mechanism. As of today we don't have any measurement of positronium formation at so low temperature. The Trento group has shown that, in the case of ordered nano-channeled Si/SiO_2 target, we have a decrease of positronium formation yield when the temperature decreases from $300K$ to $150K$. This effect is under investigation.

- The last experimental request is the amount of positron irradiation dose on the converter. There is the possibility that the intense positron bunches can damage the porous structures and so decrease the ortho-positronium yield. In order to understand the entity of the radiation damage I designed and realized an electron beam, named eBEAM, that offers the same AE$\bar{g}$IS radiation dose (in terms of particles number and energy) but in less time with respect to a typical positron beam. The description of the apparatus will be presented in chapter 4.

Chapter 4

Electron beam for ageing measurements

In the previous chapters we have described the dependences of the positronium formation yield, its outgoing velocity, its thermalization and its directionality on the characteristics of the material that will compose the AE$\bar{g}$IS converter. These characteristics must be preserved as long as possible. The main source of damage is given by the irradiation of the converter hitting by the intense AE$\bar{g}$IS positron beam. Positrons and electrons behave in the same way for what concern energy release in solids. The only difference is due to the annihilation gammas that anyway leave the AE$\bar{g}$IS converters without depositing their energy. Since it is difficult to have a positron beam like the AE$\bar{g}$IS one, we have decided to build an electron beam that allows to obtain the same irradiation dose. Moreover, since the electronic current supplied by an electron beam is greater than the positronic one obtained by positron beam, the overall AE$\bar{g}$IS dose can be reproduced in a very short time. In this chapter we will describe the apparatus designed and built at the Politecnico of Milano (positron laboratory) to make ageing measurements of the AE$\bar{g}$IS converters with electrons.

4.1 eBEAM apparatus

The *electron beam apparatus* eBEAM, is a magnetically guided electron beam with variable energy and spot dimension. It is composed by the electron source ES-eBEAM, the magnetic guide transport line, the vacuum system, the experimental chamber and the data acquisition system as shown in figure 4.1.

The vacuum is maintained by a turbomolecular vacuum pump model Balzers TPH 180H of 180 l/s with a membrane pre-vacuum pump model Vacuubrand MD4T of 0.92 l/s. The connection between the vacuum system and the experimental chamber is located near the target as indicated

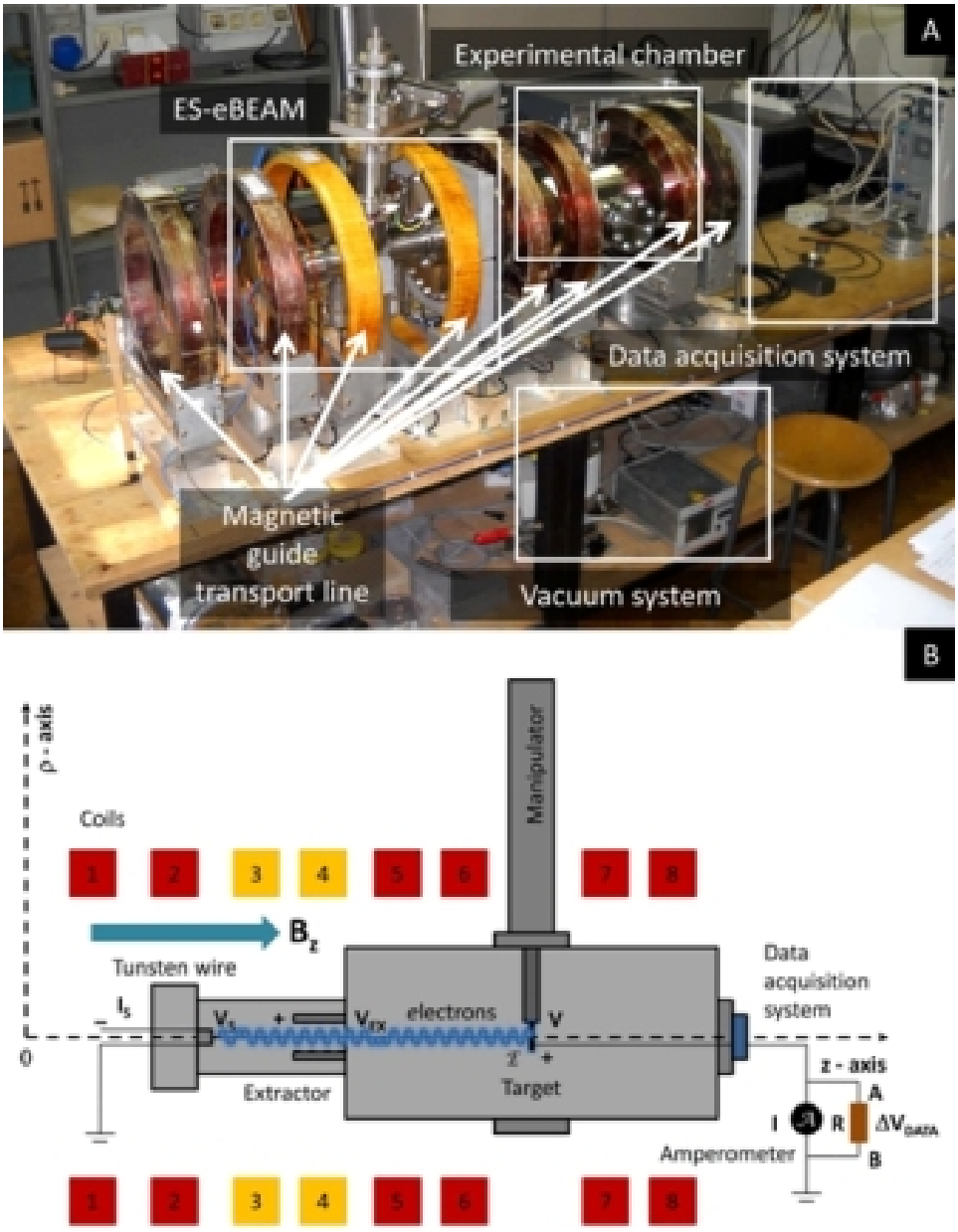

Figure 4.1: A picture (A) and the scheme from the top (B) of the *electron beam appartus* eBEAM. In (A) is not visible the manipulator.

in figure 4.1. In the present apparatus we achieved a vacuum level lower than $5.4 \cdot 10^{-7} mbar$ after two days of pumping. The vacuum connections make use of 17 gaskets and 2 O-rings. The vacuum is measured by a Penning vacuumeter (model Balzers IKR 020), decoupled from the beam pipe by a valve (model VAT series 10.8). The eBEAM source ES-eBEAM, is constituted by an heated Tungsten wire as described in section 4.2.2 (the nominal maximum power is $50W$). In front of the electron source an $1050V$ extractor is mounted. This extractor considerably increases the efficiency in the electron collection process given that it direct the electron near the source to the target. A system of 8 coils produces an axial uniform magnetic field B_z of about $100G$. The shape of B_z versus the z axis position is shown in figure 4.13. More informations about the eBEAM's magnetic field can be found in section 4.3. The experimental chamber contains the sample which support is described in section 4.4. The target is held to a potential V (produced by generator model FUG HCN 7E-35 000) that fixes the electron energy at the sample. The electronic current, measured by an Agilent U1241A amperometer is constant when varying the target potential V as shown in figure 4.2.

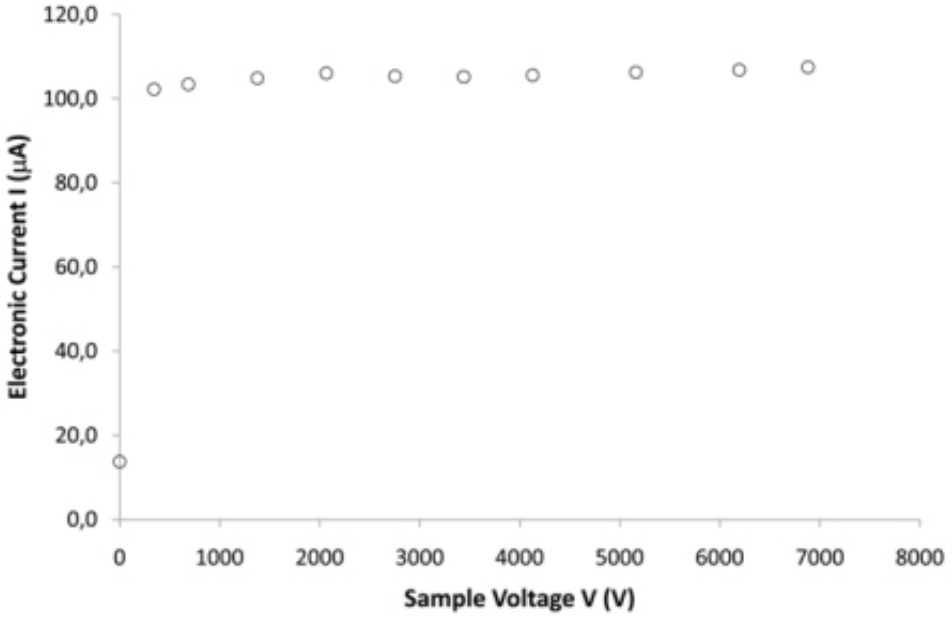

Figure 4.2: The electronic current I vs the electron energy (i.e. the sample's voltage V). Measurements done without extractor; the power of the Tungsten wire is fixed at about $40W$ and the magnetic field is on.

Instead, the electronic current increase when the Tungsten wire is heated, i.e. when changing the wire potential V_S (current) as shown in figure 4.3.

By a linear fit we obtain the relation between the wire potential and the

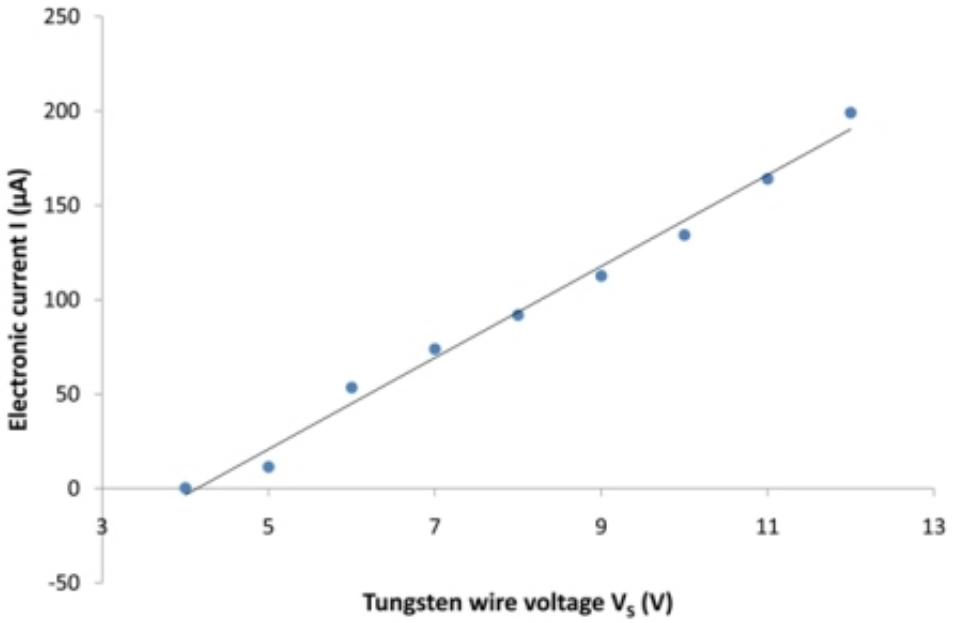

Figure 4.3: The electronic current I vs the wire potential V_S for $3.5keV$ electrons. The blue dots are the experimental data and the black line is the linear fit.

electronic current at the target, given by ($I \geq 0$):

$$I(V_S) = 24.22 \left[\frac{\mu A}{V}\right] V_S - 100.2 \, [\mu A] \, . \tag{4.1}$$

It is thus possible to tune independently the number of electrons and their energy in order to increase or decrease the irradiation dose. The current used experimentally varies between $0.1\mu A$ a $200.0\mu A$[1]. The target voltage can vary between $35V$ and $10000V$ corresponding to a kinetic electron energy range between $35eV$ and $10keV$. At this energy we usually have X rays production in the sample as simulated, for example, by the CASINO software. This X rays are anyway absorbed by the apparatus as confirmed by Geant4 simulations. We have simulated the overall eBEAM apparatus with SIMION 8.0 framework.

The simulation gives, for a $32W$ electron source ($V_S = 10V$), a transport efficiency of about 58 % (the losses are mainly due to the electrons emitted backwards) with a simulated current of about $144\mu A$. This is in agreement with the experimental value of $142\mu A$ obtained by the equation 4.1 for $V_S = 10V$ wire potential.

[1]The minimum measured electronic current is fixed by the amperometer's resolution that is $0.1\mu A$. The maximum value is instead limited by the sample voltage generator that accept as maximum input voltage $200\mu A$.

4.2 The electron source

The usual way to produce electrons is by means of an electronic gun. In order to understand the operation of this machine and to improve its performance, we designed and built two electronic guns. The first one, conceived as a test source (Test Electron Source, TES-eBEAM), was designed for a low vacuum system and an operational time of only few minutes. The second one is instead the final eBEAM electron source (Electron Source, ES-eBEAM). In the following sections we will present the design and the experimental tests of the two electron sources.

4.2.1 TES-eBEAM

The TES-eBEAM design and a picture of the apparatus at the Politecnico di Milano positron laboratory are shown in figure 4.4.

The electronic scheme of the electron source is depicted in figure 4.4 and is quite simple. A tungsten wire is heated by Joule effect to a temperature of $1000 - 2000K$. This is achieved by the current generator G_1 that produces a DC current I_S between 0 and $4A$. The positive pole is connected at ground. Thus, the wire is repulsive from the electrons point of view. They are so driven to the positive charged electrode $\mathcal{E}$. This electrode is powered by the high voltage generator G_2 that produces a positive potential V, attractive for the emitted electrons. The distance between the wire and the electrode is about $200mm$. This small distance does not require the presence of an extractor electrode in front of the wire in order to reduce electron losses.The electronic current generated by the electrons emitted by the source is measured by an analogic amperometer $\mathcal{A}$ with resolution of $0.5\mu A$. The electron energy spectrum of the source depends on:

- the negative potential between the wire and ground V_S,
- the positive potential on the target V,
- the kinetic energy of the electrons when they are thermoionically emitted by the wire (temperature dependent).

In order to understand the shape of the electron energy spectrum, we developed a Monte Carlo simulation of electron emission from Tungsten wire [69]. The details are reported in appendix A where we also report the analytical

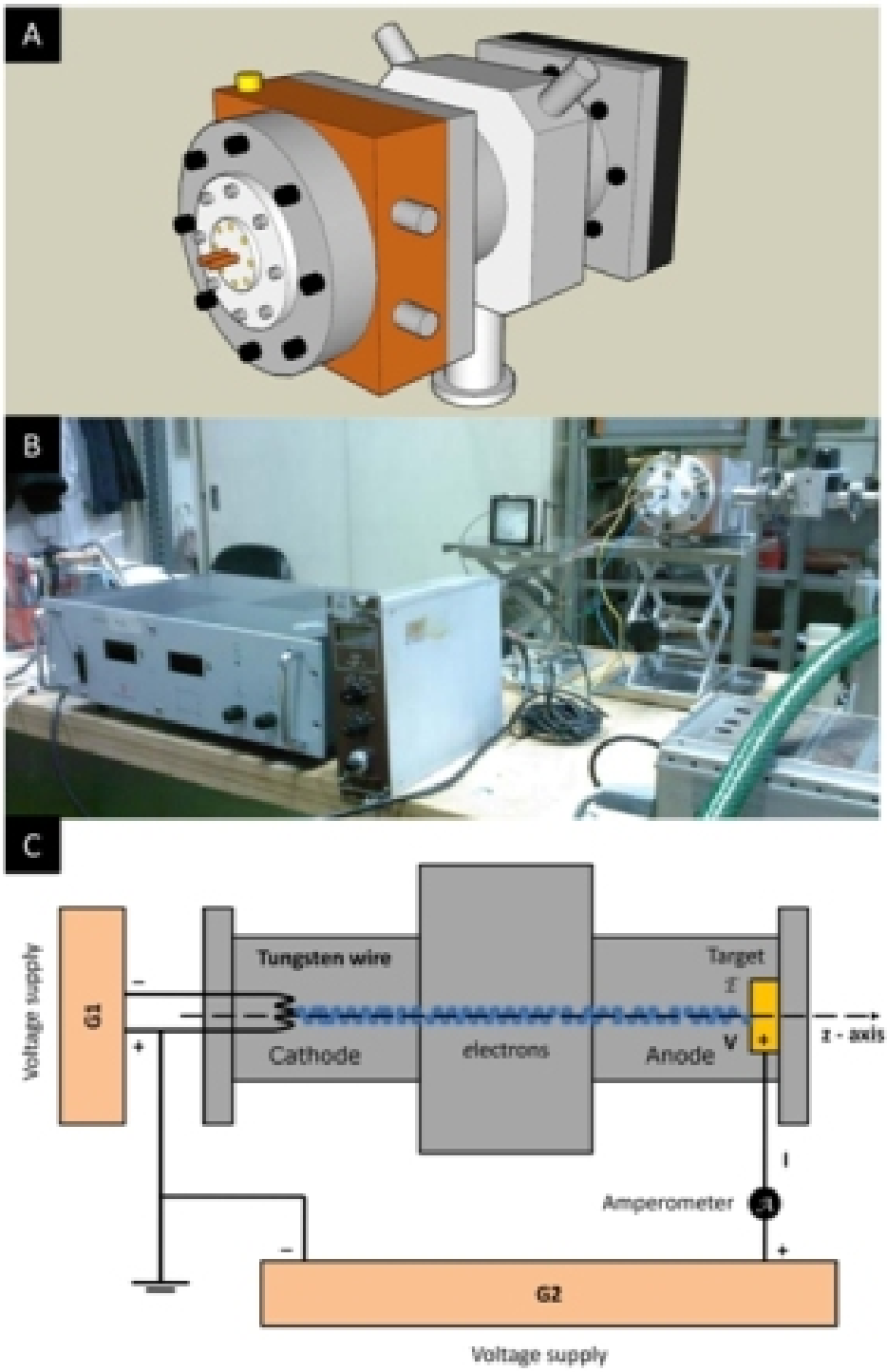

Figure 4.4: The TES-eBEAM apparatus. (A) the design (B) the elecron source during the experimental tests (C) the electronic scheme.

calculation of the energy electron spectrum $h(E)$ given, at the source, by:

$$\begin{aligned} h\left(E_{TOT}\right) &= \left[\frac{2e^{-(E-U_S)}\sqrt{(E-U)\,\beta}}{2\beta^{\frac{3}{2}}}\right]\Theta\left(E-U_S\right)+ \\ &- \left[\frac{\sqrt{\pi}Erf\left(\sqrt{(E-U)\,\beta}\right)}{2\beta^{\frac{3}{2}}}\right]\Theta\left(E-U_S\right)+ \\ &- \left[\frac{e^{-E\beta}\sqrt{E}}{\beta}\right]\Theta\left(E\right)+ \\ &+ \left[\frac{\sqrt{\pi}Erf\left(\sqrt{\beta E}\right)}{2\beta^{\frac{3}{2}}}\right]\Theta\left(E\right) \end{aligned} \tag{4.2}$$

where E is the electron kinetic energy, $\beta = (k_B T)^{-1}$, T is the wire temperature, k_B is the Boltzmann constant and if we call V_S the negative potential of the wire, $U_s = eV_S$ is its associated potential energy. In order to obtain the energy electron spectrum at the electrode $\mathcal{E}$ we must do the substitution E with $E+U$, where U is the potential energy $U = eV$. Figure 4.5 shows the electron energy spectrum for $T = 2000K$, $U_s = 12eV$ e $U = 100eV$.

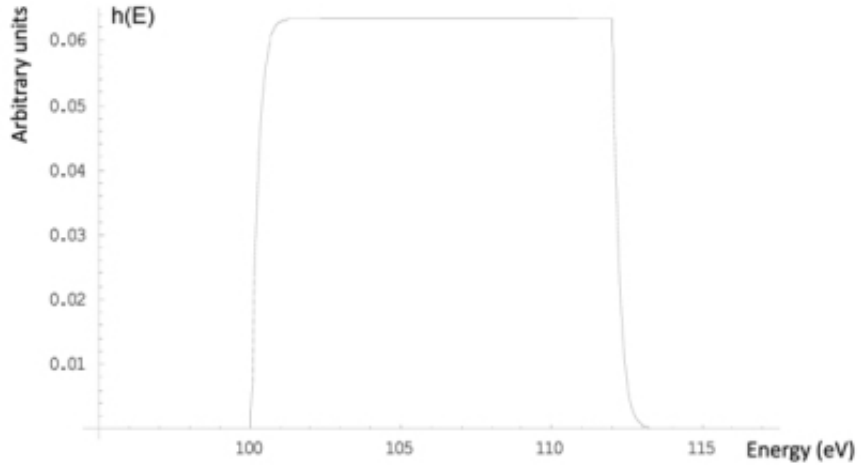

Figure 4.5: The electron energy spectrum for $T = 2000K$, $U_s = 12eV$ e $U = 100eV$.

Now, if $U \gg U_s$ then the energy electron spectrum is a delta distribution in $E = U$. Given that generally in eBEAM $U \geq 500eV$ and $U_s \leq 12eV$ the previously condition is satisfied so that we will approximate the electron energy to U. The number of electrons that reach the electrode $\mathcal{E}$, and so the

electronic current, depends instead on the electrostatic field generated and in particular, in our case, by the voltage V at the electrode $\mathcal{E}$. The simple configuration of the TES-eBEAM allows to consider it like a thermionic diode. In particular we can predict the electronic current I dependence from the voltage V applied between the cathode (tungsten wire) and the anode (the electrode $\mathcal{E}$). The theoretical plot of I versus V is shown in figure 4.6.

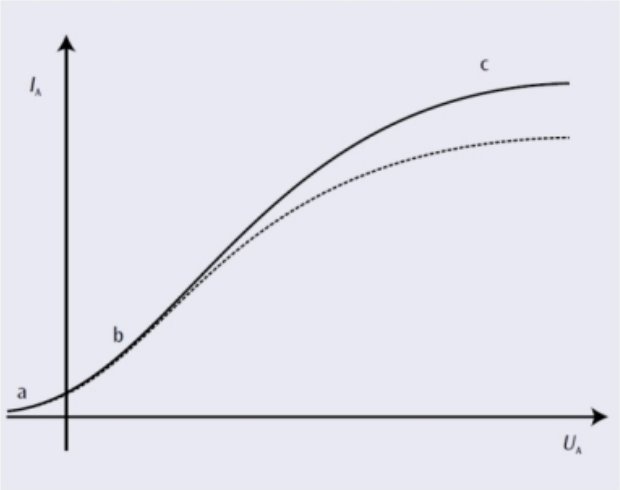

Figure 4.6: Characteristic of a thermionic diode: (a) the reverse bias region, (b) the space charge region and (c) the saturated region.

We can identify three regions: the reverse bias region, the space-charge region and the saturated region.

1. Reverse bias region (a): since electrons are emitted from the cathode (wire) with a kinetic energy $K > 0$ the current flows in the anode (target) only until the voltage of the anode is sufficiently negative that even the fastest of the emitted electrons is unable to overcome the field to reach the anode.

2. Space charge region (b): for weak field strengths, not all the electrons emitted from the cathode are transported to the anode. They occupy the space around the cathode in a cloud creating a negative space charge. When the voltage is low, field lines for the anode thus reach only as far as the electrons in the cloud and not the cathode itself. The latter is thus shielded from the anode field. Only when the voltage increases can the field lines penetrate further into the cathode causing the anode current to rise. The increase continues until the space charge

around the cathode is dissipated, at which point the anode current is saturated.

3. Saturated region (c): in the saturation region the anode current does not depend on the anode voltage at all. It can nevertheless be increased by increasing the number of electrons emitted from the cathode in unit time. This can be achieved only by raising the temperature of the cathode. The saturation current therefore depends on the source voltage.

Experimentally we measured the electronic current at the electrode $\mathcal{E}$ versus the sample potential V. The sample is a disk (radius $15mm$) of brass located at $200mm$ from the source. The experimental data compared with the SIMION 8.0 simulations are shown in figure 4.7.

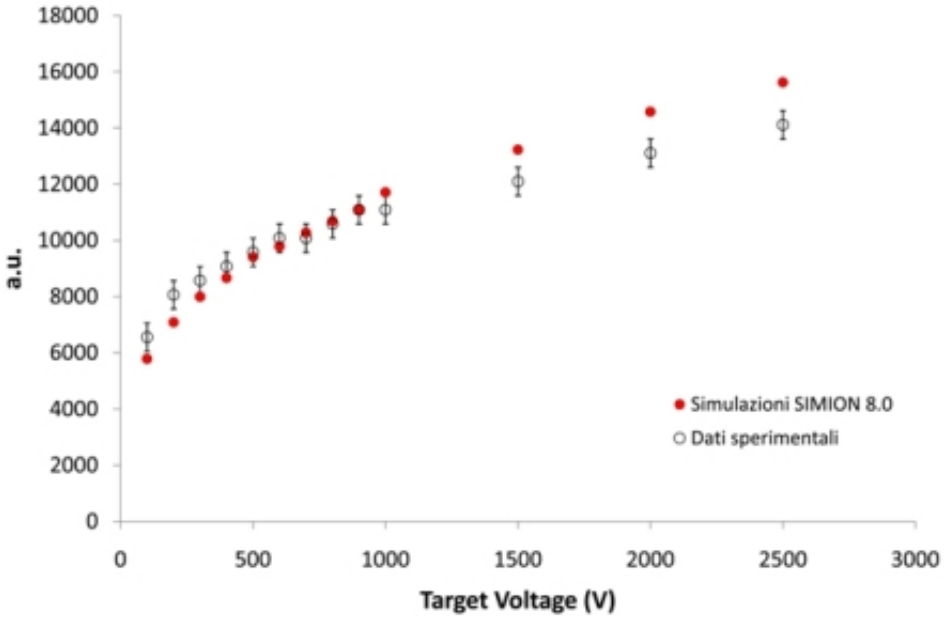

Figure 4.7: The electronic current dependence from the potential at the electrode $\mathcal{E}$. Black circles are the experimental data and the red points the SIMION 8.0 simulations.

We can distinguish the space charge (for energy lower than $500eV$) and the beginning of the saturated regions. The simulation is only approximate given that are considered the electron source point-like and mono-energetic. In our test measurements we used $V_S = 11.5V$, $I_S = 3.6A$ (so that the dissipated power is $41.4W$), and V was changing from $100V$ to $2500V$. The pressure of the chamber was $3.5 \cdot 10^{-5} mbar$, maintained by a rotative pre-pump model Balzers DUO 1,5 A of 0.0361 l/s with a turbomolecular model Balzers TPH 062 of 56 l/s pump. All vacuum connections are made by O-

Ring (OR). The tungsten wire is surrounded by a semi-cylinder in glass due to the original "lamp" wrapping. In fact this one is obtained by cutting a commercial car lamp. This low vacuum can decrease the electronic current at the anode. These phenomena are not considered in our simulations. The maximum electronic current achieved with the TES-eBEAM is $14.0 \pm 0.5 \mu A$ with $V = 2500V$. The TES-eBEAM has been designed with a water cooling system, but it has never been used. Without cooling, the TES-eBEAM can safely work till about ten minutes. This is due to the presence of O-rings around the wire connections. When the O-rings are working for a few minutes there is the possibility that the O-rings could be warped with the consequence gas inlet in the apparatus. This gas can oxide the tungsten and thus destroy the wire.

4.2.2 ES-eBEAM

After the design and realization of the TES-eBEAM, we developed an upgraded electron source named ES-eBEAM (see figure 4.8).

The first important difference between the two models is the use of copper gaskets instead of OR for the vacuum connections. These guarantee a vacuum value lower than $5.4 \cdot 10^{-7} mbar$ when the ES-eBEAM is connected to the beam pipe. The pumps (a membrane pre-pump with the previous turbomulecular pump) are not connected directly to the ES-eBEAM, but at the beam pipe. The second difference is the possibility to have two high voltage input in the electron source region (by BNC-MHV connectors that support $5000V$ as maximum voltage. These substitute the original $1000V$ ceramic connectors mounted on ES-eBEAM during the first tests.). One of them (indicated with the letter B in figure 4.8B [2]) is used as extractor voltage supply. The extractor is an hollow cylinder in Aluminium (figure 4.8), with inner radius $R_i = 5mm$, outer radius $R_o = 12mm$ and length $L = 40mm$. The central hole is used like a beam collimator and it is possible to mount in front of it a Molybdenum diaphragm or a grid in order to reduce the electronic current at the sample (e.g. for few particles experiments). The extractor is connected to the voltage supply that gives a potential of V_{ex} with respect ground. The electronic current on the target as a function of V_{ex} is shown in figure 4.9.

ES-eBEAM is also connected to a vacuumeter through a valve VAT series 10.8. This valve decouples the vacuumeter from eBEAM when the required vacuum level is achieved. In fact the vacuumeter is a Penning probe with a permanent magnet inside which generates a magnetic field that is negligible in the usual eBEAM magnetic field regime but can become significant when we want to use the electron beam for few particle experiments. For $7keV$ electrons, the differences in the electron current are however negligible. The

[2] This scheme is a zoom of the source area shown in figure 4.1

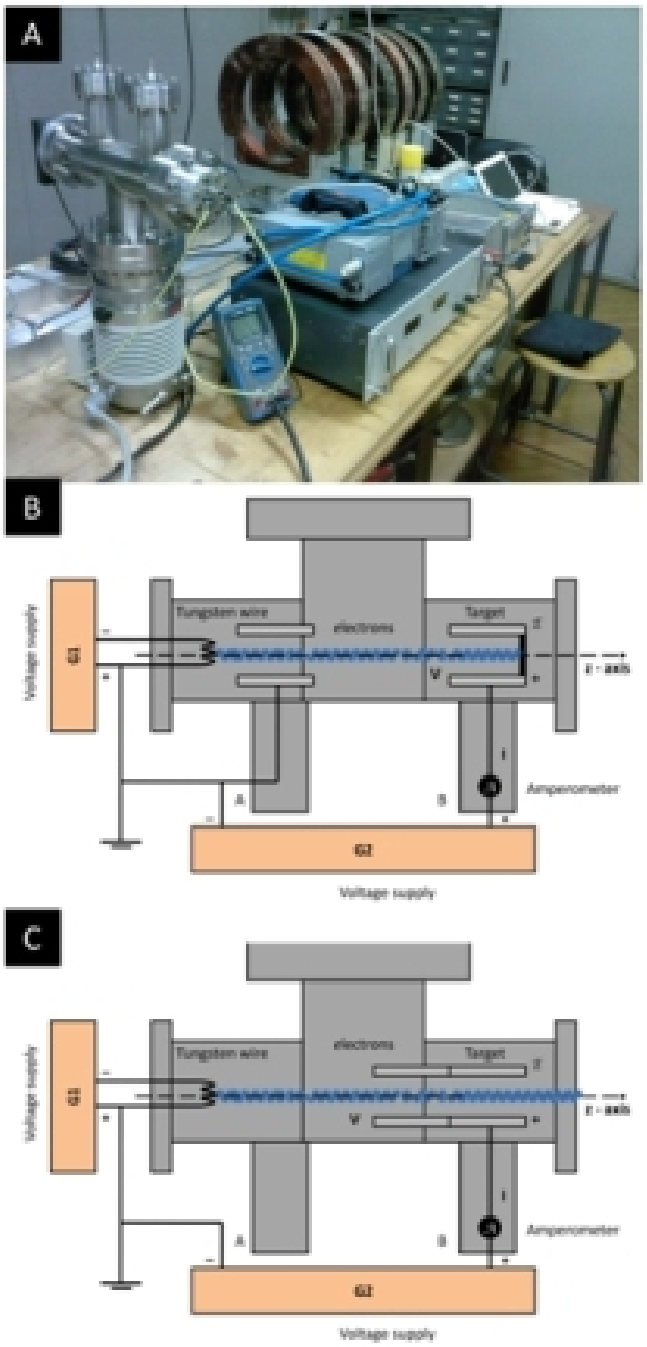

Figure 4.8: (A)The ES-eBeam electronic source during the preliminary tests in the Politecnico positron laboratory (the source is upside down compared to the scheme B and C). (B) The ES-eBeam in the two extractor configuration. (C) The ES-eBeam in the one extractor configuration. The ES-eBeam operates in absence of magnetic fields.

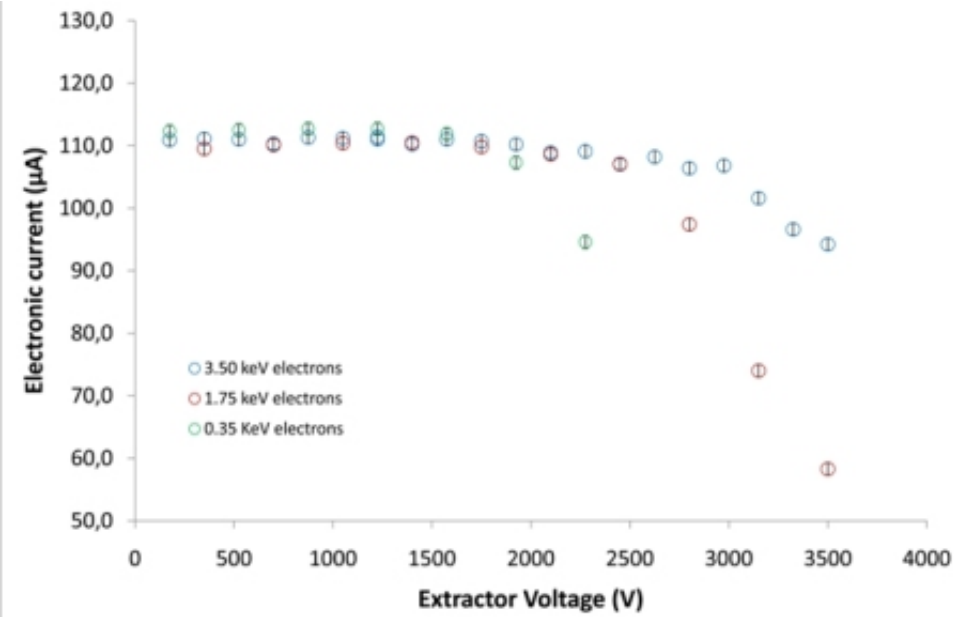

Figure 4.9: The electronic current at the sample I versus the extractor's voltage V_{ex} for 350, 1750 and 3500 eV electrons ($V = 350, 1750 and 3500 V$.

last advantage of ES-eBEAM respect to TES-eBEAM is the UHV connection of the wire electrodes. These are surrounded by glass so that it is possible use the electron source for a long operational time. In order to increase the operation time we added an air cooling system; this garantie the use of the electron source continuously at the maximum power. In figure 4.10 we report the electronic current I versus the sample voltage V (sample is a foil of Molibdenum at a $262mm$ from the source) in absence of any external magnetic field and with two extractor at ground in the position illustrated in figure 4.8(B) (each extractor has $R_i = 5mm$, $R_o = 12mm$ and $L = 20mm$). The experimental data are compared to TES-eBEAM measurements.

As seen previously, in absence of a external magnetic field, the electron source can be described by the thermionic diode theory. The electronic current, in the experimental conditions described previously, saturates at a value of about $43.3\mu A$ (wire at $32W$). This electronic current, greater than the one achieved by the TES-eBEAM electron source, is only the 17.4% of the maximum number of electron per second emitted by the heated tungsten wire. This percentage was computed by SIMION 8.0, in the assumption that we don't have irradiation or space charge effects (see figure 4.11).From this first simple simulation we obtain that at $32W$ the emission current I_e is $0.248mA$. Thanks to this information we can deduce the temperature of the

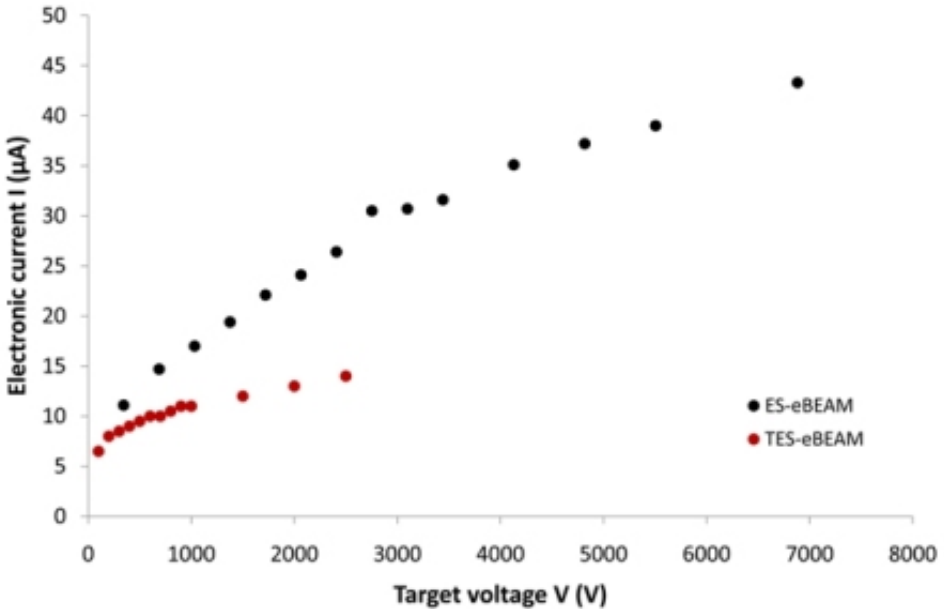

Figure 4.10: The electronic current versus the sample voltage V (sample is a foil of Molibdenum at a $262mm$ from the source) in absence of any external magnetic field. The experimental data are compared to TES-eBEAM measurements.

tungsten wire. In fact the Richardson's law for the thermionic emission is:

$$I_e = AST^2 e^{-\frac{W}{k_B T}} \tag{4.3}$$

where $A = 1.2 \cdot 10^{-6} A/m^2 K^2$ is the Richardson's constant, $S \cong 80mm^2$ is the wire surface, T is the temperature of the wire, $W = 4.5eV$ is the work function for the Tungsten, and k_B is the Boltzmann's constant. Now, if we substitute the numerical values, we obtain:

$$I_e(A) = 96AT^2 e^{-\frac{52220K}{T}} \tag{4.4}$$

By numerical integration of this equation for $I_e = 2.48 \cdot 10^{-4} A$ we get $T = 1869K$. In future it will be possible to compare this theoretical value with the temperature measured for example with a pyrometer.

4.3 The magnetic guide field

The electrons emitted by the heated wire in the ES-eBEAM source are magnetically guided to the sample support. In order to generate the appropriate magnetic field we used a set of pre-existing coils (figure 4.1).

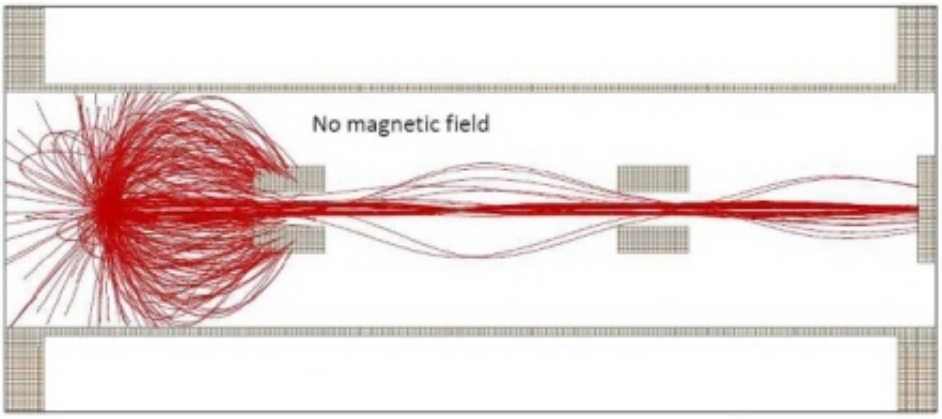

Figure 4.11: The SIMION 8.0 simulation of ES-eBEAM. The absence of the magnetic field increase the beam divergence (with electron losses).

These coils allow access to the beam pipe for pumps or electrode entries as well as for the sample manipulator. The disadvantage is the non uniformity of axial magnetic field in the zone between two different coils. In order to understand this effect we compute the magnetic field in space generated by $\mathcal{N}$ coils by the MI-AEGIS.Mag software as described in appendix B. In principle the free parameters are the distance between the coils and their currents. Given that we have a great number of coils the computational time would be too long. Thus we decided to fix the coils distance (bound to the apparatus configuration) and vary the coil currents in order to obtain the best uniform axial magnetic field B_z in a cylinder of about tens millimeters in diameter along the eBEAM axis z. In table 4.1 we summarize the current-position final configuration.

Coil number	R_i **-** R_o	z_c	**Coil current**
1	$140mm - 190mm$	$65mm$	$13.20A$
2	$140mm - 190mm$	$235mm$	$5.70A$
3	$190mm - 210mm$	$355mm$	$23.30A$
4	$190mm - 210mm$	$545mm$	$23.30A$
5	$140mm - 190mm$	$715mm$	$6.90A$
6	$140mm - 190mm$	$835mm$	$6.90A$
7	$140mm - 190mm$	$1105mm$	$21A$
8	$140mm - 190mm$	$1225mm$	$21A$

Table 4.1: The current-position (z_c) final configuration. R_i is the inner coil radius and R_o the outer one. The thickness $L = 54mm$ is equal for all coils.

The radial magnetic field $B_\rho(\rho, z)$ vanishes on the z axis. Given that

we want to compute the magnetic field components $B_z(z,\rho)$ and $B_\rho(\rho,z)$ also outside the z axis where $B_\rho(\rho,z) \neq 0$, we cannot compute them in the analytical way but only numerically by the MI-AEGIS.Mag software, as described in appendix B.1.2. The eBEAM total magnetic field $|\vec{B}(\rho,z)|$ and its components $B_z(\rho,z)$ and $B_\rho(\rho,z)$ are shown in figure 4.12.

The magnetic field map was implemented in SIMION 8.0 by SL-Toolkit as described in appendix B.1.4.The comparison with the experimental data are shown in figure 4.13 for $\rho = 0mm$ (on the beam axis) and $\rho = 220mm$ (outside the coils). This, combined with the electic field computed by SIMION 8.0, provides the simulation of the electron trajectories. Moreover, given the good comparison with experimental data, it is possible to calculate the magnetic field inside the beam having a measure of the field outside the coil system as a check.

Given that in the coils 7 and 8 a maximal current of $21A$ circulates, we provided an air cooling system with fans that blow cold air directly on the coils surface. This cooling system is not very efficient and given that we want to use eBEAM for a long time, we measured the temperature of the coil number 7 versus the operational time in standard conditions. The experimental data are reported in figure 4.14.

We fit the curve with a saturation function $T(t) = T_0\left(1 - Ae^{-\frac{t}{\tau}}\right)$ where A is a constant, τ is the characteristic time and T_0 the asymptotic temperature. From the fit we obtain $T_0 = (39.46 \pm 0.27)°C$ which guarantees the safety of the coils for long operational times.

4.4 The sample support

eBEAM was designed to make ageing measurement for the AE$\bar{g}$IS antimatter experiment. In AE$\bar{g}$IS the positron to positronium converter must be a solid. For this reason, we developed a sample support for solid targets to be located at the end of the apparatus(figure 4.15).

The sample support is a metal frame electrically isolated from the manipulator (at ground) by a Polyether ether ketone (PEEK) GF30 cylinder. The frame can hold a sample for normal irradiation and can be used for transmission measurements (for example the beam spot determination by a phosphor screen). The manipulator has one degree of freedom i.e. the transverse motion. Thus, it is possible to irradiate the sample by adjusting its position on the electron beam axis.

4.5 Acquisition system

At the moment the measurements that can be done with the eBEAM apparatus are the electronic current and the beam spot dimension. The first one is directly measured by an high precision amperometer (Agilent U1241A),

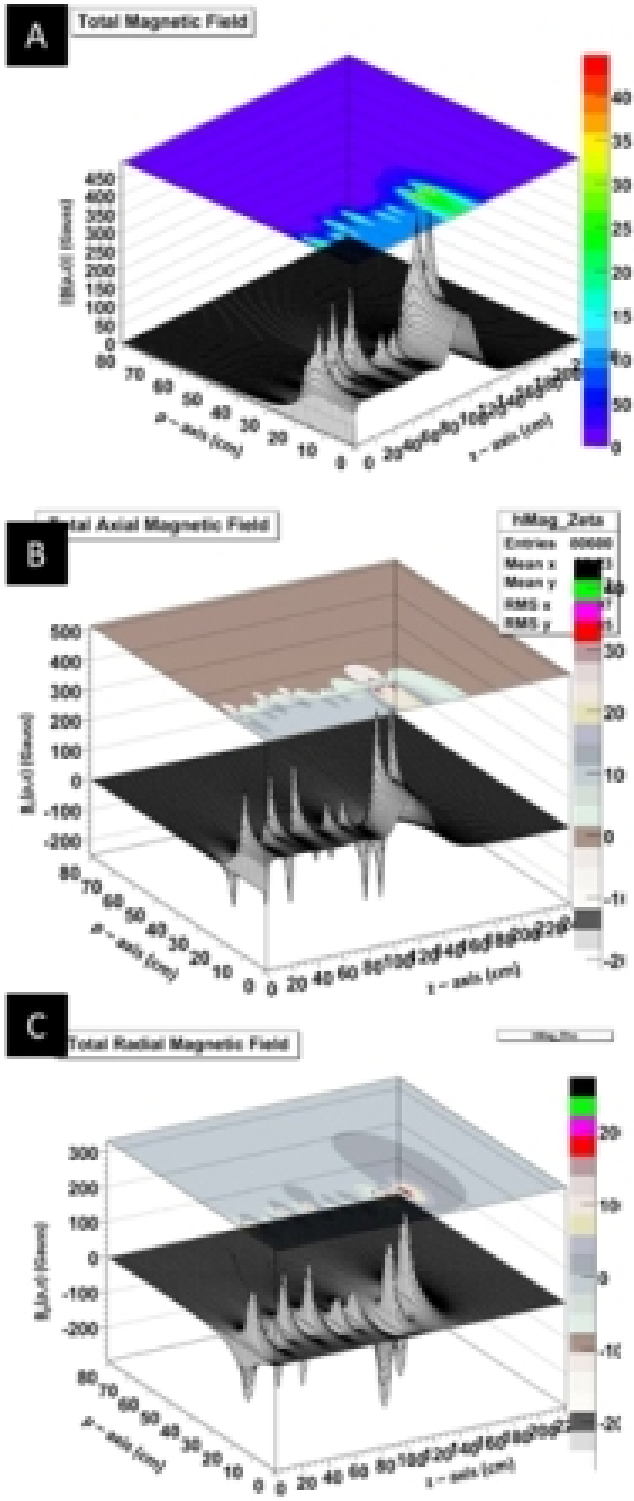

Figure 4.12: The eBEAM magnetic field computed by MI-AEGIS.Mag software. (A) is the total magnetic field $|\vec{B}(\rho, z)|$ (B) the axial component $B_z(\rho, z)$ and (C) the radial one $B_\rho(\rho, z)$. The plots show as the axial magnetic field on the beam axis is uniform and increase only near the target ($z = 1m$) in order to focus the particles.

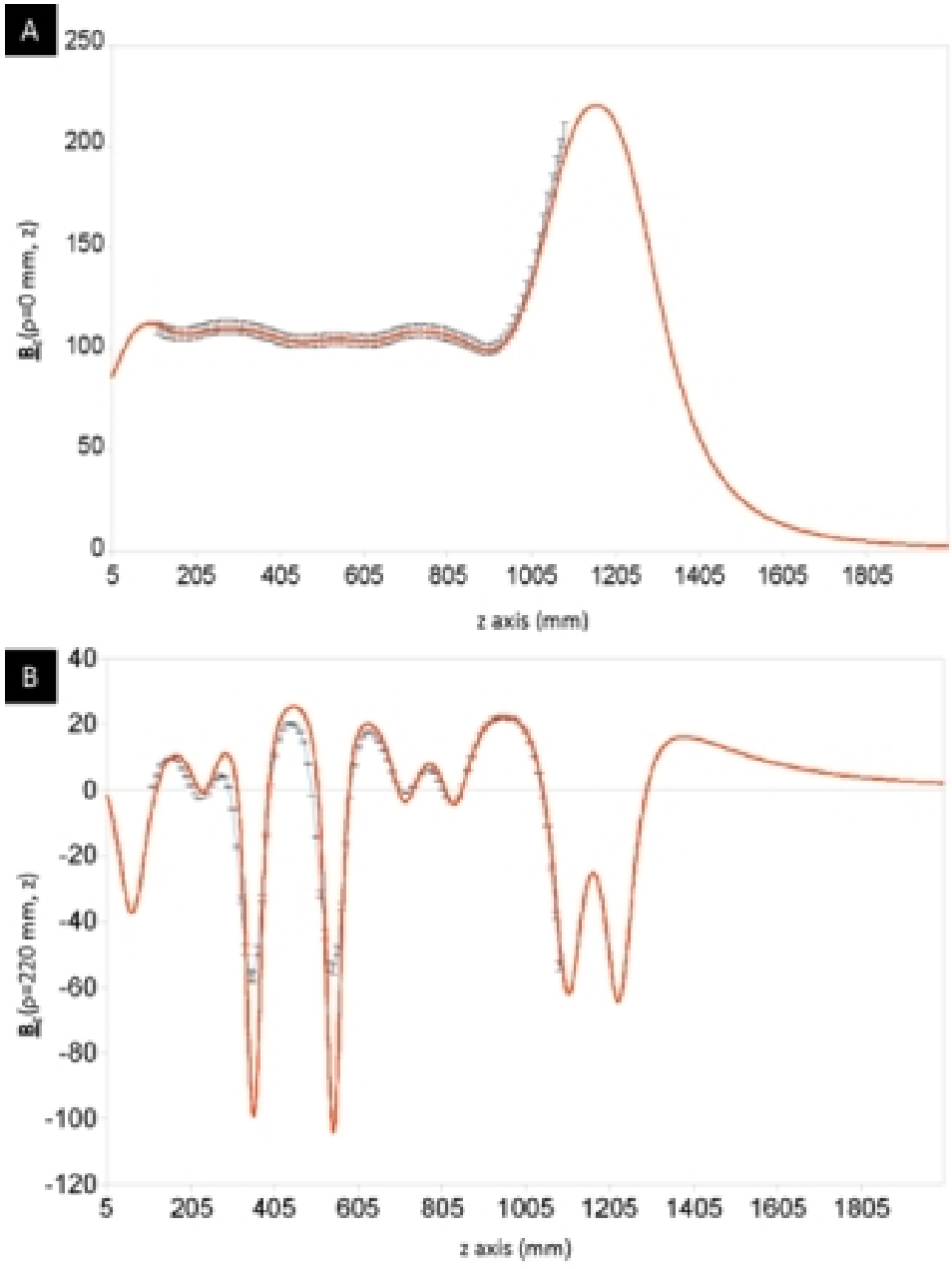

Figure 4.13: The eBEAM magnetic field measured at $\rho = 0mm$ and $\rho = 220mm$. The black dots are the experimental points and the red line is the theoretical curve computed by MI-AEGIS.Mag software

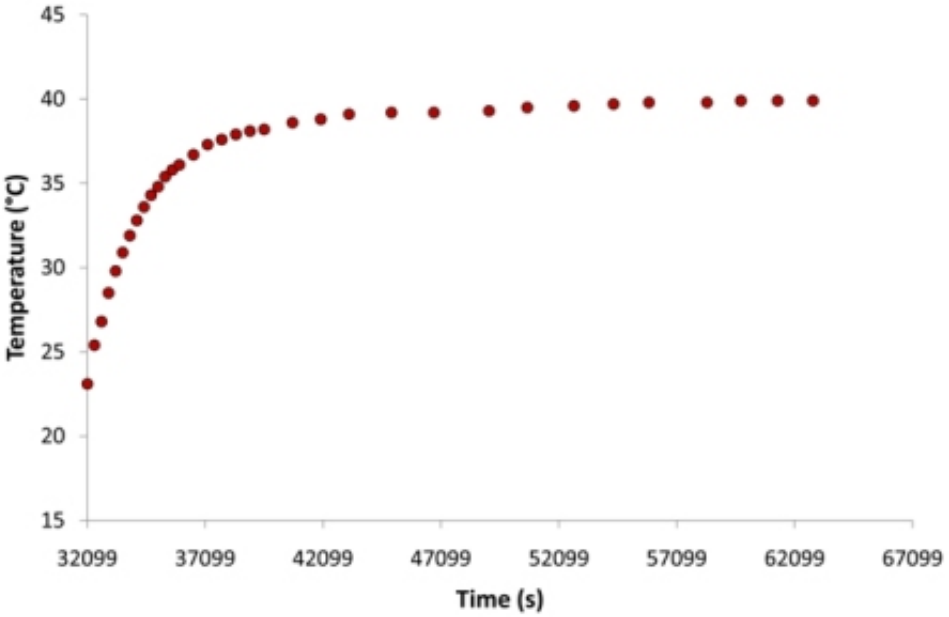

Figure 4.14: The coil number 7's temperature versus the operation time in standard conditions.

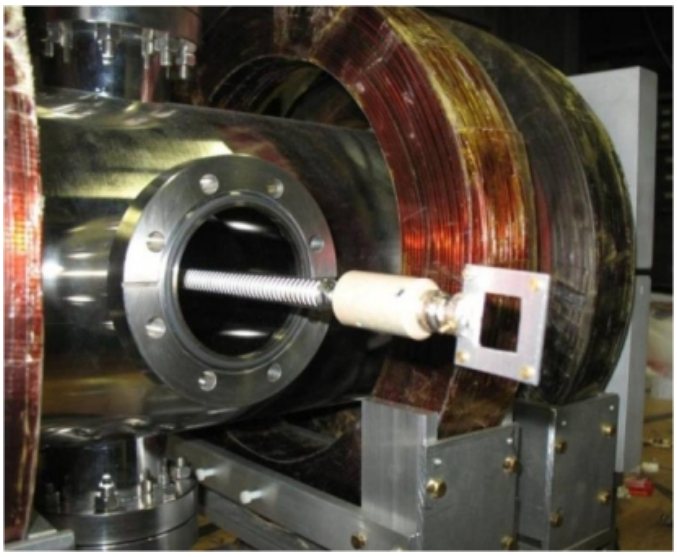

Figure 4.15: The first prototype of target support between the coils number 6 and 7.

indicated in figure 4.1 by $\mathcal{A}$. If we insert a resistor R between A and B (figure 4.1) we can measure the electronic current I by the difference of potential ΔV_{data} across it: $I = \frac{\Delta V_{data}}{R}$. This voltage can be digitized by an ADC converter like the ADC0831 model and recorded by a QBASIC software developed on purpose. The voltage ΔV_{data} can be set to a few volts by changing the resistance R. The only problem is that ΔV_{data} is referred to V and not to ground. Thus we need a photoisolator like the Fiber Optic IsolatorPhotologic Sensor OPI1290 Series model. The eBEAM acquisition system is based on webcams. A webcam, controlled by the Dorgem software, acquires a picture of the electronic current every fixed Δt between $1s$ to $99s$. After the measurement, this electronic current values must be manually transcribed into an ASCII file. Another webcam, commanded by the K3CCD Tools software, allows to control if the target support is aligned with the electron beam. This is calibrated by the phosphor screen beam spot. A picture taken by this webcam is shown in figure 4.16.

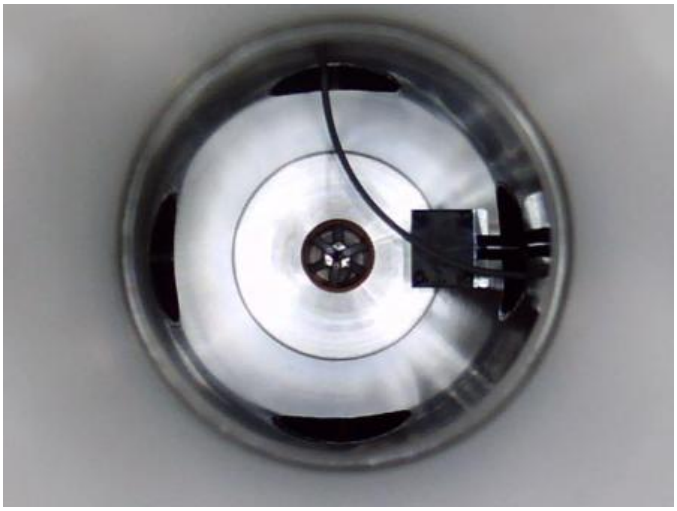

Figure 4.16: A picture of the sample taken by the control camera. In the center there is the extractor and to the right the target support. The upper entrance is the access to high voltage supply. The lower entry is the access to the vacuum turbomolecular pump.

The beam spot was obtained by the use of a phosphor screen mounted on the new kind of sample support. A picture of the screen, taken by a Canon Powershot 640 and analysed by the MI-AEGIS.Pic Matlab/C++ software developed on purpose, is shown in figure 4.17.

The experimental beam radius R is found to be $(2.175 \pm 0.275)mm$. The ring-like shape of the spot showed in figure 4.17 could be explained as the image of the tungsten wire on the target. In fact, the filament is a cylinder placed along the z - axis. We are thinking about the possibility to

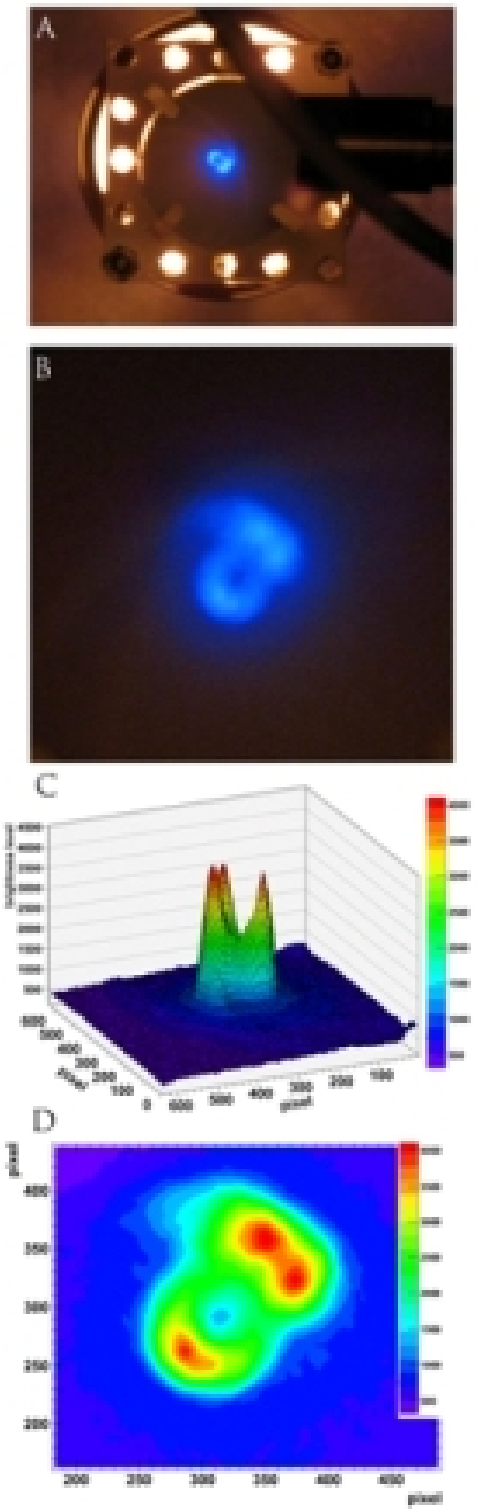

Figure 4.17: (A-B) The beam spot as seen on the phosphor screen. (C-D) The 3D-2D brightness level histogram as obtained by the MI-AEGIS.Pic software.

make an antenna measurements of the beam spot radius R versus the axial coordinate z. In fact, an electron in cyclotron motion emits radiation with discrete frequencies. The more intense of them is the cyclotron frequency (first harmonic) $\omega_c = \frac{eB}{m_e}$. Given that $R = \sqrt{\frac{2K}{m_e \omega_c^2}}$ and that the axial magnetic field B_z is not uniform, but weakly depends on the axial coordinate z, it is possible to determine the function $R(z) = \sqrt{\frac{2K}{m_e \omega_c^2(z)}}$ by measuring the radiation frequency $\omega_c(z)$. Given that R is a function of B_z it is also possible to measure the axial magnetic field $B_z(z) = \frac{m_e \omega_c(z)}{e}$. This indirect measure should be in agreement with the direct ones described in appendix B.

4.6 Ageing measurements

At the present status, we have built and characterized the electron beam eBEAM. Given that electrons and positrons release the same amount of energy in solids, eBEAM can be used for ageing measurements of the AE$\bar{g}$IS converter. In the near future, for each converter, we will able to measure the positronium formation yield before and after irradiation by eBEAM. The converter radiation dose must be the same of which achieved in the AE$\bar{g}$IS apparatus at CERN. Any change in the positronium formation yield will show the existence of a converter lifetime that it will be measured with eBEAM too.

Chapter 5

Conclusions

This PhD thesis is focused on the AE$\bar{g}$IS antimatter experiment. The main work consisted in the design, realization and characterization of an electron beam that can deliver up to $200\mu A$ with a tunable energy from 1 to $10keV$. The system is immersed in a magnetic field and delivers a beam spot of $(2.175 \pm 0.275)\, mm$ radius. This machine, now fully operational, will be used for ageing measurements of positron to positronium converters for the AE$\bar{g}$IS experiment. It has been demonstrated that many quantities like the positronium formation yield or its outgoing velocity depend on the characteristics of the converter considered. In order to have the same conditions throughout the operating time of AE$\bar{g}$IS , it is necessary to study the effect of positron radiation dose on the converter itself. Positrons and electrons behave in the same way for what concern energy release in solids. The only difference is due to the annihilation gammas that anyway leave the AE$\bar{g}$IS converters without depositing their energy. Thus we can make ageing measurements by using electrons instead of positrons. This choice has many advantages:

- obtaining an electron beam is simpler than obtaining a positron beam;
- the current of an electron beam is much grater than that of a positron beam;
- an electron beam does not produce annihilation gamma rays.

In addition, I have been working on the design of the final AE$\bar{g}$IS positron source and participating in the studies and modelling needed for the choice of the appropriate converter for the experiment.

Finally, I made measurements of positronium formation in liquid scintillators, of interest for solar neutrino detectors. Electron antineutrinos are commonly detected in liquid scintillator experiments by inverse beta decay, looking at the coincidence between the reaction products, neutron and positron. Prior to positron annihilation, an electron-positron pair may form

orthopositronium (o-Ps) with 50% probability. Even if the o-Ps decay is speeded up by spin flip or pick up effects, its effective mean life is $\tau = 3ns$. Such a mean life may introduce distorting effects in the photoelectron time distribution, fundamental for position reconstruction and pulse shape discrimination algorithms in antineutrino experiments.

I would like to thank: Dr. M. G. Giammarchi and Prof. G. Consolati for their help during all my PhD activity; Dr. D. Franco for the PALS analysis; the AE$\bar{g}$IS collaboration and in particular the L-NESS laboratory for the possibility to collaborate with an international laboratory like CERN.

Appendix A

Thermionic emission from tungsten wire

A.1 Introduction

In order to study the electron emission from an heated Tungsten wire (thermionic effect), we consider the electrons in the metal to be in thermal equilibrium with a dilute gas of electrons moving outside it. At temperature T the electronic distribution function $N_i(E_n)$ inside the metal is:

$$N_i(E_n) = \frac{1}{e^{\frac{E_n-\mu}{k_B T}} + 1}, \tag{A.1}$$

where the total energy E_n is determined by the band structure. k_B is the Boltzmann constant and μ is the chemical potential. The electronic charge distribution in primitive Wigner-Seitz cells of the metal near the surface does not have the symmetry of the Bravais lattice so that such cells will, in general, have a non-vanishing electric dipole moment and may even yield a non-vanishing net electrical surface charge (figure A.1). The particular way in which the charge distribution in cells near the surface differs from that in the bulk depends on such details as whether the surface is plane or rough, and, if plane, on the orientation of the plane with respect to the crystallographic axis. We first consider the case in which the distortion of the surface primitive cell does not result in a net macroscopic charge per unit area of metallic surface. However, within the surface layer in which the cells are distorted, this distortion will give rise to appreciable electric fields, against which the amount of work $W_S = \int e\vec{E} \cdot \vec{dl}$ must be performed, in moving an electron through the layer. The work W_S bring about a new definition of the metal work function[1] W that, with reference to figure A.1,

[1]The metal work function is the energy that must be supplied to remove an electron from a metal.

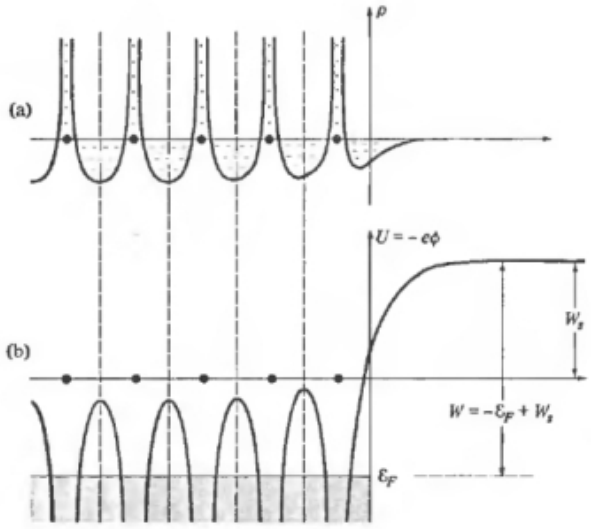

Figure A.1: Metallic solid structure.

is defined by:

$$W = -E_F + W_S = -E_F + e\phi. \tag{A.2}$$

The total energy E of an electron outside the metal should be taken to have the free particle from

$$E = K + U = K + e\phi, \tag{A.3}$$

where K is the kinetic energy, U the electrostatic potential energy and ϕ is the local value of the electrostatic potential seen before. At temperature T the electronic distribution function $N_0(E)$ outside the metal is:

$$N_0(E) = \frac{1}{e^{\frac{E-\mu'}{k_B T}} + 1} = \frac{1}{e^{\frac{K+e\phi-\mu'}{k_B T}} + 1} = N_0(K), \tag{A.4}$$

where μ' is the chemical potential of the outer electron gas. Since the electron gas inside the metal is in thermal equilibrium with electron gas outside, the chemical potential is the same, so that $\mu' = \mu$. Moreover, inside the metal, at temperature below several thousand degrees, the chemical potential differs negligibly from the Fermi energy so that $\mu \cong E_F$.

$$N_0(K) = \frac{1}{e^{\frac{K+e\phi-\mu'}{k_B T}} + 1} = \frac{1}{e^{\frac{K+e\phi-\mu}{k_B T}} + 1} = \frac{1}{e^{\frac{K-E_F+e\phi}{k_B T}} + 1} = \frac{1}{e^{\frac{K-W}{k_B T}} + 1}, \tag{A.5}$$

Since work functions W are typically a few eV in size, W/k_B is of the order $10^4 K$. Therefore in the high temperature approximation $N_0(K)$ reduces to:

$$N_0(K) = e^{-\frac{K-W}{k_B T}}. \tag{A.6}$$

From which it follows that at high temperature the electronic distribution function of the thermionic emitted electrons in vacuum (without external potentials) is given by a Maxwell - Boltzmann distribution.

A.2 The energy spectrum of the thermionically emitted electrons

The probability that a thermionic electron has a kinetic energy between $\mathcal{E}$ and $\mathcal{E} + d\mathcal{E}$ (energy spectrum) is given by:

$$P(\mathcal{E})\, d(\mathcal{E}) = \frac{N_0(\mathcal{E})}{Z} g(\mathcal{E})\, V d\mathcal{E}, \tag{A.7}$$

where $g(\mathcal{E})\, V d\mathcal{E}$ is the density of states per unit volume (DOS) in the energy range $[\mathcal{E}, \mathcal{E} + d\mathcal{E}]$ by the volume V, i.e. the number of states between $\mathcal{E}$ and $\mathcal{E} + d\mathcal{E}$ in the volume V. Moreover $N_0(\mathcal{E})$ is the electronic distribution function, i.e. the probability that one of these states is filled, and Z is the partition function. Since $\int_0^{+\infty} P(\mathcal{E}) d\mathcal{E} = 1$ the partition function is:

$$Z = V \int_0^{+\infty} g(\mathcal{E})\, N_0(\mathcal{E})\, d\mathcal{E}. \tag{A.8}$$

The DOS for electrons in three dimensions is given by[2]:

$$g(\mathcal{E}) = \frac{1}{2\pi^2} \left(\frac{2m}{\hbar}\right)^{\frac{3}{2}} \mathcal{E}^{\frac{1}{2}}, \tag{A.9}$$

where m is the electron mass and $\hbar$ the reduced Plank constant. So, the partition function, given the electronic distribution function $N_0(\mathcal{E})$, is described by:

$$\begin{aligned} Z &= V \int_0^{+\infty} g(\mathcal{E})\, N_0(\mathcal{E})\, d\mathcal{E} \\ &= V \int_0^{+\infty} \frac{1}{2\pi^2} \left(\frac{2m}{\hbar}\right)^{\frac{3}{2}} \mathcal{E}^{\frac{1}{2}} e^{-\frac{K-W}{k_B T}} d\mathcal{E} \\ &= \frac{V}{2\pi^2} \left(\frac{2m}{\hbar}\right)^{\frac{3}{2}} e^{\frac{W}{k_B T}} \int_0^{+\infty} \mathcal{E}^{\frac{1}{2}} e^{-\frac{\mathcal{E}}{k_B T}} d\mathcal{E} \\ &= \frac{V}{2\pi^2} \left(\frac{2m}{\hbar}\right)^{\frac{3}{2}} e^{\frac{W}{k_B T}} \frac{\pi^{\frac{1}{2}}}{2} (k_B T)^{\frac{3}{2}} \\ &= \frac{V \pi^{\frac{1}{2}}}{4\pi^2} \left(\frac{2mk_B T}{\hbar}\right)^{\frac{3}{2}} e^{\frac{W}{k_B T}}. \end{aligned} \tag{A.10}$$

[2]We had used a trick that is common in quantum mechanics: assume that the electron is in a large box (energy quantization) with zero potential energy (i.e. total energy is only kinetic). At the end of calculation, we will allow the size of the box to became infinite, so that the separation levels tends to zero. For any macroscopic box side L, the energy levels are very close to each other and the continuous description works well.

Finally we substitute the partition function expression in the energy spectrum formula, so that:

$$\begin{aligned} P(\mathcal{E})\, d(\mathcal{E}) &= \frac{N_0(\mathcal{E})}{Z} g(\mathcal{E})\, V d\mathcal{E} \\ &= \frac{e^{-\frac{\mathcal{E}-W}{k_B T}}}{\frac{V\pi^{\frac{1}{2}}}{4\pi^2}} \left(\frac{2mk_BT}{\hbar}\right)^{\frac{3}{2}} e^{\frac{W}{k_BT}} \frac{1}{2\pi^2} \left(\frac{2m}{\hbar}\right)^{\frac{3}{2}} \mathcal{E}^{\frac{1}{2}} V d\mathcal{E} \\ &= \frac{e^{-\frac{\mathcal{E}}{k_BT}} e^{\frac{W}{k_BT}}}{\frac{V\pi^{\frac{1}{2}}}{4\pi^2} \left(\frac{2mk_BT}{\hbar}\right)^{\frac{3}{2}} e^{\frac{W}{k_BT}}} \frac{1}{2\pi^2} \left(\frac{2m}{\hbar}\right)^{\frac{3}{2}} \mathcal{E}^{\frac{1}{2}} V d\mathcal{E} \\ &= \frac{2}{\sqrt{\pi (k_BT)^3}} \mathcal{E}^{\frac{1}{2}} e^{-\frac{\mathcal{E}}{k_BT}} \\ &= 2\sqrt{\frac{\mathcal{E}}{\pi (k_BT)^3}} e^{-\frac{\mathcal{E}}{k_BT}} d\mathcal{E}. \end{aligned} \tag{A.11}$$

This distribution represents the probability that a thermionic electron has a kinetic energy between $\mathcal{E}$ and $\mathcal{E} + d\mathcal{E}$ (i.e. the density probability function PDF). We observe that:

$$\begin{aligned} \int_0^{+\infty} P(\mathcal{E})\, d\mathcal{E} &= \int_0^{+\infty} 2\sqrt{\frac{\mathcal{E}}{\pi (k_BT)^3}} e^{-\frac{\mathcal{E}}{k_BT}} d\mathcal{E} \\ &= \sqrt{\frac{4}{\pi (k_BT)^3}} \int_0^{+\infty} \sqrt{\mathcal{E}} e^{-\frac{\mathcal{E}}{k_BT}} \\ &= \sqrt{\frac{4}{\pi (k_BT)^3}} \sqrt{\frac{\pi (k_BT)^3}{4}} = 1. \end{aligned} \tag{A.12}$$

The $P(\mathcal{E})\, d\mathcal{E}$ function for $T = 2000K$ is plotted versus the kinetic energy $\mathcal{E}$ (figure A.2)

A.3 A Monte Carlo simulation of thermionic emission from Tungsten wire

A Tungsten wire can be idealized like a straight wire with length L. In each points of this ideal wire the electron emitted by thermionic emission process have a potential energy U_w given by the difference of potential between the wire and ground. Suppose that the potential inside the wire is linear by changes from its minimum value ($0V$) to its maximum (V_{max}). Moreover suppose that the probability of having a thermionic emission at a given point of the ideal wire is uniform. The energy spectrum of the thermionic

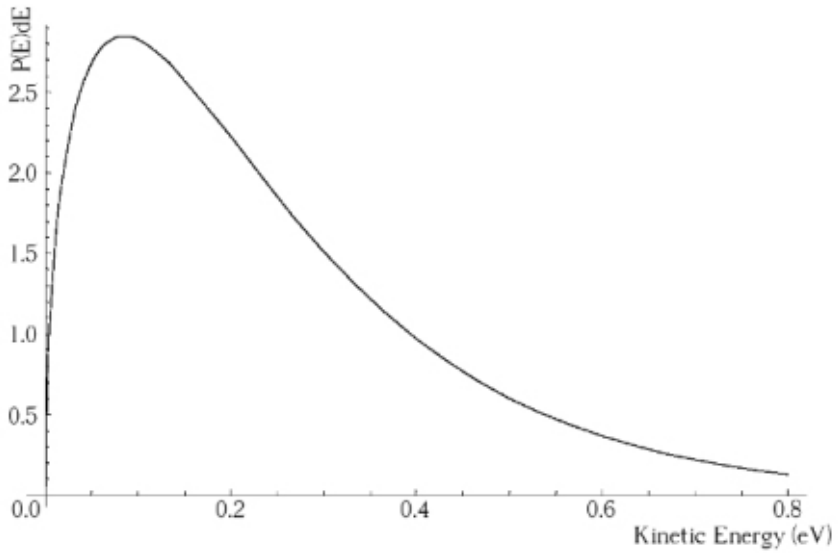

Figure A.2: The $P(\mathcal{E})\,d\mathcal{E}$ function for $T = 2000K$ is plotted versus the kinetic energy $\mathcal{E}$.

electrons does not depend on the wire size but only on the potential V_i at the emission point x_i. In order to determine the energy spectrum of the emitted electron we propose a simple Monte Carlo simulation. Its scheme is the following:

1. Extract a number V_i from a uniform distribution between zero and V_{max}. V_i represents the potential energy (in eV units) of an electron emitted at rest in a point x_i of the ideal wire of length L.

2. Extract a number $\mathcal{E}_i$ from the PDF $P(\mathcal{E})\,d\mathcal{E}$, give in equation A.11. $\mathcal{E}_i$ represent the kinetic energy (in eV units) of an electron thermionically emitted at point x_i of the ideal wire ground potential.

3. The total energy E^i_{TOT} of the i-th electron is given by $E^i_{TOT} = V_i + \mathcal{E}_i + V_e$ where V_e is the potential of extractor[3].

4. Repeat this three steps N_{events} times.

The results thus obtained can be fitted with a fit function $h(E_{TOT})$ that is the convolution of a Maxwell-Boltzmann distribution $P(\mathcal{E})\,d\mathcal{E} \equiv f(\mathcal{E})$ multiplied for the Heaviside function $\Theta(\mathcal{E})$ with the characteristic function

[3]The extractor is a diaphragm with potential V_e (positive) that extract the electrons from the wire region

$\chi_{[0,V_{max}]}$. All must be shifted by the potential energy V_e:

$$\begin{aligned} h\left(E_{TOT}\right) &= \left[f\left(\mathcal{E}\right)\Theta\left(\mathcal{E}\right)\right] * \chi_{[0,V_{max}]} \\ &= \int_{-\infty}^{+\infty} \chi_{[0,V_{max}]}\left(\tau\right) f\left(\mathcal{E}-\tau\right)\Theta\left(\mathcal{E}-\tau\right) d\tau \\ &= \int_{0}^{V_{max}} f\left(\mathcal{E}-\tau\right)\Theta\left(\mathcal{E}-\tau\right) d\tau. \end{aligned} \tag{A.13}$$

After the integration and shift $\mathcal{E} \rightarrow E_{TOT} - V_e$, $h\left(\mathcal{E}\right)$ is given by:

$$\begin{aligned} h\left(E_{TOT}\right) &= \left[\frac{2e^{-\left(E_{TOT}-U_e\right)}\sqrt{\left(E_{TOT}-U_e\right)\beta}}{2\beta^{\frac{3}{2}}}\right]\Theta\left(E_{TOT}-U_e\right) + \\ &- \left[\frac{\sqrt{\pi}Erf\left(\sqrt{\left(E_{TOT}-U_e\right)\beta}\right)}{2\beta^{\frac{3}{2}}}\right]\Theta\left(E_{TOT}-U_e\right) + \\ &- \left[\frac{e^{-E_{TOT}\beta}\sqrt{E_{TOT}}}{\beta}\right]\Theta\left(E_{TOT}\right) + \\ &+ \left[\frac{\sqrt{\pi}Erf\left(\sqrt{\beta E_{TOT}}\right)}{2\beta^{\frac{3}{2}}}\right]\Theta\left(E_{TOT}\right) \end{aligned} \tag{A.14}$$

where $\beta = \left(k_B T\right)^{-1}$. The fit function $h\left(E_{TOT}\right)$, at least, must be normalized to the number of total events N_{events}. In the final version of our Monte Carlo code we also add the energy resolution of the detector like a Gaussian broadening. From the simulations we obtain that, in principle, if we have a detector resolution of $0.1eV$ and 10^7 electrons collected, we can determine the temperature of the tungsten wire with a precision of 1.55%. The fit curve (red dashed line) and the Monte Carlo simulation (circles) with $V_e = 0V$ are shown in figure A.3.

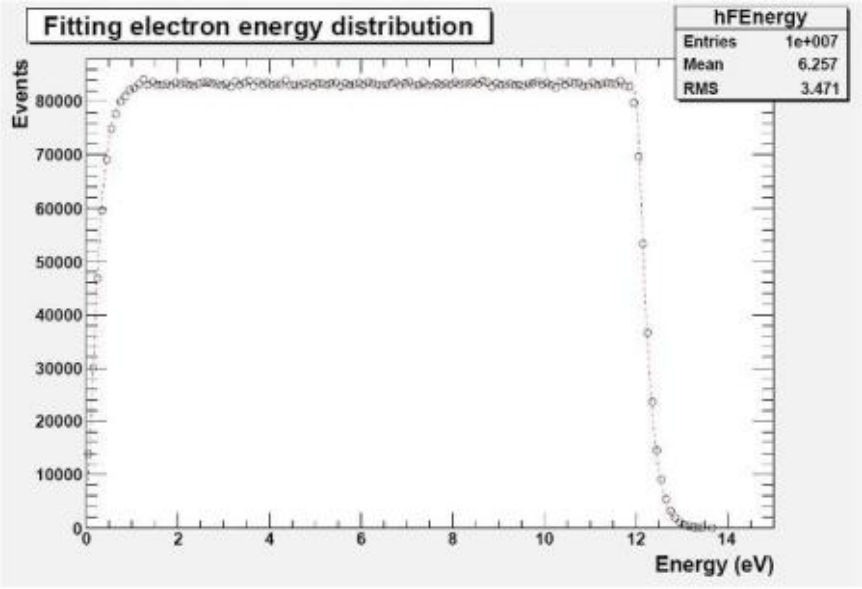

Figure A.3: The simulation results The red dashed line is the fit curve $h(\mathcal{E})$ and the black circles are the simulated electron energies detected.

Appendix B

The eBEAM magnetic field

B.1 Magnetic field calculation

B.1.1 Introduction

In this chapter we discuss the magnetic field generated by a finite solenoid (coil) [70]. In our theoretical discussion we will use cylindrical coordinates in the half-space $z \geq 0$ and model each coil by a cylindrical shell volume current. The origin of cylindrical coordinates is taken at the axis of the coil with $z = 0$ at its end. We will use Bessel functions in our calculations although other functions, such as Legendre functions and polynomials, could have been used as well. A current loop C of infinitesimal radius ρ', carrying current I, is located to the plane xy with center on the z axis (see figure B.1).

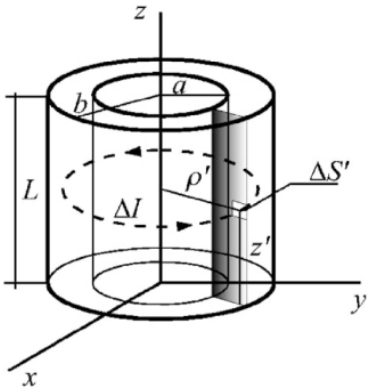

Figure B.1: The geometry of the cylindrical shell volume current used in this section. a is the inner radius b the outer and L the thickness of the cylinder.

The vector potential of the loop is

$$\vec{A}(\vec{x}) = \frac{\mu_0 I}{4\pi} \oint_C d\frac{d\vec{l'}}{|\vec{x} - \vec{x'}|}, \tag{B.1}$$

where μ_0 is the permeability of free space and $d\vec{l'} = \rho' d\phi' \hat{e}_\phi$. The unit vector $\hat{e}_\phi$ is oriented in the positive sense of the polar angle ϕ. The integral in equation B.1 can be calculated by a series expansion of $|\vec{x} - \vec{x'}|^{-1}$ in terms of the Bessel functions $J_m(\xi)$:

$$\frac{1}{|\vec{x} - \vec{x'}|} = \sum_{m=-\infty}^{+\infty} \int_0^{+\infty} dk e^{im(\phi - \phi')} J_m(k\rho) J_m\left(k\rho'\right) e^{-k|z-z'|}. \tag{B.2}$$

The magnitude of the vector potential is independent of ϕ because of the azimuthal symmetry of the currents. After integration with respect to ϕ', only terms with indices $m = -1, 1$ remain in the sum. By using the identity $J_{-1}(\xi) = -J_1(\xi)$, the x component of the potential vanishes and the vector potential becomes

$$\vec{A}(\rho, z) = \frac{\mu_0 I \rho'}{2} \hat{e}_y \int_0^{+\infty} dk J_1(k\rho) J_1\left(k\rho'\right) e^{-k|z-z'|}. \tag{B.3}$$

Equation B.3 is obtained for $\phi = 0$ with $\hat{e}_y = \hat{e}_\phi$. Another choice of ϕ would not change the potential. If we take into account that the vector potential has the same direction as the current, we can let $\vec{A} = A_\phi \hat{e}_\phi$ where

$$A_\phi(\rho, z) = \frac{\mu_0 I \rho'}{2} \int_0^{+\infty} dk J_1(k\rho) J_1\left(k\rho'\right) e^{-k|z-z'|}. \tag{B.4}$$

By use of this last equation and the superposition principle, we can derive the vector potential of an arbiter cylindrically symmetric current distribution. The finite coil can be modeled by a cylindrical shell current $\vec{K} = K\hat{e}_\phi$ with:

$$K = \frac{\Delta I}{\Delta S'} = \frac{NI}{(b-a)L} \tag{B.5}$$

where N is the number of turns of the coil and $\Delta S' = \Delta\rho' \Delta z'$ is the finite surface element. We use the equation B.4 for a narrow $\Delta z'$ and $\Delta\rho'$ strip carrying the current ΔI and obtain

$$\Delta A_\phi(\rho, z) = \frac{\mu_0 \Delta I \rho'}{2} \int_0^{+\infty} dk J_1(k\rho) J_1\left(k\rho'\right) e^{-k|z-z'|}. \tag{B.6}$$

Now, using the superposition principle we obtain the vector potential of the entire cylinder in the limit $\Delta z' \to 0$ and $\Delta\rho' \to 0$,

$$A_\phi(\rho, z) = \frac{\mu_0 NI}{2(b-a)L} \int_0^L dz' \int_a^b d\rho' \rho' \int_0^{+\infty} dk J_1(k\rho) J_1\left(k\rho'\right) e^{-k|z-z'|} \tag{B.7}$$

After integration with respect to z' and ρ' the vector potential becomes

$$A_\phi(\rho,z)=\frac{\mu_0 NIa^2\pi}{4L(b-a)}\int_0^{+\infty}dk\frac{J_1(k\rho)}{k}f(k;z)\,g(k)\,. \tag{B.8}$$

where the function $f(k;z)$ is defined by:

$$f(k;z)=\begin{cases} e^{-k(z-L)}-e^{-kz}, & z\geq L \\ 2-e^{-k(L-z)}-e^{-kz}, & 0\leq z<L \end{cases}. \tag{B.9}$$

and $g(k)$ is given by

$$\begin{aligned} g(k) &= \frac{1}{ka}\big[-J_1(ka)H_0(ka)+\frac{b}{a}J_1(kb)H_0(kb)+J_0(ka)H_1(ka)+ \\ &- \frac{b}{a}J_0(kb)H_1(kb)\big], \end{aligned} \tag{B.10}$$

where $H_0(\zeta)$ and $H_1(\zeta)$ are Struve functions [1]. The magnetic field, corresponding to the potential $\vec{A}(\rho,z)$, is calculated using $\vec{B}(\rho,z)=\vec{\nabla}\times\vec{A}(\rho,z)$ in cylindrical coordinates:

$$\vec{B}(\rho,z)=-\frac{\partial A_\phi(\rho,z)}{\partial z}\hat{e}_\rho+\frac{1}{\rho}\frac{\partial}{\partial\rho}\left[\rho A_\phi(\rho,z)\right]\hat{e}_z. \tag{B.12}$$

So, we obtain:

$$\begin{aligned} B_\rho(\rho,z) &= \frac{\mu_0 NI}{L}\frac{a^2\pi}{4(b-a)}\int_0^{+\infty}dkJ_1(k\rho)\left[e^{-k|z-L|}-e^{-kz}\right]g(k) \\ B_z(\rho,z) &= \frac{\mu_0 NI}{L}\frac{a^2\pi}{4(b-a)}\int_0^{+\infty}dkJ_0(k\rho)\,f(k;z)\,g(k)\,. \end{aligned} \tag{B.13}$$

These two integrals have to be done numerically to obtain the final values for the magnetic field.

B.1.2 MI-AEGIS.Mag

Theoretically, the magnetic field generated by a finite solenoid is given by the equations B.13. These equations do not have analytical solutions and must be solved numerically for each point of space. In order to compute

[1] The Struve function $H_n(\zeta)$ are solutions of the non-homogeneous Bessel's differential equation and are defined as:

$$H_n(\zeta)=\left(\frac{1}{2}\zeta\right)^{n+1}\sum_{k=0}^{+\infty}\frac{(-1)^k\left(\frac{1}{2}\zeta\right)^{2k}}{\Gamma\left(k+\frac{3}{2}\right)\Gamma\left(k+n+\frac{3}{2}\right)}. \tag{B.11}$$

The complex number n is the order of the Struve function, and in our studies is an integer.

the total magnetic field vector $\vec{B}(\rho, z)$ generated by a set of $\mathcal{N}$ coils, we developed a C++ program, MI-AEGIS.Mag (version 3.5). The main inputs are the simulation space in cylindrical coordinates $[\rho_{MAX}, z_{MAX}]$ and the space resolution that is the number of points in which the program compute the magnetic field vector. The maximum number of coils (like the simulation space) depends on the amount of computer memory available, in our case is 11[2]. For every coil, MI-AEGIS.Mag compute the magnetic field vector $\vec{B}_i(\rho, z)$ in each point of the simulation space. Moreover it is useful to use the symmetry of the problem respect the coil axis plane $z = 0$. In fact, the magnetic field vector $\vec{B}(\rho_0, z_0)$ at a given point (ρ_0, z_0) is related with the one in $(\rho_0, -z_0)$ by:

$$B_z(\rho_0, z_0) = B_z(\rho_0, -z_0) \tag{B.14}$$

$$B_\rho(\rho_0, z_0) = -B_\rho(\rho_0, -z_0). \tag{B.15}$$

This symmetry reduces the computational time. In order to integrate the equations B.13 we developed a set o libraries and functions. We use the Simpson's integration method that guarantees the best time to error ratio for our problem. We try also other integration methods like the gauss method, but we did not obtain better results. We find the number of Simpson's integration steps $N_{step} = 2700$ by means of the study of the time to error ratio and the integration range in k given by $[0.001, 5000]\, m^{-1}$. The algorithm is stable up to $1mm$ in space resolution (for both ρ and z). When all the $\vec{B}_i(\rho, z)$ are computed, the total magnetic field vector $\vec{B}_{TOT}(\rho, z)$ is given by:

$$\vec{B}_{TOT}(\rho, z) = \sum_{i=1}^{\mathcal{N}} \vec{B}_i(\rho, z) \tag{B.16}$$

The output of the program are three files: Mag_Rho.txt, Mag_Zeta.txt and Mag.txt. The first and the second ones represent the cylindrical components of the magnetic field vector $\vec{B}_{TOT}(\rho, z)$. The last one is the absolute value $|\vec{B}_{TOT}(\rho, z)|$ given by:

$$|\vec{B}_{TOT}(\rho, z)| = \sqrt{\left[\sum_{i=1}^{\mathcal{N}} B_{\rho,i}(\rho, z)\right]^2 + \left[\sum_{i=1}^{\mathcal{N}} B_{z,i}(\rho, z)\right]^2} \tag{B.17}$$

These files can be imported in CERN/ROOT in order to visualize the magnetic field computed. The magnetic field $\vec{B}_{TOT}(0, z)$ computed by MI-AEGIS.Mag was compared with the analytical approximation given by E. Dennison:

[2]Corresponding to a personal computer with 4Gb of memory

$$B_z(0,z) = \frac{\mu_0 IN}{2(b-a)}\left[z\ln\left(\frac{\sqrt{b^2+z^2}+b}{\sqrt{a^2+z^2}+a}\right)+ - (z-L)\ln\left(\frac{\sqrt{b^2+(z-L)^2}+b}{\sqrt{a^2+(z-L)^2}+a}\right)\right] \quad \text{(B.18)}$$

We find a good agreement between them with a maximum difference of 0.1% in $z = 0$ (figure B.2)[3].

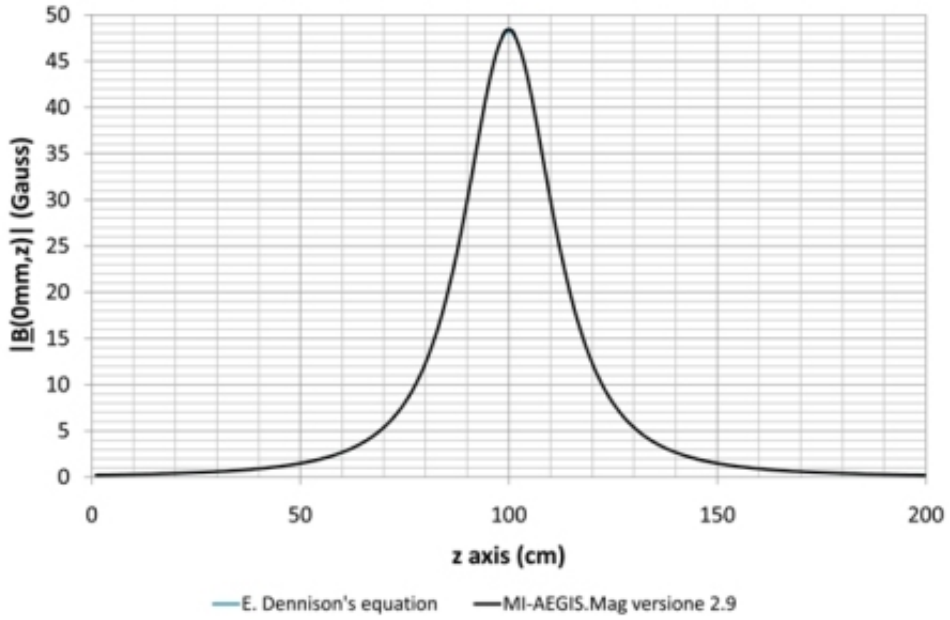

Figure B.2: Comparison between MI-AEGIS.Mag results and the E. Dennison's equation. The simulated solenoid has $a = 14cm$, $b = 19cm$, $L = 5cm$, $I = 7A$, 180 wires and centred in $(\rho = 0, z = 1m)$.

MI-AEGIS.Mag was developed for Linux and Windows XP/Vista operating OS. The program does not require a CPU performance or disk space, except that an amount of memory greater than 2Gb. The computational time for a 8 coils system, $[2m, 4m]$ simulation space with $10mm$ z resolution and $10mm$ ρ resolution is for a E6550 2.33 GHz CPU, 4Gb RAM Linux Ubuntu 8.04 OS, 10312 seconds. The three output txt files have a dimension of 4.06 MB. The MI-AEGIS.Mag is an open source software (non commercial use).

[3]Remember that the equation B.18 compute the magnetic field only on the coil axis $\rho = 0$.

B.1.3 MI-AEGIS.Mag experimental test

In order to test the MI-AEGIS.Mag software we compute the magnetic field generated by a coil (with $a = 14cm$, $b = 19cm$, $L = 5cm$, $I = 7A$, $N = 162$) and compare the theoretical results with the experimental data obtained in laboratory[69]. Particularly, we map the axial component of the magnetic field $B_z(\rho, z)$. The measurements are made with our home made gaussmeter, described in section B.2. In this section all the plots are referred to the laboratory frame showed in figure B.3.

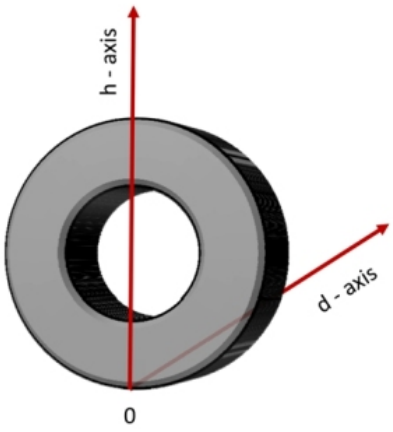

Figure B.3: The laboratory frame used for the axial magnetic field measurements.

In the MI-AEGIS.Mag computation we fix all the parameters except the wire's number N. By fitting the experimental data we obtain a value $N = 161 \pm 3$ wires (see figure B.4). This is in good agreement with the real value of 162 wires. Two examples of the experimental axial magnetic field versus h and d positions are showed in figure B.5 and B.6.

B.1.4 Magnetic field map implementation in SIMION®

In accelerator physics it is important to have a software able to simulate a given electro-magnetic system and simulate the particle tracks in the fields. For this purpose there are many commercial software, each one specialized in electrostatic, magnetostatic, electrodynamics or magnetodinamycs. It is difficult to find a software that computes the field map and simulates the relative particle tracks for both electro-magneto static systems. One of the commercial software available for electrostatic beam design is SIMION®. This software is important for our applications because it also allows to implement a magnetostatic field map and simulate the particles tracks in a electro-magneto static field. Generally SIMION® does not compute the

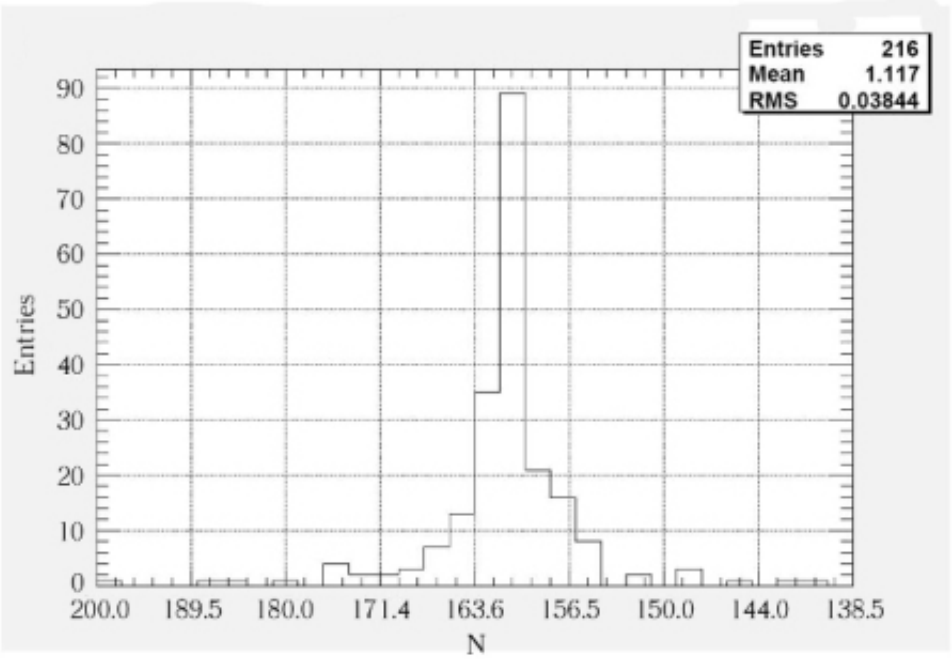

Figure B.4: The wire's number statistical distribution obtained by fitting the experimental dataset with the MI-AEGIS.Mag theoretical calculations.

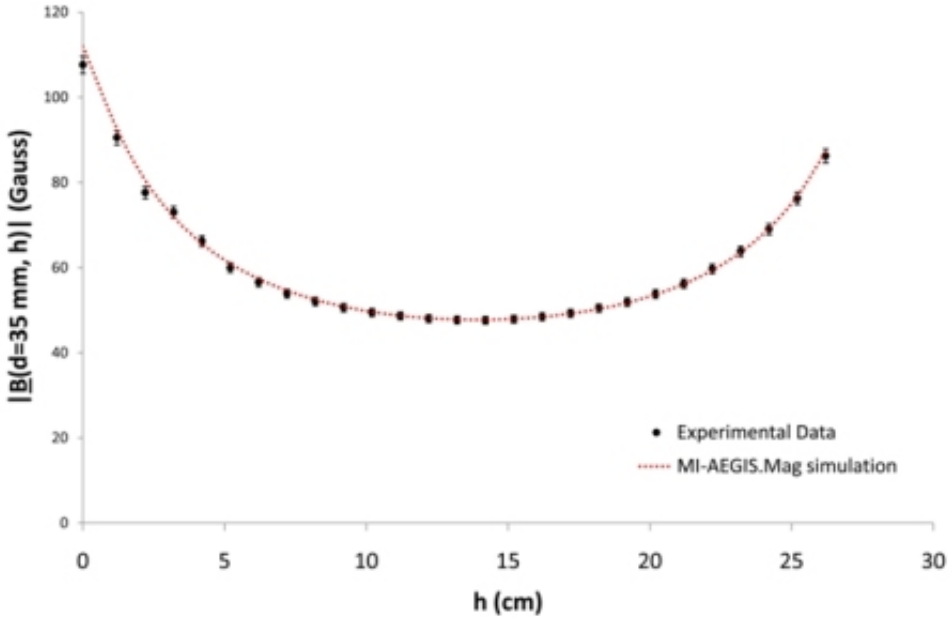

Figure B.5: The axial magnetic field $B_z(\rho, z)$ vs the hight h at depth $d = 3.5cm$. The black dots are the experimental data and the red line represents the theoretical model.

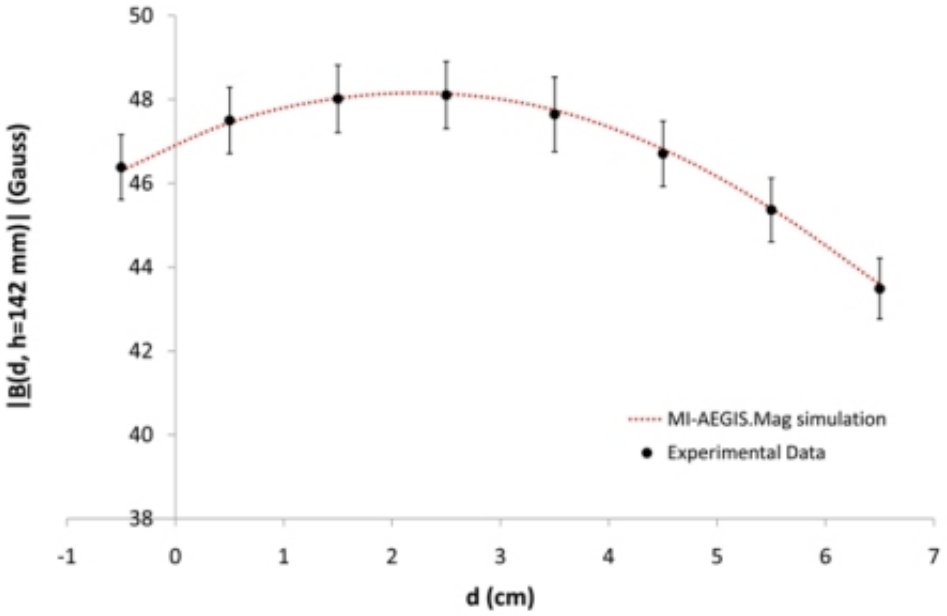

Figure B.6: The axial magnetic field $B_z(\rho, z)$ vs the depth d at hight $h = 14.2cm$. The black dots are the experimental data and the red line represents the theoretical model.

magnetic field map and so this must be computed by other external software. There are few commercial software that are able to compute the magnetic field map generated by a set of coils. MI-AEGIS.Mag is one of them with the difference that it is completely free and open source. The experimetal test described previously guarantee the accuracy of the obtained results. Another advantage of MI-AEGIS.Mag is that the three output file can be converted by a simple c-language application developed by us in a patxt file. Thanks to SL-Tools software[4], developed by the Scientific Instrument Services, Inc. it is possible to read the patxt file previously generated and convert it to a PA file. This is the file field map format accepted by SIMION®. MI-AEGIS.Mag becomes so a useful tool in order to implement the magnetic field generated by a given set of coils into an more or less complex electrostatic system. This is very important, for example, in the design of magnetically guided particle beam, particle detectors, positron source, traps and much more.

[4]Available from SIMION® version 8.0.

B.2 A gaussmeter design for the eBEAM apparatus.

We have designed, built and operated a low-cost gaussmeter for measuring magnetic fields in the range $[0, 670G]$. It is made by two parts: the first one is the Hall sensor producing a voltage proportional to the magnetic field intensity and the second one is the controller, an electronic circuit for the calibration of the scale between the output voltage of the Hall sensor and the magnetic field. In particular we set $1mV = 1G$.

Figure B.7: A picture of the low-cost homemade gaussmeter.

The Hall sensor is the SS495A1, glued on a plexiglass backing in order to measure axial fields. The electronic scheme of the controller is showed in figure B.8.

It is possible to calibrate the device through the two trimmer $(20k\Omega, 50k\Omega)$ as shown in figureB.8. The linearity of the gaussmeter was tested using the axial magnetic field generated by a coil in the $(z = 0, \rho = 0)$ point. The experimental data are reported in figure B.9.

A picture of the apparatus is showed in figure B.7.

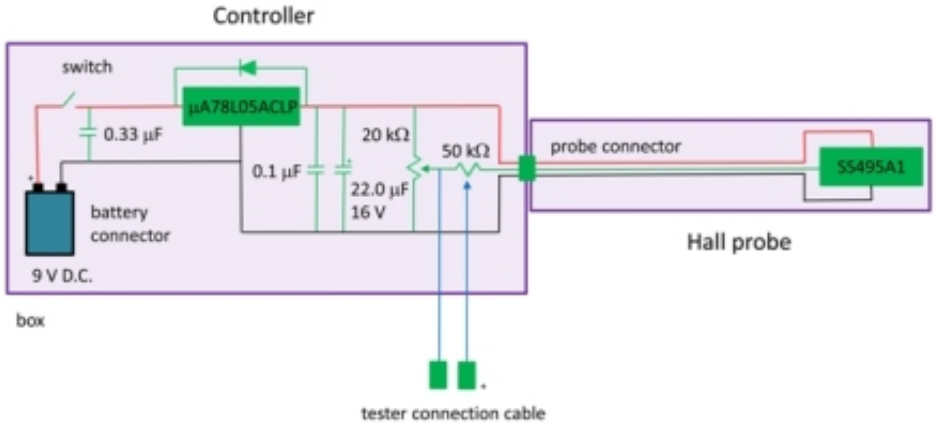

Figure B.8: The electronic sheme of the gaussmeter.

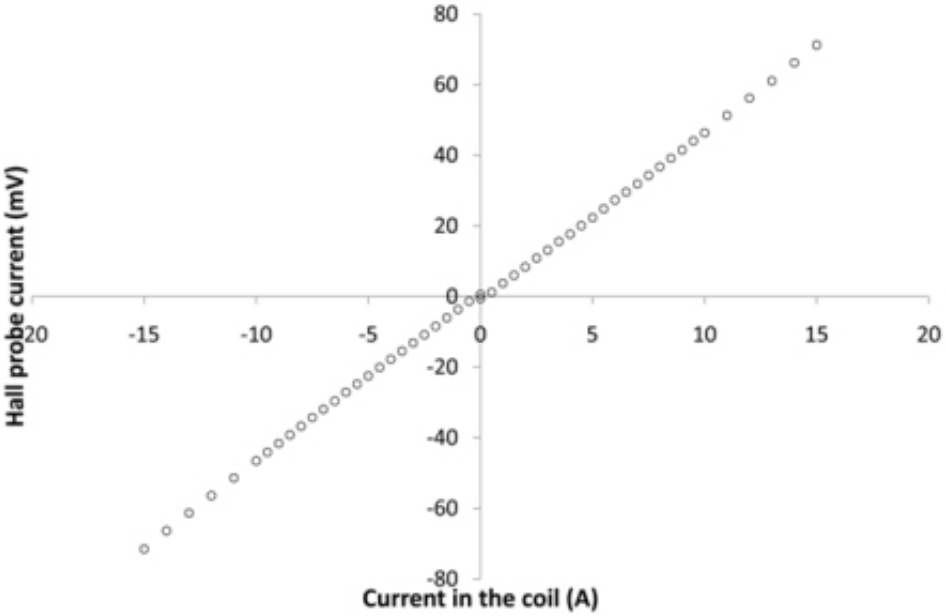

Figure B.9: The axial magnetic field intensity measured in the center of one coil (i.e. the output current generated by the Hall probe) vs its circulating current.

Bibliography

[1] J. Scherk. *Physics Letter*, 88 B:265, 1979.

[2] G. Lüders. *Annals of Physics*, 2:1, 1957.

[3] K. Nakamura et al. (Particle Data Group). *Journal of Physics G*, 37:075021, 2010.

[4] A. Kellerbauer et al. (AEGIS Proto-collaboration). *Nuclear Instruments and Measurements B*, 266:351, 2008.

[5] G. Baur et al. *Physics Letters B*, 368:251, 1996.

[6] R. Klapisch. *Physica Scripta*, T5:140, 1983.

[7] J. B. Adams. *Nature*, 185:568, 1960.

[8] G. Blanford et al. *Physical Review Letters*, 80:3037, 1998.

[9] S. Baird et al. *Nuclear Instruments and Methods in Physics Research A*, 391:210, 1997.

[10] G. Gabrielse et al. Technical Report SPSC-P-306. CERN-SPSC-97-8, 1997.

[11] M. H. Holzscheiter et al. *Hyperfine interaction*, 109:1, 1997.

[12] M. Amoretti et al. *Nature*, 419:456, 2002.

[13] G. Gabrielse et al. *Physical Review Letters*, 89:233401, 2002.

[14] W. Bertsche et al. *AIP Conference Proceedings*, 796:301, 2005.

[15] G. Drobychev et al. Technical Report SPSC-P-334. CERN-SPSC-2007-017, 2007.

[16] Yasunori Yamazaki. *Nuclear Instruments and Methods in Physics Research Section B*, 154:174, 1999.

[17] C. Maggiore et al. *Nuclear Instruments and Methods in Physics Research Section B*, 214:181, 2004.

[18] G. Testera et al. *AIP Conference Proceedings*, 1037:5, 2008.

[19] I. Boscolo et al. Technical Report SPSC-SR-055. CERN-SPSC-2010-003, 2010.

[20] I. N. Meshkov et al. *Instruments and Experimental Techniques*, 50:639, 2007.

[21] K. G. Lynn et al. *Applied Physics Letters*, 55:87, 1989.

[22] M. Kallenrode. *Space Physics: An Introduction to Plasmas and Particles in the Heliosphere and Magnetospheres.* Springer; 3rd edition, 2004.

[23] S. J. Gilbert. A New Ultra-Cold Positron Beam and Applications To Low-Energy Positron Scattering and Electron-Positron Plasmas. PhD Thesis, 2000.

[24] A. Rich. *Review of Modern Physics*, 53:127, 1981.

[25] J. A. Wheeler. *Annalen New York Accademy Science*, 48:219, 1946.

[26] A. Ore and J. L. Powell. *Physical Review*, 75:1696, 1949.

[27] R. Ley and G. With. *Positronium: Theory versus experiment in Hydrogen Atom.* Springer-Verlag, Heidelberg, 2002.

[28] P.J. Schultz and K. G. Lynn. *Review of Modern Physics*, 60:701, 1988.

[29] R. Ley et al. *Journal of Physics B: Atomic, Molecular and Optical Physics*, 23:3437, 1990.

[30] F. Castelli et al. *Physical Review A*, 78:052512, 2008.

[31] M. Charlton and J. W. Humberston. *Positron Physics.* Cambridge University Press, 2000.

[32] W. Brandt and A. Dupasquier. *Proceedinds International School of Physics "Enrico Fermi" Varenna on Lake Como, Course LXXXIII.* North-Holland, Amsterdam, 1983.

[33] A. Ore. *Årbok University of Bergen*, (9), 1949.

[34] O. E. Mogensen. *Journal of Chemistry Physics*, 60:598, 1974.

[35] D. Trezzi. Studio della produzione di Positronio nell'esperimento AEGIS. Master Thesis, 2006-2007.

[36] M. Dapor. *Electron-Beam Interactions with Solids.* Springer, 2003.

[37] J. M. Fernandez Varea et al. *Nuclear Instruments and Methods in Physics B*, 108:35, 1996.

[38] G. F. Knoll. *Radiation Detection and Measurement*. Wiley; 3rd edition, 2000.

[39] H. Gümüş et al. *Chinese Journal of Physics*, 44:290, 2006.

[40] K.A. Ritley et al. *Journal of Applied Physics*, 74:3479, 1993.

[41] S. Van Petegem et al. *Physical Review B*, 70:115410, 2004.

[42] M. Dapor. *Journal of Electron Spectroscopy and Related Phenomena*, 151:182, 2006.

[43] P. Sferlazzo et al. *Physical Review B*, 35:5315, 1987.

[44] R. S. Vallery et al. *Physical Review Letters*, 90:203402, 2003.

[45] D. W. Gidley et al. *Physical Review Letters*, 36:395, 1976.

[46] S. J. Tao. *Journal of Physics Chemistry*, 56:5499, 1972.

[47] I. K. MacKenzie. *Experimental Methods of Annihilation Time and Energy Spectrometry in Positron Solid-State Physics*. Eds, North-Holland, Amsterdam, 1983.

[48] D. M. Shrader and Y. C. Jean. *Positron and Positronium Chemistry*. Eds, Elsevier, Amsterdam, 1988.

[49] H. Saito et al. *Nuclear Instruments and Methods in Physics Research A*, 487:612, 2002.

[50] K. Rytsölä et al. *Applied Surface Science*, 194:260, 2002.

[51] F. Becvar. *Nuclear Instrument Methods Physics for Research B*, 261:871, 2007.

[52] P. Kirkegaard and M. Eldrup. *Computational Physics Communications*, 3:240, 1972.

[53] R.B. Gregory. *Nuclear Instrument Methods for Physics Research A*, 302:496, 1991.

[54] A. Shukla et al. *Nuclear Instrument Methods for Physics Research A*, 335:310, 1993.

[55] J. Kansy. *Nuclear Instrument Methods for Physics Research A*, 374:235, 1996.

[56] G. Alimonti et al. *Nuclear Instruments and Methods A*, 600:568, 2009.

[57] T. Mitsui and KamLAND collaboration. *Nuclear Physics B - Proceedings Supplements*, 117:13, 2003.

[58] I. Antcheva et al. *Computer Physics Communications*, 180:2499, 2009.

[59] H. O. Back et al. *Nuclear Instruments and Methods A*, 584:98, 2008.

[60] T. Marrodn Undagoitia et al. *Review of Scientific Instruments*, 80:043301, 2009.

[61] S. Marder et al. *Physical Review*, 103:1258, 1956.

[62] R. Ferragut et al. *Journal of Physics: Conference Series*, 225:012007, 2010.

[63] M. Baiguera. Sintesi e caratterizzazione di sospensioni di silice colloidale. Bachelor Thesis, 2007-2008.

[64] N. Djourelov et al. *Journal of Physics: Condensed Matter*, 20:095206, 2008.

[65] S. S. Kistler. *Nature*, 127 (3211):741, 1931.

[66] S. Mariazzi et al. *Physical Review B*, 81:235418, 2010.

[67] S. Mariazzi et al. *Physical Review Letters*, 104:243401, 2010.

[68] M. Eldrup et al. *Physical Review B*, 32:7048, 1985.

[69] A. Palman. Caratterizzazione di un sistema magnetico per una guida di campo magnetico di fasci elettronici. Bachelor Thesis, 2007-2008.

[70] V. Labinac et al. *American Journal of Physics*, 74:521, 2006.

List of Figures

List of Tables